

THE BALLOON-BORNE LARGE APERTURE SUBMILLIMETER TELESCOPE (BLAST) 2005: A 10 deg² SURVEY OF STAR FORMATION IN CYGNUS X

ARABINDO ROY¹, PETER A. R. ADE², JAMES J. BOCK^{3,4}, EDWARD L. CHAPIN⁵, MARK J. DEVLIN⁶, SIMON R. DICKER⁶, KEVIN FRANCE⁷, ANDREW G. GIBB⁵, MATTHEW GRIFFIN², JOSHUA O. GUNDERSEN⁸, MARK HALPERN⁵, PETER C. HARGRAVE², DAVID H. HUGHES⁹, JEFF KLEIN⁶, GAELAN MARSDEN⁵, PETER G. MARTIN¹⁰, PHILIP MAUSKOPF², JORGE L. MORALES ORTIZ¹¹, CALVIN B. NETTERFIELD^{1,12}, ALBERTO NORIEGA-CRESPO¹³, LUCA OLMI^{11,14}, GUILLAUME PATANCHON¹⁵, MARIE REX¹⁶, DOUGLAS SCOTT⁵, CHRISTOPHER SEMISCH⁶, MATTHEW D. P. TRUCH⁶, CAROLE TUCKER², GREGORY S. TUCKER¹⁷, MARCO P. VIERO^{1,4}, AND DONALD V. WIEBE⁵

¹ Department of Astronomy & Astrophysics, University of Toronto, 50 St. George Street, Toronto, ON M5S 3H4, Canada; aroy@cita.utoronto.ca

² Department of Physics & Astronomy, Cardiff University, 5 The Parade, Cardiff, CF24 3AA, UK

³ Jet Propulsion Laboratory, Pasadena, CA 91109-8099, USA

⁴ Observational Cosmology, MS 59-33, California Institute of Technology, Pasadena, CA 91125, USA

⁵ Department of Physics & Astronomy, University of British Columbia, 6224 Agricultural Road, Vancouver, BC V6T 1Z1, Canada

⁶ Department of Physics and Astronomy, University of Pennsylvania, 209 South 33rd Street, Philadelphia, PA 19104, USA

⁷ Center for Astrophysics and Space Astronomy, University of Colorado, Boulder, CO 8030, USA

⁸ Department of Physics, University of Miami, 1320 Campo Sano Drive, Carol Gables, FL 33146, USA

⁹ Instituto Nacional de Astrofísica Óptica y Electrónica (INAOE), Aptdo. Postal 51 y 72000 Puebla, Mexico

¹⁰ Canadian Institute for Theoretical Astrophysics, University of Toronto, 60 St. George Street, Toronto, ON M5S 3H8, Canada

¹¹ Physics Department, University of Puerto Rico, Rio Piedras Campus, Box 23343, UPR Station, San Juan, PR, USA

¹² Department of Physics, University of Toronto, 60 St. George Street, Toronto, ON M5S 1A7, Canada

¹³ Spitzer Science Center, California Institute of Technology, Mail Code 314-6, Pasadena, CA 91125, USA

¹⁴ Istituto di Radioastronomia, Largo E. Fermi 5, I-50125 Firenze, Italy

¹⁵ Laboratoire APC, 10 rue Alice Domon et Léonie Duquet, 75205 Paris, France

¹⁶ Steward Observatory, University of Arizona, 933 North Cherry Avenue, Tucson, AZ 85721, USA

¹⁷ Department of Physics, Brown University, 182 Hope Street, Providence, RI 02912, USA

Received 2010 September 10; accepted 2010 November 18; published 2011 January 11

ABSTRACT

We present Cygnus X in a new multi-wavelength perspective based on an unbiased BLAST survey at 250, 350, and 500 μm , combined with rich data sets for this well-studied region. Our primary goal is to investigate the early stages of high-mass star formation. We have detected 184 compact sources in various stages of evolution across all three BLAST bands. From their well-constrained spectral energy distributions, we obtain the physical properties mass, surface density, bolometric luminosity, and dust temperature. Some of the bright sources reaching 40 K contain well-known compact H II regions. We relate these to other sources at earlier stages of evolution via the energetics as deduced from their position in the luminosity–mass (L – M) diagram. The BLAST spectral coverage, near the peak of the spectral energy distribution of the dust, reveals fainter sources too cool (~ 10 K) to be seen by earlier shorter-wavelength surveys like *IRAS*. We detect thermal emission from infrared dark clouds and investigate the phenomenon of cold “starless cores” more generally. *Spitzer* images of these cold sources often show stellar nurseries, but these potential sites for massive star formation are “starless” in the sense that to date there is no massive protostar in a vigorous accretion phase. We discuss evolution in the context of the L – M diagram. Theory raises some interesting possibilities: some cold massive compact sources might never form a cluster containing massive stars, and clusters with massive stars might not have an identifiable compact cold massive precursor.

Key words: balloons – ISM: clouds – stars: formation – stars: massive – submillimeter: general

Online-only material: color figures

1. INTRODUCTION

We report on an unbiased survey of the Cygnus X (Cyg X) high-mass star formation region, conducted in 2005 by the Balloon-borne Large Aperture Submillimeter Telescope (BLAST), a 2 m stratospheric telescope that maps simultaneously at 250, 350, and 500 μm (Pascale et al. 2008). A primary ambition for BLAST was to study the earliest stages of massive protostellar evolution. Massive stars play an important role in Galactic ecology, initially through protostellar outflows and later through radiation pressure, ionization, stellar winds, and supernova explosions, and yet, in spite of their pivotal role, very little is known about their formation (Zinnecker & Yorke 2007).

Massive molecular clouds are favorable sites for massive star formation. If they are sufficiently dense to be self-gravitating,

then they also have high extinction. Even in the near- to mid-infrared they have significant optical depth, affecting observations of any embedded protostars, and leading to the “infrared dark cloud” (IRDC) phenomenon seen by the *Infrared Space Observatory* (Perault et al. 1996), *Midcourse Space Experiment* (*MSX*; Egan et al. 1998; Simon et al. 2006), and *Spitzer* IRAC and MIPS (Carey et al. 2005; Kraemer et al. 2010a). Some IRDCs are nurseries of young protostellar objects and protoclusters (Simon et al. 2006). However, IRDCs, by definition found in silhouette, require a luminous diffuse background. Massive clouds can be discovered directly, without this detection bias, by their far-infrared to millimeter wave optically thin thermal dust emission. BLAST exploits this fact.

We introduce the BLAST imaging of Cyg X in Section 2. BLAST detects thermal emission from dust in largely neutral

regions and so provides a complementary view of the interstellar medium (ISM) compared to, for example, radio emission from ionized gas (Section 2.1; though both are ultimately dependent on the local stellar radiation field and so are related spatially in some predictable ways). An important feature of BLAST imaging is its capability of observing and characterizing extended structures in the star-forming environment at different spatial scales (Sections 2.3 and 2.4). In Sections 2.5 and 2.6, we describe the identification and quantification of BLAST compact sources. The Appendix discusses measurement of their flux densities at different wavelengths for use in the multi-wavelength spectral energy distribution (SED).

Blind submillimeter surveys with BLAST (Chapin et al. 2008; Netterfield et al. 2009), precursors to those with *Herschel* (e.g., Molinari et al. 2010), are ideally suited for finding and characterizing cold sources, because of the designed coverage near the peak of the cold dust SED. This allows us to determine where the dust temperature T is low, a key requirement before determining the cold dust column densities and masses. BLAST, of course, also sees the later evolutionary stages when the dust is warmed up by the forming protostars, and again the multi-wavelength coverage tightly constrains both dust temperature and bolometric luminosity (L_{bol}).

In order to interpret the BLAST emission more fully, and place the compact sources in context, we make use of many different surveys of Cyg X in other tracers, including both continuum emission and molecular lines. These rich multi-wavelength, multi-species surveys of Cyg X are the basis of a brief overview of the physical environment in Section 3.

The SEDs and deduced properties T , L , and mass M of the compact sources are presented in Section 4. As we discuss in Section 4.6, the mass of the compact source, along with its luminosity (which maps into T), determines its position on an evolutionary track in the L - M diagram (Molinari et al. 2008). Investigating the stages of high-mass protostellar and protocluster evolution is a prime aspect of this paper.

In the earliest stages, before there is any (significant) internal source of energy from accretion or nuclear burning, the dust is heated only by the external radiation field. Because of the high extinction the dust is cold, with T typically ~ 15 K or lower, but in any case colder than the “ambient” temperature of diffuse dust in the same external radiative environment (which near these star-forming molecular clouds might be much more intense than the local interstellar radiation field). Such cold clouds, and the initial gravitationally bound condensations within them are therefore rather invisible to *IRAS*, but are in principle detectable by BLAST and ground-based surveys targeting regions of high extinction (e.g., Motte et al. 2007 using MAMBO at 1.2 mm). According to the time sequence and nomenclature used for low-mass star formation, sources detected in this earlier evolutionary stage could be called “Class -1 .” However, as a reminder of the energetics, we prefer the physically motivated shorthand “stage E” (from externally heated, but also usefully earliest—see Section 5.6). Likewise, we call sources in the subsequent evolutionary stage, when there is sufficiently vigorous accretion power internally to raise the dust to the ambient or higher temperature, “stage A” (see Section 5.5; the low-mass analog would be “Class 0”).

An illustrated view of the evolutionary stages of massive star formation, illuminated from the BLAST submillimeter perspective, is presented in Section 5.

A key factor that is important to the interpretation of our particular observations is that massive stars form in stellar groups

and star clusters (Lada & Lada 2003). The approximately $1'$ angular resolution full width at half-maximum (FWHM) of the BLAST images corresponds to 0.5 pc at 1.7 kpc. This is the size scale (sometimes called a “clump;” Bergin & Tafalla 2007) of the observed embedded and newly emerging clusters in Cyg X (Le Duigou & Knödseder 2002; Section 3.1). Thus, it is relatively straightforward to search for the precursors to these protoclusters, within which massive protostars will be the dominant source of luminosity and ionizing radiation. However, resolving protoclusters into unconfused condensations (a smaller linear scale sometimes called “cores”) that are destined to form single (proto)stars requires more angular resolution than has been available in surveys (even with the $11''$ beam of MAMBO2 which is smaller than achieved here with BLAST). Submillimeter observations with the larger telescope of *Herschel* will be better ($18''$ at $250 \mu\text{m}$ with the SPIRE camera), but not immune to these considerations.

Empirically, Bontemps et al. (2010) have made an extensive study of fragmentation and sub-fragmentation inside targeted molecular dense cores in the Cyg X region with interferometric observations at Plateau de Bure. Theoretically, it is still unclear how clusters containing massive stars form (McKee & Tan 2003; Krumholz & McKee 2008; Bonnell et al. 1997, 2001, 2007; Smith et al. 2009; Wang et al. 2010). Some insight provided by the BLAST observations and ancillary data coupled with current theory is the focus of the discussion in Section 6.

2. BLAST IMAGING OF Cyg X

Cyg X, positioned in the Galactic Plane at about $l = 80^\circ$ and about 1.7 kpc away from the Sun (Schneider et al. 2006), has long been known for its massive star formation. With BLAST (Pascale et al. 2008; Truch et al. 2008), we surveyed 10 deg^2 in Cyg X for 10.6 hr during the 2005 June flight (BLAST05), mapping the area on three visits to provide cross-linked scanning. In addition, a significant amount of calibration-related time was spent observing a circular cap of radius 1° centered on W75N, resulting in even higher signal to noise and dynamic range there.

Final maps on $15''$ pixels were produced using the map-maker SANEPIC (Patanchon et al. 2008). The combination of high scan speed and low $1/f$ knee, together with the cross-linking and common-mode removal in SANEPIC, produces a map retaining diffuse low spatial frequency emission, in contrast to current ground-based millimeter wave mapping which contends with the atmosphere and therefore is spatially filtered and emphasizes the compact structures. However, preprocessing of the time-ordered data to remove very low frequency drifts makes the SANEPIC map average near zero, the DC level having been effectively removed.

BLAST05 was designed to produce diffraction-limited beams with FWHM $30''$, $42''$, and $60''$ at 250, 350, and $500 \mu\text{m}$, respectively. However, BLAST05 suffered from an uncharacterized failure relating to the primary mirror figure and focus. Nevertheless, even with the corrupted beam the resolution is about $3'$ full width half-power (Truch et al. 2008; Roy et al. 2010), comparable to *IRAS*, though disappointing compared to the diffraction-limited images obtained in the 2006 flight (Truch et al. 2009; Netterfield et al. 2009).

The characteristic beam shape can be clearly seen at many locations throughout the field, indicating the presence of point sources with angular size comparable to the diffraction limit. Obviously, we want to work with images with as good resolution as possible. We removed the worst effects of the corrupted beam

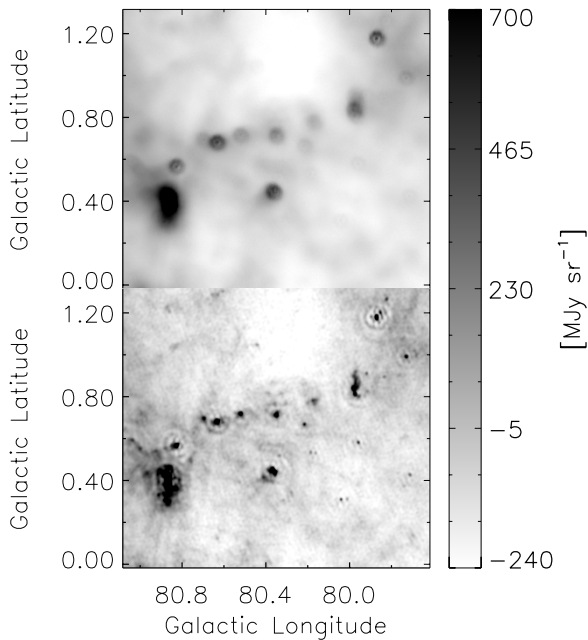


Figure 1. Upper: enlarged section of 250 μm BLAST05 image in Figure 2. Lower: deconvolved image using a Lucy–Richardson algorithm. FWHM of the deconvolved sources are about $1'$.

(see A. Roy et al. 2011, in preparation) by a Lucy–Richardson deconvolution algorithm (Richardson 1972; Lucy 1974). The significant improvement is illustrated in Figure 1.

Even so the effective resolution is about $1'$, less dependent on wavelength than for diffraction (which has the silver-lining benefit that beam matching is not an issue). Moreover, there are artifacts introduced near very strong sources. Mathematically, Lucy–Richardson deconvolution should conserve flux, and we have verified this through simulations and measurements on isolated compact sources (Section 2.6). The astrometric accuracy is good, about $5''$ when the deconvolved maps (Section 2.6) are aligned with compact sources in common with MAMBO2 (Motte et al. 2007) and/or Submillimeter Common User Bolometer (SCUBA; Di Francesco et al. 2008).

The full 250 μm map is shown in the upper panel of Figure 2.

BLAST measures the dust continuum emission along the line of sight and probes the major star-forming sites in the region by detecting reprocessed stellar or protostellar radiation. The positions of luminous stars in the Cyg OB association (Negueruela et al. 2008) and a number of stellar clusters (Section 3.1) are indicated for reference. Expanding H II regions, bubbles, and stellar outflows, and the interplay with structures in the ISM make the morphology of extended emission in the Cyg X region quite complex. A comprehensive review covering important physical aspects of Cyg X is presented by Reipurth & Schneider (2008).

2.1. A Complementary View Using Radio Continuum Emission

A complementary way to see the effects of the high-energy radiation from hot massive stars is via radio emission from the ionized gas. The lower panel of Figure 2 shows the 21 cm continuum map from the CGPS (Taylor et al. 2003), which has $1'$ resolution, about the same resolution as the BLAST maps. A number of H II regions are labeled for reference: numerals n are DR n regions from Downes & Rinehart (1966), ECX6- $*$ from Wendker et al. (1991), and otherwise G_l (accurate coordinates for these three regions being G79.957 + 0.866, G80.451 + 1.041

and G81.445 + 0.480). Note that the recombination line velocity for G79.9 is -14.8 km s^{-1} and for ECX6-27 is -64.4 km s^{-1} (Lockman 1989), putting these beyond the Cyg OB2 association.

In diffuse regions the free–free emission is optically thin, but for the most dense compact H II regions, it can be self-absorbed. There is rough correspondence with the dust emission, as might be expected given the impact of OB star radiation on both. Note, however, that unlike the dust emission, which depends on the column density, the H II emission depends on the emission measure, involving the square of the local density. Furthermore, ionizing radiation is obviously essential to produce the plasma. This radiation, the rest of the non-ionizing starlight, trapped Lyman- α , and cooling lines all heat any dust surviving in the plasma. Most of the sub-ionizing radiation escapes the plasma to heat any dust outside the H II region. In an edge-on geometry, as occurs in extended regions like DR22, the warm dust immediately outside the arc-shaped ionization front (I-front) can be seen (Figure 2 and magnified views in figures below). In a related way, in DR23, the ionization is clearly stopped on the right by a dense cloud which forms a “bay” in the radio emission, and a corresponding bright feature in the dust map.

There are also large-scale ionized structures denoted CXRn (Cyg X Ridges) by Wendker et al. (1991). Those in the BLAST region are labeled in Figure 2. These are seen dimly in the BLAST image because they have relatively low column density (they also do not show very strongly in the extinction map; Section 3.4). A much better dust emission tracer (Section 2.3) of these ionized ridges, indeed of all of the diffuse ionized gas, is the 24 μm MIPS image, from the *Spitzer* Cyg X Legacy Survey (Hora et al. 2009), which looks remarkably like the radio continuum image.

2.2. Planck Cold Core Survey

In the midst of this turmoil, we search for relatively cold structures which could be the precursors of the next generation of stars. This is also the goal of the lower-resolution Planck Cold Core survey (Juvela et al. 2010), an unbiased search using the Planck all-sky maps of submillimeter dust emission. Cold cores are characterized by a lack of corresponding *IRAS* 100 μm emission. Because the Planck high-frequency angular resolution is $4'$, clumps—even if more extended than the BLAST clumps—will appear as point sources, and smaller structures will be beam-diluted. Even for relatively nearby regions like Cyg X, the Planck beam would correspond to a spatial extent of about 2 pc.

The highest frequency Planck channels correspond approximately to 350 and 500 μm . Prior to the availability of Planck imaging data, we explored the possibilities by convolving the two longer wavelength BLAST images to the Planck resolution and combining them with *IRAS* 100 μm in a three-color image (Figure 3). At this resolution, BLAST stage E sources like C116 (Sections 4 and 5.6.1) still stand out as being cool. More extended, elongated structures such as the cool IRDC ridge near DR15 (Section 5.6.2) and the DR17 molecular pillar (Sections 3.6 and 5.1.1) are also preserved. Of course, the regions of warmer dust are highlighted in this image as well.

2.3. Diffuse Emission

BLAST maps measure surface brightness (MJy sr^{-1}), hence column density of the dust M_d :

$$I_\nu = M_d \kappa_\nu B_\nu(T) = r \mu m_{\text{H}} N_{\text{H}} \kappa_\nu B_\nu(T), \quad (1)$$

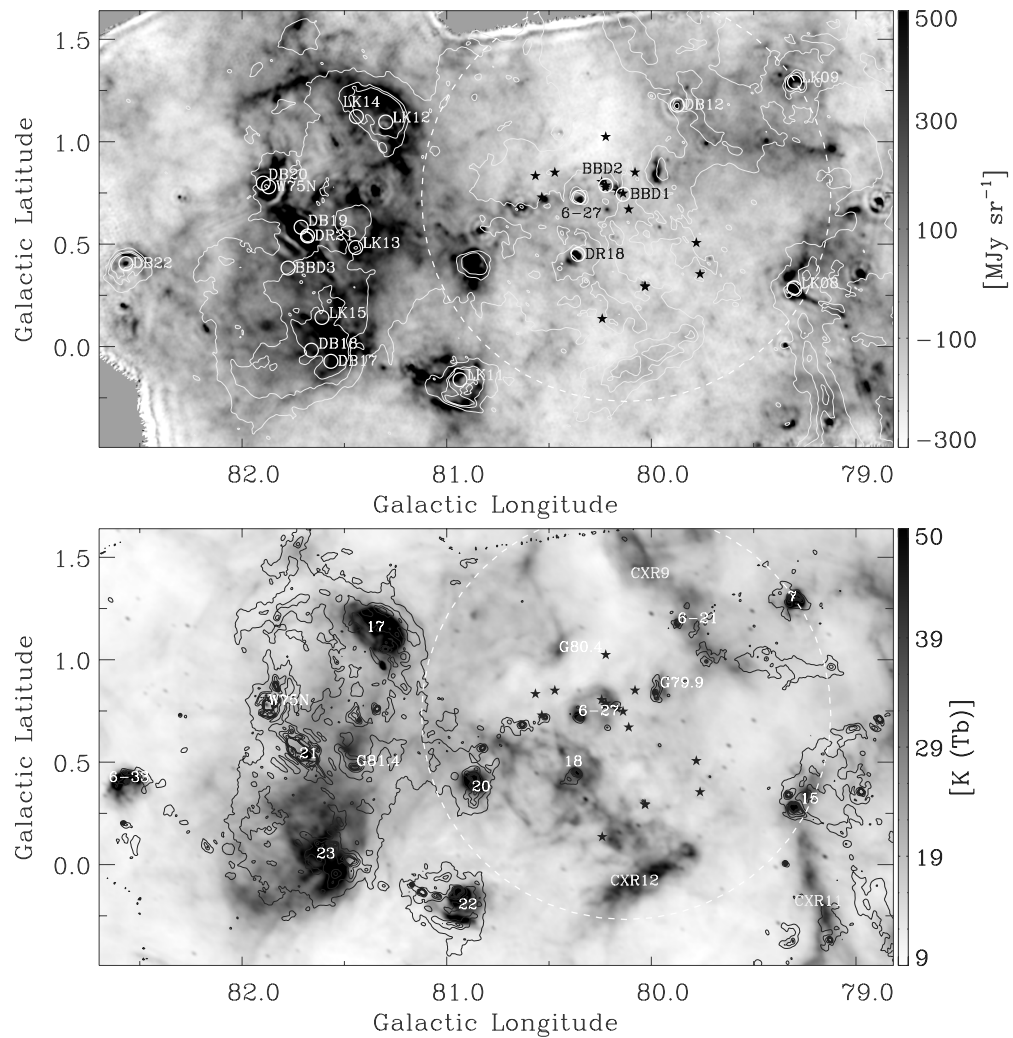


Figure 2. Upper panel: BLAST05 deconvolved $250 \mu\text{m}$ dust emission map of Cyg X. Contours are of 21 cm radio continuum emission from the CGPS in the lower panel. The large dashed circle of radius $60'$ shows the extent of the Cyg OB2 association (Knödlseder 2000) and the stars are the most luminous O stars in the list of Negueruela et al. (2008; see the text). Circles denote the positions (not extent) of star clusters (see Section 3.1 for nomenclature). Lower panel: the radio image in turn has contours from the BLAST05 image. Prominent H II regions and diffuse ridges are marked (see Section 2.1 for nomenclature).

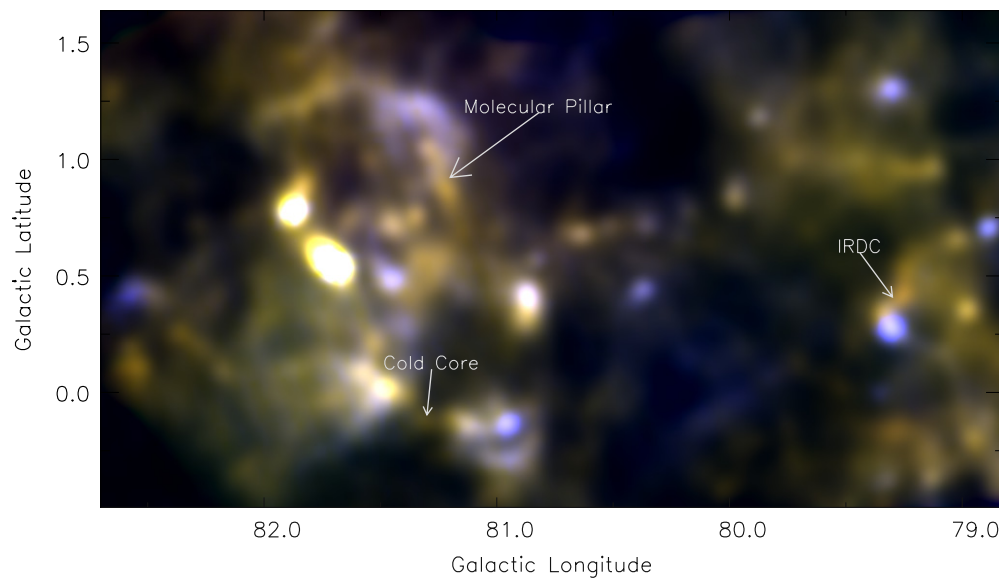


Figure 3. Three color BLAST plus IRAS image of Cyg X ($500, 350,$ and $100 \mu\text{m}$ are represented by red, green, and blue, respectively). Images are first convolved to the Planck high frequency $4'$ resolution.

where r is the dust-to-gas ratio, N_{H} is the H column density, and κ_{ν} is the mass absorption coefficient of the dust. For later characterization of the SED, we note that the spectral dependence of κ_{ν} is usually scaled with respect to a fiducial frequency as $\kappa_{\nu}/\kappa_0 = (\nu/\nu_0)^{\beta}$. Note also that for absolute measures of column density we would have to restore the zero point (DC level) of the maps, as we did for the Cas A region (Sibthorpe et al. 2010) but not here.

In the Galactic plane, cirrus-like structures in the form of bright diffuse emission, termed “interstellar froth” (Waller & Boulanger 1994), are distributed everywhere. With the compact structures removed, either explicitly or by clipping (Miville-Deschênes et al. 2007), the diffuse emission has a cirrus-like power spectrum, with lower fluctuations at high spatial frequencies. In fact, we have found that for this region the power spectrum is quite like that for *IRAS* 100 μm , with amplitude simply scaled by the SED² for the appropriate cirrus temperature (Roy et al. 2010).

Somehow, through turbulent motions, thermal instabilities, and phase transitions, massive localized regions become self-gravitating and so at high spatial frequencies they stand out from the dwindling cirrus structure as compact sources. A distribution of masses is expected, but the cirrus confusion limits our ability to distinguish lower mass sources (Section 2.5). This situation improves with angular resolution, but even for *Herschel* it is a dominant limitation (Martin et al. 2010).

Actually, the diffuse emission in the submillimeter and mid-infrared wavelengths comes from three different dust components, distinguished principally by their size distribution (Desert et al. 1990; Li & Draine 2001; Compiegne et al. 2011): big grains (BGs), very small grains (VSGs), and polycyclic aromatic hydrocarbons (PAHs). The BGs, which account for the most of the dust mass and therefore most of the longer wavelength emission, are in thermal equilibrium. The VSGs have a relatively lower share of the total dust mass, even smaller in dense regions. They are small enough to experience non-equilibrium heating and so broaden the spectrum toward shorter wavelengths, beyond the spectral peak of the BG emission. Compared to what is expected from equilibrium BGs alone, this excess non-equilibrium emission appears typically at 60 μm and shorter wavelengths. PAHs are also non-equilibrium emitters, in strong spectral bands pumped by far-ultraviolet radiation. The relative amounts of emission in these three components can vary from region to region. Schneider et al. (2006) used the *MSX* band A images (8.3 μm ; Carey et al. 2005) effectively as a tracer of PAHs and the environment. We use *Spitzer* IRAC band 4 images (8.6 μm ; Werner et al. 2004) from the Cyg X Legacy Survey (Hora et al. 2009) for the same purpose (Section 3.3), since they have better sensitivity and resolution. *Spitzer* MIPS 24 μm images trace VSG emission generally, and the hotter grains associated with ionized gas, and so, as commented above, look remarkably like the radio continuum images.

2.4. Dust Temperature from the Diffuse Emission

From the above equation it is clear that the BG emission that BLAST sees is modulated by the dust temperature T which is in equilibrium with the local radiation field, whether in the diffuse medium or within a compact source. We concentrate here on the former. For our exploratory work here on the BGs, we adopt a single-temperature SED and therefore fit only data at 100 μm and larger to avoid contamination by VSG emission.

For a sufficiently large and homogeneous region, an estimate of the characteristic temperature can be obtained by fitting an

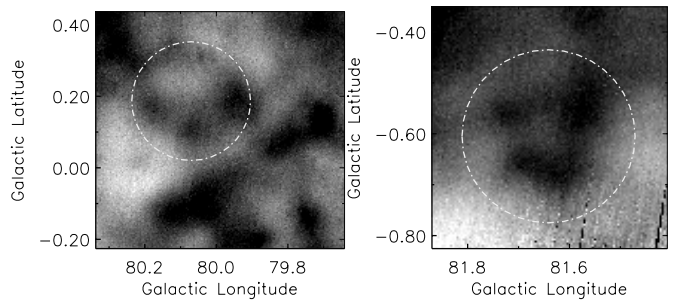


Figure 4. Two small regions in Cyg X selected on the basis of a three-color 500, 250, and 100 μm image to have warm (left) and relatively cold dust (images here at 500 μm). Note that, as in other figures, white represents lower intensity.

SED to the square root of the amplitudes of power spectra. By this method using data at 100, 250, 350, and 500 μm , Roy et al. (2010) obtained a cirrus dust temperature of 19.9 ± 1.3 K for a relatively uncrowded region (basically the right half of the BLAST map). However, this more global power spectrum method is not practical when the region considered is relatively small, inhomogeneous, and/or focusing primarily on particular sub-structures.

An alternative approach for smaller regions begins with pixel-by-pixel correlations of images with respect to some reference image (here 250 μm). Small-scale structures are remarkably well correlated across the three BLAST bands. The slopes of these correlations describe the relative SED of the spatially varying dust emission that is changing in common across these images. Note that this approach cannot give the dust temperature pixel by pixel (that would require the DC offsets too). On the other hand, the emission in each pixel is from dust of different temperatures along the line of sight, whereas our approach isolates and characterizes certain more localized spatial components.

For quantification of the size of the changes in temperature, we selected regions that appeared to have different colors in a map like Figure 3.

The first region, shown in 500 μm emission in the left panel of Figure 4, is within the relative void created by the Cyg OB2 stars, near CXR12 (Figure 2). Here there is relatively strong 100 and 60 μm emission. When the SED (left panel of Figure 5) is fit using $\beta = 1.5$, which is consistent with the value adopted for the analyses of compact sources in this paper, the derived dust equilibrium temperature $T = 29.7 \pm 2.3$ K. For $\beta = 2$, appropriate for local diffuse dust in the atomic gas at high latitudes (Boulanger et al. 1996; Li & Draine 2001), T is 25.4 ± 2.3 K. This can be compared to the local high-latitude equilibrium temperature, 17.5 K. The higher T in Cyg X results from the much higher effective interstellar radiation field from the OB association. The ridge of warm dust emission and this particular selected warm region above and to the left are also prominent in diffuse H II emission (Figure 2) and 24 μm emission, which supports the view that the local radiation field is high here. This region is particularly devoid of CO emission (Section 3.5). However, the material emitting in the submillimeter must be neutral, because the associated extinction ΔA_{ν} is up to 3 mag above the local background (and is spatially well correlated with the BLAST emission; Section 3.4). To the lower right of the CXR12 ridge, the dust is cooler, and there is some CO emission. CXR12 is oriented roughly tangentially to the direction to the center of the OB association, and might involve swept-up material. However, the geometry is unclear,

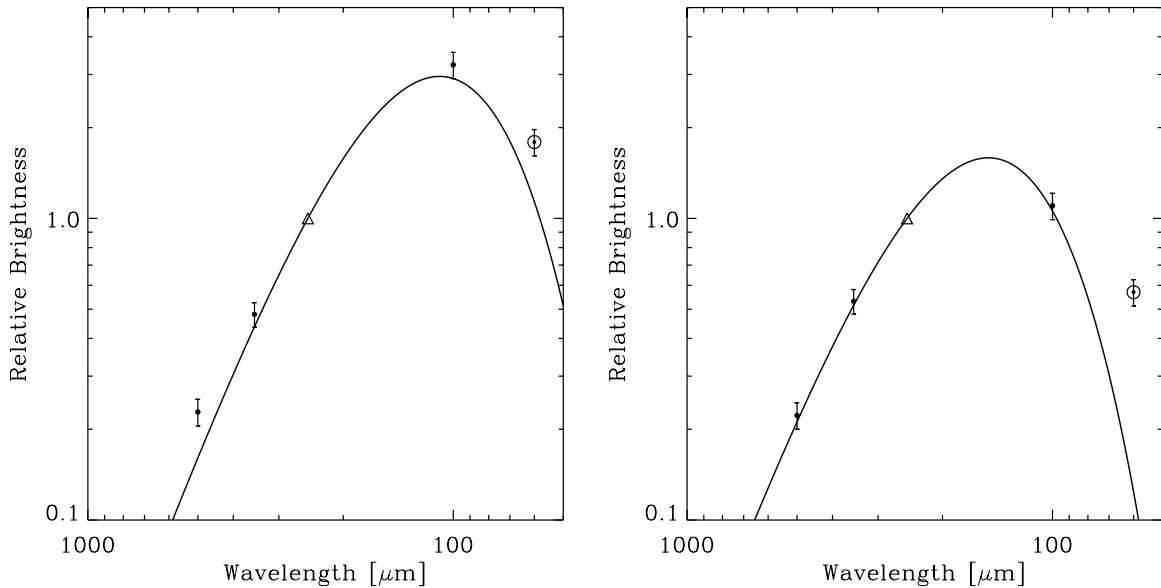


Figure 5. Left: relative SED normalized at 250 μm corresponding to the circular region shown on the left-hand image of Figure 4. The triangle shows the relative value unity at 250 μm . The SED fitted using $\beta = 1.5$ has a temperature of 29.7 ± 2.3 K. The 60 μm relative brightness (represented by a circle) is not used in the fit. Right: relative SED corresponding to the circular region shown on the right-hand image of Figure 4. The fit temperature is 21.6 ± 0.5 K.

not immediately recalling a classical edge-on photodissociation region (PDR) in a molecular cloud.

The selected cooler region, judged from relatively low 100 and 60 μm emission, is shown by a circle in the right panel of Figure 4. Its SED (right panel of Figure 5) yields an equilibrium temperature of 21.6 ± 0.5 K. The lower T would imply a lower effective interstellar radiation field, due to the high extinction, with A_V for this molecular structure (Section 3.5) up to 6 mag above the local background.

2.5. Compact Sources

When I_ν in Equation (1) is integrated over a suitable solid angle, accounting for the background, the flux density S_ν (typically in Jy) of a “source” is obtained. Likewise, the source mass M (gas plus dust) is related to the integrated column density when the distance D is known, so that

$$S_\nu = L_\nu / (4\pi D^2) = MD^{-2} r \kappa_\nu B_\nu(T). \quad (2)$$

Note that “source” refers to the dust emission that is being observed, not what heats the dust, and so in particular does not imply that there is an embedded source of energy (a star or protostar) within the volume of dust being measured.

The definition and characterization of what is a compact source is a difficult challenge, and different extraction schemes, such as Clumpfind (Williams et al. 1994), Gaussclump (Stutzki & Guesten 1990; Kramer et al. 1998), or the multi-scale method of Motte et al. (2007), can produce different catalogs and source characteristics. Operationally what is called a “compact source” is often basically a structure comparable in size to the beam. This immediately cautions that what is a compact source to one instrument could become resolved into multiple components at higher resolution, as has been illustrated by submillimeter/millimeter interferometric observations of *IRAS* protoclusters and hot cores (e.g., with the SMA and IRAM Plateau de Bure, Beuther et al. 2007a, 2007b; Bontemps et al. 2010).

As mentioned above, massive stars form in clusters. What BLAST can hope to detect in this survey at $1'$ resolution is unlikely to be a single protostar or its progenitor, but rather

a protocluster or stellar nursery possibly containing many unresolved objects. Of course, depending on the mass function, a single object among these might dominate the luminosity and ionizing flux.

We have taken a pragmatic view that since whatever underlying structure that is smeared out as a compact structure does appear quite like a Gaussian, this is an adequate model for extracting flux densities. Furthermore, the deconvolved beam for this BLAST05 survey is of similar size at all three bands, so that the same volume of dust is being examined. A corollary is that when we use other initially higher-resolution data to expand the spectral coverage of multi-wavelength photometry (the Appendix), we measured the flux density consistently by first convolving these maps to the BLAST05 resolution.

2.6. Compact Source Identification and Photometry

For compact source identification, we used the IDL-implemented DAOPHOT “FIND” routine, keeping as candidates detected peaks that were above the local background in both the 250 and 350 μm images by 3σ (empirical local rms fluctuation). Both source identification and photometry on individual sources are affected by the presence of cirrus noise; for example, at 250 μm the 1σ cirrus noise level was evaluated to be ~ 4 Jy in the fainter right portion of the map (Roy et al. 2010), although it is expected to vary over the map according to the median brightness of the region (making catalog completeness a function of position in the map). The 500 μm map was not productive for further independent identifications due to at least as great apparent relative confusion noise. In fact, for 14 faint sources among the above, it was not possible to measure a reliable 500 μm flux density. Given this noise and also the deconvolution artifacts near the brightest sources, we visually checked our candidates from the automated list. Since we were not depending on a complete survey—for example, to find a mass function or relative lifetimes of different stages—we were conservative in rejecting sources and a few were even added to the list. We were most concerned with having sources with accurately determined

SEDs, so that reliable physical parameters could be determined (Section 4).

Photometry was carried out using a Gaussian nonlinear fit, with amplitude, FWHM, position, and linear background as free parameters. Model-independent aperture photometry for isolated sources gave the same fluxes within 7%, confirming that this is an acceptable approach. Cyg X has a sufficiently flat background locally that fitting a linear background is an adequate approximation. However, in a complex crowded star-forming region like much of Cyg X, it is often not possible to extract fluxes by aperture photometry or by fitting a single Gaussian. In such cases, we adopted a multiple Gaussian technique, fitting simultaneously to all candidates within a 2.5 radius about the parent source. If a parent source in a crowded region had a low signal to noise ratio compared to its neighbors then we fixed their positions and/or FWHMs as required.

Positions and flux densities for 184 sources are given in Table 1. These Cyg X sources are referred to below as “Cn” where “n” is an up-to-three digit number, ranging from 0 to 183.

3. CONTEXT: GLOBAL ENVIRONMENT AND STRUCTURAL DETAIL

3.1. Cyg OB2 Association and Star Clusters

Cyg OB2 is among the more impressive assemblies of OB stars in the Galaxy. It is more compact than a normal association and rich enough to have been called a “young globular cluster” (Knödlseider 2000). The latest census indicates that it contains some 60–70 O-type stars (Negueruela et al. 2008). From their semi-observational HR diagram, Negueruela et al. (2008) favor a distance 1.5 kpc, with 1.8 kpc being noticeably too large. Our adopted distance of 1.7 kpc, consistent with Schneider et al. (2006) and Motte et al. (2007), is close to this and a 10% uncertainty in distance is of no consequence in the analysis that follows.

The most luminous hot stars (selected as $M_{\text{bol}} \leq -9.2$, $\log T_{\text{eff}} \geq 4.56$ and $M_{\text{bol}} \leq -9.9$, $4.46 \leq \log T_{\text{eff}} \leq 4.53$) are plotted in Figure 2 with positions from Massey & Thompson (1991) and Comerón et al. (2002). Note that star A37 (at G80.240+0.135) has what appears to be a bow-shock to its right in the *Spitzer* images and so might be a runaway star from LK8 in DR15. Kobulnicky et al. (2010) studied the bow-shock morphology of A37 (and others), placing this star slightly behind Cyg OB2 at a distance of 2.1 kpc.

According to Knödlseider (2000), Cyg OB2 extends to a radius of 1° (30 pc), with half-light radius $13'$ (6.4 pc). Examination of the sub-structure reveals two open clusters in the core (BBD1 and BBD2; Bica et al. 2003), each of radius $\sim 2'$ yet separated by only $6'$ and appearing to form a physical pair.

A number of highly reddened OB clusters and stellar groups have been found in the surrounding molecular clouds using Two Micron All Sky Survey (2MASS). Dutra & Bica (2001) performed a targeted search toward large angular-size H II regions in Cyg X; eight clusters and four stellar groups are in this BLAST survey region. Five of these have been recovered and characterized by Le Duigou & Knödlseider (2002), including the half-population radius R_{50} and central density. They also describe two new clusters. Comerón & Torra (1999) studied DR18, finding a stellar group, and Comerón et al. (2002) targeted other ECX (Wendker et al. 1991) compact H II regions finding four clusters within the BLAST area. The new one, ECX6-27, has a recombination line velocity of -62.4 km s^{-1} (Lockman

1989) and so is much more distant than Cyg OB2, more like 10 kpc. It has a “double concentration” of stars (Comerón et al. 2002) and also a complex double structure in the *Spitzer* images. The catalog of Bica et al. (2003) also includes the W75N and DR21 (W75S) infrared clusters. In total there are 13 clusters and five stellar groups (see Table 2). Their positions (not extents) are shown in Figure 2, with names in precedence LK, DB, and ECX6-* where the lists overlap. In subsequent figures, to indicate the cluster angular size we use R_{50} for the OB star population where available (Le Duigou & Knödlseider 2002), otherwise a radius of $1'$.

3.2. The Radiative Environment: Ionization

The signature of radio emission in this region of the Galactic Plane, as distinct from the radio galaxy Cygnus A, led to the name Cyg X (Piddington & Minnett 1952). A more contemporary large-scale view is given in Figure 5 of Uyaniker et al. (2001). Radio surveys conducted at different frequencies have cataloged the main H II region complexes (1390 MHz, Westerhout 1958; 5 GHz, Downes & Rinehart 1966; multi-frequency, Wendker et al. 1991). What we have observed with BLAST is only the central portion, all projected within the Cygnus superbubble. The corresponding 1420 MHz image from the CGPS, including the diffuse emission, is shown in Figure 2.

The free-free emission traces the compact sources and extended structures like I-fronts, elephant trunks and pillars, and material that is being sculpted by winds. Figure 2 shows a striking ridge of emission CXR11 extending downward from DR15. Sculpting seen in the *Spitzer* images indicates illumination from the upper left (Cyg OB2), but like CXR12, this does not appear to be a classical I-front, because the expected neutral tracers in the PDR (Section 3.3) are not present immediately to the right.

In a closed geometry, the bolometric luminosity of the dust emission is a calorimeter for radiation from any embedded (proto)stars. Likewise, the spatially integrated radio flux from the same region is a measure of the number of ionizing photons. Thus, one can check for consistency, which is particularly useful in assessing the distribution of masses within an unresolved cluster. For example, dividing the luminosity among several lower mass stars will produce a lower ionizing flux. There are complications, of course, in addition to the relative covering factors. For example, one must know the distance. If the distance is overestimated, then the luminosity will imply more massive stars and so a relatively higher ionizing flux (Comerón & Torra 2001). Furthermore, the radio emission is also affected by self-absorption. Thus, the ionized zone around young OB stars deeply embedded in dense gas (ultracompact and hypercompact H II regions) can appear to be underluminous. Multi-frequency observations (not pursued here) can of course reveal self-absorption by its spectral signature in the radio SED (see the discussion of DR21 in Wendker et al. 1991), or by the high brightness temperature if the source is resolved.

3.3. The Radiative Environment: Far-ultraviolet

The non-ionizing radiation heats dust beyond any I-front. This is the main source of the extended submillimeter emission surrounding the H II regions. As described above, in cases with “edge-on” geometries, like in DR22, there is a clear displacement of the BLAST emission to the side of the I-front away from the ionizing stars.

The non-ionizing radiation induces non-equilibrium emission when the relevant species, VSGs and PAHs, are present. Diffuse

Table 1
Measured Flux Density

BLAST ID	Source Name	l (Deg)	b (Deg)	S_{1200} (Jy)	S_{850} (Jy)	S_{500} (Jy)	S_{450} (Jy)	S_{350} (Jy)	S_{250} (Jy)	S_{100} (Jy)	S_{60} (Jy)
C0	J203057+394248	78.6760	0.1902	22.0 ± 3.9	...	85.8 ± 3.4	110.7 ± 5.6	15.6 ^a	...
C1	J202925+401118	78.8861	0.7091	8.1	28.3	151.5 ± 2.9	226.9	375.3 ± 8.0	1029.3 ± 35.2	5819.4	5699.0
C2	J202904+401506	78.8980	0.8006	90.7 ± 32.4	...	79.1 ± 17.8	59.9 ± 6.7	40.3	1.3
C3	J203329+394127	78.9454	-0.2135	23.7 ± 1.3	...	50.9 ± 2.9	85.4 ± 5.0	41.1 ^a	7.7 ^a
C4	J203323+394253	78.9546	-0.1860	33.0 ± 1.3	...	68.8 ± 2.9	130.7 ± 5.6	118.2 ^a	6.9 ^a
C5	J202653+403717	78.9566	1.3528	5.1 ± 0.4	...	7.7 ± 0.5	11.3 ± 0.9	11.2 ^a	6.1 ^a
C6	J203023+400926	78.9702	0.5401	15.2 ± 0.9	...	50.3 ± 2.4	74.4 ± 4.4	...	1.0 ^a
C7	J203112+400310	78.9778	0.3528	6.6	17.6	133.8 ± 3.0	187.6	287.8 ± 5.1	512.5 ± 10.1	935.1	688.1
C8	J202957+401533	79.0029	0.6686	4.0	...	42.0 ± 2.5	...	80.6 ± 4.8	150.8 ± 10.2	876.7 ^a	253.0 ^a
C9	J203242+395409	79.0262	0.0331	9.7 ± 1.3	...	20.9 ± 2.1	43.3 ± 4.2	40.2 ^a	39.8 ^a
C10	J203002+401637	79.0279	0.6645	4.0	...	91.3 ± 5.6	...	145.5 ± 7.5	198.4 ± 13.0	195.5 ^a	51.8 ^a
C11	J203230+395738	79.0499	0.0986	16.3 ± 1.4	...	37.0 ± 3.0	70.2 ± 5.3	89.3	52.0
C12	J203220+400021	79.0687	0.1497	11.9 ± 1.6	...	26.3 ± 4.4	71.9 ± 7.4	201.8 ^a	42.0 ^a
C13	J202903+402817	79.0746	0.9314	10.9 ± 2.3	...	28.0 ± 5.7	46.2 ± 10.1	10.8 ^a	18.8 ^a
C14	J202720+404234	79.0776	1.3350	8.9 ± 1.0	...	19.8 ± 2.6	32.8 ± 2.9	116.3	53.2
C15	J202904+403148	79.1237	0.9637	107.1 ± 6.9	...	175.6 ± 7.6	259.2 ± 9.4	292.2	122.7 ^a
C16	J203442+394448	79.1312	-0.3696	95.9 ± 5.0	...	167.0 ± 4.0	286.2 ± 6.0	540.8	85.4
C17	J203326+395612	79.1370	-0.0594	...	1.3	5.9 ± 1.1	9.4	10.6 ± 1.6	29.2 ± 3.4	112.1 ^a	20.3 ^a
C18	J203042+401921	79.1388	0.5894	11.2 ± 1.4	...	22.3 ± 3.0	32.4 ± 3.5	18.2 ^a	...
C19	J203108+401718	79.1606	0.5016	13.0 ± 1.1	...	29.7 ± 3.1	76.0 ± 4.1	452.1	178.2
C20	J203229+400848	79.1987	0.2105	19.3 ± 3.5	...	38.7 ± 6.0	91.9 ± 11.3	428.5 ^a	137.3 ^a
C21	J202655+405517	79.2044	1.5223	22.7 ± 2.5	...	53.7 ± 3.4	94.8 ± 8.5	12.6 ^a	2.3 ^a
C22	J202923+403603	79.2173	0.9549	32.7 ± 2.7	...	82.1 ± 9.5	92.9 ± 11.3	27.8 ^a	8.7 ^a
C23	J203116+402231	79.2462	0.5321	31.3 ± 3.2	...	99.8 ± 22.9	92.7 ± 12.6	...	0.1 ^a
C24	J203138+401939	79.2477	0.4492	15.5 ± 3.4	...	10.1 ± 6.4	9.0 ± 4.6	...	69.8 ^a
C25	J203146+401843	79.2499	0.4198	...	6.8	67.4 ± 2.1	...	133.5 ± 7.7	121.1 ± 7.2
C26	J203158+401833	79.2702	0.3877	3.2	10.1	44.2 ± 2.2	135.1	70.1 ± 4.1	87.3 ± 4.5	319.5 ^a	45.7 ^a
C27	J202806+405127	79.2822	1.3037	32.3 ± 1.8	...	124.4 ± 8.3	292.5 ± 18.7	1312.2	1217.3
C28	J203227+401554	79.2903	0.2855	5.4	...	44.3 ± 4.9	...	92.2 ± 8.4	307.5 ± 31.2	2885.4	2740.1
C29	J202738+405706	79.3081	1.4293	8.0 ± 1.1	...	12.8 ± 2.2	26.2 ± 2.4	129.3 ^a	21.4 ^a
C30	J202809+405301	79.3099	1.3099	91.9 ± 3.1	...	199.9 ± 7.8	453.2 ± 16.4	2654.2	2324.4
C31	J203518+395310	79.3107	-0.3767	36.9 ± 2.1	...	100.8 ± 5.2	141.7 ± 7.1	651.7 ^a	289.6 ^a
C32	J203233+401651	79.3145	0.2796	5.1	...	107.2 ± 5.5	...	275.0 ± 9.8	666.5 ± 31.4	8224.0	6221.7
C33	J202818+405309	79.3275	1.2893	21.7 ± 3.3	...	22.4 ± 4.8	84.9 ± 10.8	3271.4 ^a	1948.1 ^a
C34	J203525+395328	79.3278	-0.3913	14.1 ± 1.9	...	33.8 ± 3.2	93.7 ± 7.1	272.3 ^a	161.9 ^a
C35	J202823+405234	79.3292	1.2704	6.9 ± 11.2	...	19.2 ± 12.7	73.1 ± 34.6	2234.4 ^a	913.7 ^a
C36	J203222+401955	79.3337	0.3394	6.6	20.4	123.8 ± 3.3	172.8	238.5 ± 5.5	386.5 ± 13.3	1139.2	277.0
C37	J202802+405636	79.3459	1.3622	11.6 ± 1.1	...	19.0 ± 2.1	42.8 ± 3.7	382.5 ^a	65.3 ^a
C38	J203349+400832	79.3471	0.0025	29.8 ± 0.9	...	68.3 ± 1.9	172.1 ± 3.9	978.1	988.4
C39	J203530+395438	79.3531	-0.3928	17.6 ± 1.7	...	57.9 ± 5.0	74.2 ± 8.7	444.6 ^a	270.6 ^a
C40	J203508+395725	79.3492	-0.3102	32.0 ± 3.2	...	44.3 ± 2.6	103.2 ± 9.2	23.8 ^a	1.3 ^a
C41	J202818+405638	79.3746	1.3231	4.2 ± 0.4	...	12.4 ± 2.6	51.0 ± 5.1	479.9 ^a	121.4 ^a
C42	J203530+400053	79.4371	-0.3311	21.4 ± 3.0	...	32.8 ± 2.0	44.8 ± 3.2	101.6 ^a	11.6 ^a
C43	J202952+404842	79.4415	1.0049	21.2 ± 1.0	...	50.9 ± 1.9	81.5 ± 2.9	245.8	137.6
C44	J202754+410505	79.4460	1.4651	13.5 ± 1.1	...	39.4 ± 3.4	82.3 ± 6.7	100.4	15.7
C45	J203616+395728	79.4807	-0.4836	19.7 ± 3.3	...	63.7 ± 3.5	137.7 ± 5.7	87.1	7.1
C46	J203412+401634	79.4985	0.0231	17.7 ± 1.4	...	32.8 ± 2.0	71.3 ± 8.5	7.6 ^a	2.7 ^a
C47	J203417+401840	79.5360	0.0314	16.1 ± 0.8	...	32.0 ± 1.6	26.2 ± 2.2	19.4 ^a	12.4 ^a
C48	J203423+403039	79.7073	0.1358	28.6 ± 3.3	...	77.8 ± 10.7	55.7 ± 4.7	46.4 ^a	5.2 ^a
C49	J203311+404138	79.7185	0.4278	6.4 ± 0.4	...	11.8 ± 0.6	29.2 ± 1.1	102.4	49.2
C50	J203610+401716	79.7318	-0.2685	14.7 ± 1.1	...	36.6 ± 2.4	45.3 ± 3.4
C51	J203050+410224	79.7340	0.9909	24.3 ± 0.8	...	50.9 ± 1.7	79.5 ± 2.3	95.2	55.4 ^a
C52	J203119+410049	79.7670	0.9011	6.0 ± 0.6	...	13.4 ± 0.9	22.2 ± 1.7	33.4 ^a	19.7 ^a
C53	J202958+411639	79.8299	1.2628	10.1 ± 0.6	...	34.6 ± 1.4	53.6 ± 2.2	133.0	84.4
C54	J203134+410357	79.8364	0.8949	8.4 ± 0.8	...	16.3 ± 1.6	14.8 ± 1.5	53.6 ^a	1.6 ^a
C55	J203029+411556	79.8764	1.1790	90.0 ± 2.8	...	200.4 ± 3.5	442.4 ± 7.0	1470.4	820.4
C56	J203208+410524	79.9188	0.8234	90.0 ± 2.8	...	200.4 ± 3.5	442.4 ± 7.0
C57	J203148+410836	79.9241	0.9065	-21.5 ± 26.8	...	3.9 ± 1.4	15.6 ± 3.0	166.0 ^a	79.9 ^a
C58	J203319+405858	79.9643	0.5814	4.3 ± 0.9	...	16.5 ± 2.9	25.6 ± 4.1	112.4	51.6
C59	J203223+410748	79.9787	0.8099	7.3 ± 0.7	...	24.5 ± 0.9	40.6 ± 1.4	258.5 ^a	242.7 ^a
C60	J203201+411053	79.9789	0.8963	32.1 ± 2.1	...	72.6 ± 5.3	115.4 ± 8.3	579.5 ^a	51.7 ^a
C61	J203216+410860	79.9813	0.8397	63.5 ± 11.3	...	133.0 ± 19.8	206.6 ± 35.5	889.9	184.1
C62	J203437+405147	80.0149	0.3127	87.2 ± 4.1	...	171.6 ± 7.4	311.9 ± 13.1	63.0 ^a	70.2 ^a
C63	J203745+402529	80.0234	-0.4268	3.9 ± 0.6	...	9.4 ± 1.5	15.7 ± 1.6	41.7 ^a	...
C64	J203443+405308	80.0457	0.3090	20.9 ± 1.1	...	61.7 ± 5.0	96.7 ± 10.9	126.0	59.7

Table 1
(Continued)

BLAST ID	Source Name	l (Deg)	b (Deg)	S_{1200} (Jy)	S_{850} (Jy)	S_{500} (Jy)	S_{450} (Jy)	S_{350} (Jy)	S_{250} (Jy)	S_{100} (Jy)	S_{60} (Jy)
C65	J203309+411603	80.1752	0.7749	10.5 ± 0.7	...	17.1 ± 0.9	36.0 ± 1.5	265.8	70.0
C66	J203414+410808	80.1903	0.5331	57.6 ± 3.5	...	94.2 ± 3.4	168.6 ± 7.3	70.8	76.6
C67	J203345+411415	80.2188	0.6657	7.9 ± 1.1	...	12.7 ± 0.9	22.8 ± 1.6	208.1	73.9
C68	J203520+410551	80.2851	0.3429	16.0 ± 0.7	...	43.0 ± 1.3	79.9 ± 2.1	23.6 ^a	...
C69	J203112+414229	80.3133	1.3307	11.4 ± 0.7	...	39.2 ± 3.1	45.2 ± 3.4	31.4	4.0
C70	J203537+410615	80.3220	0.3050	5.1 ± 0.4	...	13.0 ± 1.1	18.0 ± 1.1	32.3	60.7 ^a
C71	J203358+412230	80.3536	0.7148	3.8 ± 1.1	...	9.9 ± 1.1	14.7 ± 1.6	814.3	443.2
C72	J203347+412449	80.3638	0.7658	53.3 ± 1.6	...	126.0 ± 2.1	264.7 ± 5.1	337.5 ^a	38.6 ^a
C73	J203509+411331	80.3665	0.4474	201.3 ± 102.4	...	12.1 ± 1.9	24.2 ± 3.9	2737.9	1256.9
C74	J203525+411428	80.4095	0.4162	110.5 ± 3.4	...	221.4 ± 7.0	575.7 ± 17.4	1158.3	184.8
C75	J203252+413846	80.4475	1.0436	11.8 ± 5.9	...	21.7 ± 7.8	58.1 ± 15.0	167.3	100.5
C76	J203430+413044	80.5233	0.7168	6.2 ± 0.5	...	24.5 ± 0.9	37.9 ± 1.7	549.0	255.2
C77	J203554+411919	80.5275	0.3939	41.4 ± 1.8	...	102.0 ± 3.8	212.2 ± 6.0	55.1 ^a	9.3 ^a
C78	J203215+415540	80.6069	1.3023	2.6 ± 0.8	...	157.2 ± 641.0	11.1 ± 1.7	70.2 ^a	21.6 ^a
C79	J203224+415616	80.6316	1.2855	16.9 ± 5.4	...	10.5 ± 0.9	22.8 ± 1.7	113.7 ^a	37.1 ^a
C80	J203500+413451	80.6344	0.6827	...	14.6	6.4 ± 1.3	91.9	17.4 ± 1.2	48.9 ± 3.6	1287.8	969.8
C81	J203722+411452	80.6348	0.1286	96.4 ± 2.8	...	221.8 ± 5.6	413.7 ± 7.0	5.5 ^a	...
C82	J203229+415729	80.6566	1.2855	9.7 ± 1.2	...	32.5 ± 2.2	26.8 ± 2.0	74.3 ^a	5.8 ^a
C83	J203509+413827	80.6992	0.6963	13.3 ± 3.4	...	16.4 ± 2.0	19.3 ± 1.9	370.4	157.7
C84	J203614+413412	80.7631	0.4933	55.5 ± 16.7	...	54.1 ± 4.2	141.8 ± 6.1	117.1 ^a	20.8 ^a
C85	J203608+413959	80.8287	0.5666	5.7	15.8	21.5 ± 3.7	66.5	40.6 ± 5.1	73.9 ± 5.4	1130.5	666.6
C86	J203900+411722	80.8550	-0.0910	71.6 ± 1.6	...	171.7 ± 4.1	328.5 ± 6.9	85.3 ^a	78.5 ^a
C87	J203702+413457	80.8634	0.3814	4.0	18.3	37.7 ± 2.1	135.0	74.5 ± 3.5	117.4 ± 6.4	1286.0	190.1
C88	J203652+413620	80.8634	0.4198	6.3	21.2	64.3 ± 3.2	225.5	197.9 ± 12.0	368.9 ± 18.0	3598.8	1299.8
C89	J203944+411155	80.8659	-0.2543	97.8 ± 3.3	...	259.1 ± 8.3	554.8 ± 14.5	471.9 ^a	37.1 ^a
C90	J203724+413257	80.8785	0.3064	3.7 ± 1.8	...	12.7 ± 4.0	67.2 ± 10.6	609.8 ^a	28.2 ^a
C91	J203634+414338	80.9270	0.5373	61.1 ± 15.8	...	114.8 ± 20.0	199.9 ± 46.2	58.4 ^a	10.1 ^a
C92	J203927+412023	80.9460	-0.1272	7.1	...	78.1 ± 32.1	...	53.6 ± 7.7	122.4 ± 21.5	6232.1	5024.8
C93	J204011+411432	80.9519	-0.2949	210.7 ± 10.2	...	446.2 ± 14.1	826.5 ± 25.2	1331.5 ^a	208.0 ^a
C94	J203936+411959	80.9566	-0.1519	1.8	...	54.5 ± 6.7	...	129.1 ± 19.0	262.7 ± 25.2	5171.0	2497.3
C95	J203709+414130	80.9641	0.4293	4.4 ± 2.0	...	3.3 ± 2.9	134.9 ± 15.8	395.1 ^a	98.9 ^a
C96	J203941+412111	80.9816	-0.1519	9.8 ± 0.6	...	20.6 ± 1.2	52.5 ± 3.6	3351.5 ^a	616.0 ^a
C97	J203923+412538	81.0071	-0.0632	450.6 ± 117.3	...	3592.9 ± 1145.6	286.1 ± 58.8	657.1 ^a	44.1 ^a
C98	J203646+414744	81.0046	0.5480	72.6 ± 5.2	...	156.4 ± 10.9	340.5 ± 20.2	103.3	23.6
C99	J204023+411801	81.0211	-0.2892	49.6 ± 5.4	...	118.7 ± 10.9	198.7 ± 15.9	763.4	81.4
C100	J203644+415112	81.0454	0.5895	47.5 ± 6.1	...	107.0 ± 12.2	218.7 ± 24.4	188.9 ^a	26.1 ^a
C101	J203954+412407	81.0470	-0.1563	8.1 ± 1.0	...	22.3 ± 2.0	57.3 ± 5.6	812.8	218.2
C102	J204025+412009	81.0536	-0.2733	60.5 ± 3.5	...	179.9 ± 8.0	395.2 ± 20.0	426.7 ^a	48.0 ^a
C103	J203936+412741	81.0583	-0.0735	15.9 ± 3.2	...	42.4 ± 5.8	112.0 ± 13.2	308.6 ^a	49.1 ^a
C104	J204004+412828	81.1230	-0.1364	4.5	...	70.5 ± 79.9	...	47.2 ± 17.7	62.5 ± 11.9	1790.2	611.5
C105	J203713+415407	81.1394	0.5463	85.2 ± 2.9	...	250.0 ± 6.4	502.0 ± 15.9	160.0 ^a	18.1 ^a
C106	J203636+415947	81.1457	0.6944	18.1 ± 1.3	...	36.8 ± 2.5	76.7 ± 5.1	35.6 ^a	6.2 ^a
C107	J204005+413212	81.1736	-0.1002	3.0	...	30.2 ± 1.3	...	64.7 ± 2.4	97.0 ± 4.5	526.0 ^a	65.8 ^a
C108	J203605+420851	81.2080	0.8627	41.1 ± 2.5	...	94.0 ± 5.5	169.3 ± 7.8	164.7 ^a	...
C109	J203620+420702	81.2115	0.8075	93.0 ± 7.8	...	193.0 ± 24.0	353.2 ± 46.7	51.4 ^a	7.2 ^a
C110	J203527+421435	81.2137	1.0143	12.7 ± 1.5	...	26.1 ± 3.4	87.9 ± 42.1	575.6	173.7
C111	J203506+421957	81.2465	1.1197	67.5 ± 7.9	...	74.1 ± 4.2	224.8 ± 12.4	481.4 ^a	67.2 ^a
C112	J203546+421513	81.2580	0.9729	21.3 ± 2.1	...	56.9 ± 4.7	121.8 ± 7.8	199.2 ^a	7.2 ^a
C113	J203601+421336	81.2640	0.9199	34.5 ± 4.1	...	73.7 ± 6.1	141.8 ± 11.0	247.9 ^a	19.4 ^a
C114	J203541+421649	81.2692	1.0022	20.4 ± 2.7	...	51.7 ± 5.7	126.7 ± 17.5	...	12.6 ^a
C115	J203534+422009	81.3014	1.0517	7.1	...	23.0 ± 2.0	...	54.9 ± 3.6	107.6 ± 6.5	1031.4	239.3
C116	J204034+413836	81.3126	-0.1053	2.0	...	97.0 ± 2.6	...	199.9 ± 5.8	384.0 ± 8.8
C117	J203448+422732	81.3152	1.2389	35.4 ± 1.6	...	73.7 ± 3.0	117.8 ± 4.4	1567.2	444.0
C118	J203708+420841	81.3240	0.7043	43.7 ± 3.9	...	121.0 ± 12.7	329.0 ± 32.1	...	1.8
C119	J203658+421128	81.3407	0.7592	7.8	...	5.5 ± 2.2	...	8.0 ± 3.1	25.0 ± 7.6	450.9	75.8
C120	J203740+420707	81.3616	0.6119	107.5 ± 2.7	...	247.4 ± 6.2	316.4 ± 9.7	54.2 ^a	11.5 ^a
C121	J203720+421112	81.3784	0.7021	27.4 ± 10.0	...	45.3 ± 8.5	140.3 ± 23.8	101.4 ^a	...
C122	J204029+414530	81.3955	-0.0248	15.8 ± 2.3	...	24.5 ± 4.4	37.9 ± 5.7	336.3 ^a	25.9 ^a
C123	J203505+423125	81.3984	1.2355	51.2 ± 3.1	...	98.2 ± 6.6	113.5 ± 10.9	695.4 ^a	203.3 ^a
C124	J203559+422518	81.4155	1.0428	0.6	...	37.9 ± 4.5	...	97.5 ± 13.6	207.8 ± 27.8	28.3 ^a	...
C125	J203611+422417	81.4249	1.0021	8.4 ± 0.8	...	60.2 ± 6.2	145.2 ± 17.0	148.5	64.8
C126	J203730+421353	81.4339	0.7030	4.0	...	9.7 ± 0.9	...	29.1 ± 3.4	57.0 ± 5.7	591.4	45.3
C127	J203831+420549	81.4400	0.4731	4.5	...	105.6 ± 7.5	...	225.9 ± 17.8	440.2 ± 30.1	4000.4	1385.3
C128	J203718+421630	81.4454	0.7598	1.4	...	137.3 ± 25.8	...	362.1 ± 89.3	955.5 ± 172.6	111.6 ^a	70.3
C129	J203836+420700	81.4650	0.4731	4.5	...	14.9 ± 3.5	...	34.1 ± 10.3	64.1 ± 13.1	3421.1 ^a	980.6 ^a

Table 1
(Continued)

BLAST ID	Source Name	l (Deg)	b (Deg)	S_{1200} (Jy)	S_{850} (Jy)	S_{500} (Jy)	S_{450} (Jy)	S_{350} (Jy)	S_{250} (Jy)	S_{100} (Jy)	S_{60} (Jy)
C130	J204046+414844	81.4703	-0.0331	73.4 ± 8.2	...	189.5 ± 21.6	282.2 ± 40.1	230.5 ^a	14.6 ^a
C131	J204052+414756	81.4707	-0.0555	15.4 ± 4.7	...	33.5 ± 9.8	111.5 ± 16.3	785.9 ^a	133.2 ^a
C132	J204035+415057	81.4779	0.0172	5.0	...	8.1 ± 2.5	...	7.6 ± 4.7	28.8 ± 12.7	1449.3 ^a	...
C133	J203831+420938	81.4919	0.5099	268.0 ± 12.9	...	596.3 ± 29.0	1082.0 ± 51.9	1723.5 ^a	159.4 ^a
C134	J203822+421144	81.5024	0.5537	1.6	...	19.9 ± 5.3	...	45.6 ± 13.2	171.1 ± 39.3	1036.8 ^a	107.5 ^a
C135	J203957+415918	81.5163	0.1952	1.6	4.8	41.3 ± 5.6	...	115.0 ± 11.6	240.6 ± 27.4	122.4	75.5
C136	J203954+420055	81.5319	0.2191	18.8 ± 1.1	...	34.2 ± 2.2	73.9 ± 3.7	263.4 ^a	19.0 ^a
C137	J203514+423936	81.5230	1.2966	64.8 ± 2.8	...	165.6 ± 9.1	190.5 ± 10.3	413.8	54.8
C138	J203725+422217	81.5360	0.8000	54.9 ± 22.5	...	44.4 ± 3.9	575.7 ± 203.2	157.0	16.2
C139	J203638+422921	81.5424	0.9868	0.5	...	9.4 ± 3.2	...	9.4 ± 3.3	23.9 ± 6.6	34.1 ^a	12.3 ^a
C140	J204104+415147	81.5438	-0.0453	34.4 ± 1.2	...	53.6 ± 2.8	88.2 ± 3.6	973.0 ^a	168.0 ^a
C141	J204029+415717	81.5502	0.0965	3.3	9.8	50.9 ± 2.5	65.4	150.7 ± 6.6	396.5 ± 22.9	230.3	36.9
C142	J203944+420413	81.5566	0.2772	66.1 ± 1.6	...	143.3 ± 5.3	234.9 ± 9.4	254.6 ^a	14.6 ^a
C143	J203635+423047	81.5552	1.0095	13.1 ± 1.5	...	33.1 ± 3.9	67.3 ± 5.8	14.9 ^a	...
C144	J203931+420634	81.5630	0.3331	22.7 ± 1.6	...	35.8 ± 2.8	61.3 ± 4.3
C145	J204033+415857	81.5804	0.1026	1.8	6.2	11.6 ± 1.5	38.9	36.4 ± 3.1	68.4 ± 6.2	733.3 ^a	81.7 ^a
C146	J203430+424933	81.5759	1.5032	56.4 ± 1.6	...	109.0 ± 4.7	188.7 ± 8.7	186.8 ^a	16.8 ^a
C147	J203931+420821	81.5869	0.3510	66.6 ± 13.2	...	125.5 ± 23.7	166.0 ± 20.3
C148	J203520+424413	81.5967	1.3267	24.2 ± 6.9	...	27.0 ± 5.8	44.3 ± 9.1	257.7 ^a	25.7 ^a
C149	J204048+415757	81.5948	0.0568	2.2	...	10.3 ± 1.2	...	27.5 ± 2.6	72.7 ± 4.5	128.0 ^a	2.2 ^a
C150	J203449+424829	81.5973	1.4446	21.2 ± 4.4	...	63.1 ± 9.3	132.5 ± 19.7	109.1	10.0
C151	J203914+421221	81.6081	0.4326	26.2 ± 21.9	...	14.4 ± 3.0	34.4 ± 4.6	162.3	4.8
C152	J203620+423723	81.6164	1.1110	21.4 ± 4.7	...	38.5 ± 8.7	114.2 ± 16.6	59.0 ^a	10.8 ^a
C153	J204044+420129	81.6349	0.1012	14.4 ± 1.1	...	34.0 ± 2.6	74.0 ± 5.3	93.9 ^a	101.8 ^a
C154	J203807+422443	81.6468	0.7213	16.0 ± 4.5	...	95.7 ± 24.7	80.1 ± 16.2	184.7 ^a	10.8 ^a
C155	J203902+421939	81.6811	0.5372	48.7	127.1	33.2 ± 3.9	738.0	78.9 ± 8.2	164.6 ± 23.2	19911.5	13058.7
C156	J204046+420536	81.6920	0.1397	578.6 ± 27.7	...	1391.9 ± 68.2	3391.8 ± 113.3	207.3	55.2
C157	J203901+422249	81.7217	0.5713	46.8	146.7	15.8 ± 1.1	1160.0	56.0 ± 3.6	135.9 ± 10.1	16765.7	2429.5
C158	J204103+420547	81.7269	0.0994	838.8 ± 22.4	...	1917.1 ± 61.7	4111.7 ± 98.7	312.1 ^a	26.3 ^a
C159	J203444+425911	81.7312	1.5634	4.0 ± 0.9	...	18.2 ± 1.4	42.7 ± 2.8	848.0	257.5
C160	J203901+422506	81.7524	0.5938	27.1	91.6	35.4 ± 3.3	621.3	91.5 ± 6.9	195.7 ± 13.2	7777.6	1145.1
C161	J204236+415454	81.7603	-0.2385	597.2 ± 75.6	...	1501.2 ± 272.6	1700.2 ± 301.4	297.3	24.4
C162	J203548+425243	81.7607	1.3445	9.9 ± 1.8	...	24.8 ± 3.6	46.5 ± 4.7
C163	J203749+423846	81.7992	0.9075	0.6	...	22.6 ± 2.3	...	31.1 ± 3.7	47.3 ± 7.4	283.9 ^a	56.6 ^a
C164	J203755+423840	81.8093	0.8919	0.6	...	31.1 ± 1.6	...	46.8 ± 8.0	98.2 ± 8.6	451.8 ^a	87.6 ^a
C165	J203810+423817	81.8316	0.8521	1.6	...	29.7 ± 3.6	...	67.2 ± 8.7	73.2 ± 11.7	432.5	142.7
C166	J203639+425112	81.8337	1.2052	2.4	...	62.1 ± 5.6	...	96.3 ± 16.5	233.3 ± 16.0	307.5	82.3
C167	J203804+423945	81.8399	0.8813	5.4	...	45.7 ± 2.7	...	139.2 ± 6.5	215.2 ± 11.3	812.8 ^a	99.0 ^a
C168	J203757+424050	81.8410	0.9098	88.1 ± 3.3	...	204.0 ± 10.2	347.9 ± 14.1	404.6	26.5
C169	J203837+423738	81.8733	0.7795	36.5	87.3	22.5 ± 3.0	1008.0	33.6 ± 6.3	49.5 ± 12.1	15488.2	11970.0
C170	J203644+425507	81.8961	1.2309	515.9 ± 9.8	...	1140.6 ± 28.2	3202.4 ± 46.1	125.5 ^a	13.6 ^a
C171	J204237+422613	82.1734	0.0809	10.6 ± 1.5	...	38.8 ± 3.7	80.4 ± 3.9	219.5	154.5
C172	J204234+422726	82.1836	0.1005	24.8 ± 1.6	...	55.7 ± 3.3	107.7 ± 4.4	98.9 ^a	37.1 ^a
C173	J204013+425459	82.2814	0.7228	23.0 ± 1.4	...	40.4 ± 2.8	55.0 ± 3.4	81.9 ^a	4.7 ^a
C174	J204017+425624	82.3073	0.7280	17.5 ± 0.7	...	25.5 ± 1.5	21.8 ± 5.2	126.1 ^a	40.6 ^a
C175	J204227+424151	82.3591	0.2663	14.8 ± 0.7	...	31.7 ± 1.6	56.6 ± 2.1	22.3 ^a	3.7 ^a
C176	J204159+424812	82.3909	0.3972	65.6 ± 5.6	...	91.2 ± 5.3	147.6 ± 8.1	185.1 ^a	41.4 ^a
C177	J204211+425258	82.4752	0.4182	13.9 ± 1.1	...	31.4 ± 2.3	80.8 ± 6.1	526.3	80.5
C178	J204209+425519	82.5020	0.4479	68.2 ± 4.7	...	97.4 ± 6.6	222.5 ± 12.8	618.1 ^a	77.6 ^a
C179	J204341+424355	82.5271	0.1077	17.3 ± 1.7	...	10.0 ± 5.3	78.2 ± 9.9	54.9 ^a	4.1 ^a
C180	J204234+425649	82.5689	0.4029	80.7 ± 15.1	...	88.9 ± 5.6	141.9 ± 10.1	573.4	769.8
C181	J204346+424707	82.5787	0.1285	14.3 ± 1.4	...	53.0 ± 4.1	125.3 ± 6.6	9.4 ^a	...
C182	J204222+425831	82.5695	0.4482	31.4 ± 3.3	...	27.3 ± 2.2	32.1 ± 3.9	500.2	179.1
C183	J204329+424954	82.5826	0.1985	20.5 ± 4.7	...	103.8 ± 6.3	222.2 ± 14.0	168.4	95.5

Note. ^a Upper limit.

PAH emission is well traced by *MSX* band A; the *MSX* map of Cyg X is discussed by Schneider et al. (2006). PAH emission can now be seen in more exquisite detail in the IRAC band 4 images. Where the geometry is favorable, this reveals impressive PAH-fronts (defined by where the exciting radiation is attenuated) outside the I-fronts. There is also a sweeping arc to the lower right of DR15. This is not immediately adjacent to the ionized

ridge CXR11 mentioned above (thus not the standard I-front-PDR geometry). The arc (and ridge) can be seen as well in MIPS 24 μ m emission (Hora et al. 2009), which we interpret there as VSG emission.

MIPS 24 μ m dust emission also turns out to be a good tracer of the plasma, although because of the different physics there is not a complete morphological or brightness correspondence.

Table 2
Clusters and Stellar Groups

Cluster ^a ID	<i>l</i> (Deg)	<i>b</i> (Deg)	Other Names
LK08	79.302	0.286	DB10, ECX6-25
LK09	79.301	1.291	DB11, ECX6-18
DB12 ^b	79.879	1.178	ECX6-21
ECX6-27	80.354	0.728	...
DR18 ^b	80.357	0.450	...
LK11	80.935	-0.167	DB13, DB14 ^b
LK12	81.298	1.096	DB15
LK13	81.445	0.483	DB16
LK14	81.441	1.122	...
DB17	81.566	-0.719	...
LK15	81.610	0.142	...
DB18 ^b	81.661	-0.017	...
DR21	81.680	0.540	...
DB19 ^b	81.711	0.582	...
W75N	81.870	0.779	...
DB20	81.896	0.797	...
DB22	82.567	0.404	...

Notes.

^a LK, DB, and ECX6 are the cluster IDs by Le Duigou & Knödsleder (2002), Dutra & Bica (2001), and Comerón et al. (2002), respectively.

^b Stellar group.

In the figures for the selected regions below (Section 3.6), we show the 24 μm emission overplotted with 21 cm radio emission contours to illustrate their correlation, and also the relationship to clusters and the BLAST compact sources.

3.4. Extinction

Another tracer of column density is near-infrared extinction (often expressed as its equivalent in A_V), which can be estimated from the colors of 2MASS sources. Such a map by S. Bontemps (2007, private communication) is presented in Figure 1 in Motte et al. (2007). A_V and BLAST emission are well correlated. This correlation can be used to calibrate the dust opacity (P. G. Martin et al. 2011, in preparation). In their Figure 1, Schneider et al. (2006) show an $H\alpha$ image which strikingly shows the foreground optical extinction called the Great Cygnus Rift.

3.5. The Molecular Reservoir

Numerous surveys of the Cyg X giant molecular cloud (GMC) have been carried out in the molecular line transition $^{12}\text{CO } J = 1 \rightarrow 0$ (Cong 1977; Dame et al. 1987; Leung & Thaddeus 1992). Schneider et al. (2006) report on an extensive multi-transition survey with KOSMA ($^{13}\text{CO } J = 2 \rightarrow 1$, $3 \rightarrow 2$, and $^{12}\text{CO } J = 3 \rightarrow 2$) to study in detail the spatial structural variations and physical conditions. The relative intensity of $^{13}\text{CO } J = 3 \rightarrow 2$ to $^{13}\text{CO } J = 2 \rightarrow 1$ depends on the local density and kinetic temperature. Their $^{13}\text{CO } J = 2 \rightarrow 1$ channel maps show elongated filamentary structure at scales of $10'$ to $20'$, and smaller sub-structures (CO clumps) embedded in the larger cloud fragments. The peaks of the CO emission profiles occur over a wide range of radial velocities surveyed from $+20$ to -20 km s^{-1} (there is not much gas beyond -10 km s^{-1} and gas at more negative “Perseus arm velocities” is not included).

Schneider et al. (2006) provide a comprehensive treatment of the region from this molecular line perspective. They estimate $4 \times 10^6 M_\odot$ of molecular gas, at the large end of GMC masses in the Milky Way. Thus, despite the prior star formation, there remains a tremendous reservoir of gas pregnant with

Table 3
Structures Observed at 1.2 mm Associated with BLAST Clumps

BLAST ID	Core ^a ID	Clump ^a ID	$\Sigma_{\text{core}}^{\text{a}}$ (g cm^{-2})	$\Sigma_{\text{clump}}^{\text{a}}$ (g cm^{-2})
C1	S26	CI-S5	0.58	0.33
C7	S30, S31	CI-S7	0.21	0.18
C8	S29	CI-S6	0.08	0.08
C26	S34	CI-S9	0.08	0.08
C28	S39	...	0.12	...
C32	S40, S41	CI-S11	0.13	0.11
C36	S36, S37, S38	CI-S10	0.16	0.12
C85	N5, N6	CI-N3	0.15	0.15
C87	N14	CI-N6	0.48	0.14
C88	N10	CI-N4	0.43	0.18
C90	N17	...	0.15	...
C92	N58, N59	CI-N17	0.22	0.18
C104	N62	CI-N20	0.08	0.09
C107	N63	CI-N21	0.96	0.28
C115	N1, N2	CI-N1	0.56	0.29
C116	N70	...	0.07	...
C119	N12, N13	CI-N5	0.58	0.21
C126	N18	CI-N9	0.07	0.07
C127	N29	CI-N11	0.06	0.08
C128	N16	...	0.13	...
C132	N67, N69	CI-N23	0.05	0.09
C134	N26	...	0.06	...
C135	N61	...	0.07	...
C139	N8	...	0.12	...
C141	N65, N64	CI-N22	0.14	0.10
C145	N68	...	0.29	...
C149	N72	...	0.05	...
C155	N42, N46, N47	CI-15	2.30	1.67
C157	N36, N38, N41, N44, N48	CI-N14	1.92	1.24
C160	N37, N43, N51, N53, N54	CI-N16	0.45	0.45
C163	N20	...	0.18	...
C166	N9	...	0.05	...
C167	N21, N22, N24	CI-N10	0.08	0.10
C169	N30, N31, N32	CI-N13	2.49	1.27

Note. ^a Core, clump ID, and surface density are from Motte et al. (2007).

star formation, offering the opportunity of studying many evolutionary stages. To this end, Motte et al. (2007) have carried out a continuum survey at 1.2 mm with MAMBO further revealing through dust emission the complex and hierarchical morphology in the region. They find that Cyg X hosts about 40 massive protostars destined to be OB stars. As discussed in Section 5.4, the more massive protostars are already forming (ultra)compact H II regions, famous examples being DR21 (Downes & Rinehart 1966), W75N (Westerhout 1958), and AFGL2591, the strongest submillimeter compact sources within the BLAST coverage. Table 3 lists the correspondences between the cores and clumps of Motte et al. (2007) and our BLAST sources.

CO emission integrated over the line profile (W) is often taken as a surrogate of the column density of molecular hydrogen and so should be correlated with BLAST emission. We note the good correspondence and explore this in the examples below. Radiation from massive stars can of course in time destroy CO and the detailed correspondence with dust emission.

Neither dust continuum emission nor W is sufficient for describing the complete physical environment and geometry of the star formation region. Additional insight can be gained by the examination of the CO velocity cubes (Schneider et al. 2006). Where there is CO coverage in our BLAST map, most of

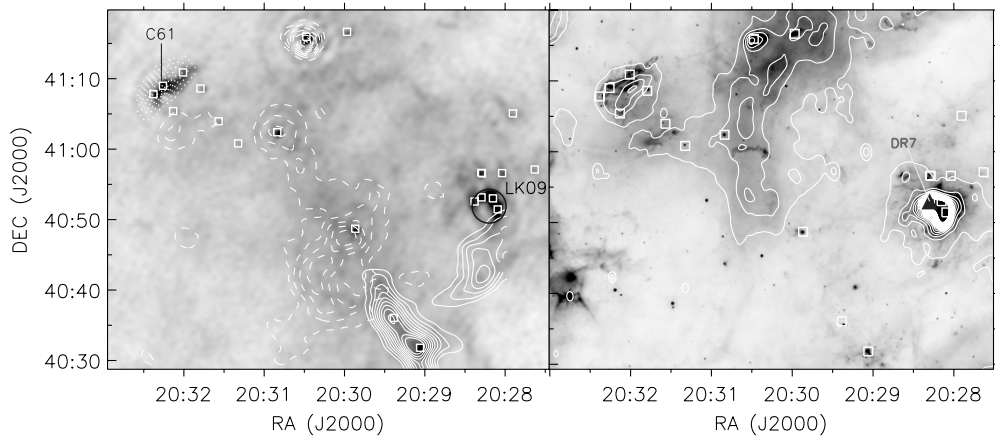


Figure 6. Left: BLAST 250 μm image including DR7 overlaid with contours of $^{13}\text{CO } J = 2 \rightarrow 1$ emission integrated over velocity ranges chosen to highlight the clumps discussed by Schneider et al. (2006), Figure B.4. Solid, dash, and dot contour lines correspond to the ranges 3 to 9, -7 to -1 , and -13.5 to -8 km s^{-1} , respectively. The circle represents the position and extent R_{50} of a star cluster (Le Duigou & Knödlseder 2002). Right: 24 μm MIPS map of the same region, with contours of the 21 cm radio continuum emission from the CGPS (see Figure 2). BLAST compact sources are marked in each image by square boxes of $1/3$ width. Note the MIPS counterparts to many BLAST sources.

the identified BLAST compact sources are correlated with CO emission features (within the CO clumps mentioned above), thus associating the dust emission with gas at a certain velocity. In Section 3.6, we provide a few examples using their $^{13}\text{CO } J = 2 \rightarrow 1$ cube to emphasize that objects seen closely together in projection in a dust emission image can have quite different velocities. In principle, the velocity associations could be used to sort the sources with respect to distance. In Cyg X, Schneider et al. (2006) have argued that the main velocity systems are all at roughly the same distance, 1.7 kpc. Nevertheless, the association with different CO clumps having differing velocities does indicate that the BLAST compact sources are in distinguishable environments, and there certainly are some sources behind the main Cyg OB2 complex (Section 4.2).

3.6. Selected Regions

In this section, we show the BLAST compact sources in the context of the diffuse submillimeter emission and other tracers discussed above. They are marked in the figures with a $1/3$ square, characteristic of their apparent size in the deconvolved image. In each example, starting with Figure 6, the left panel shows the BLAST 250 μm image. On this are contours of the $^{13}\text{CO } J = 2 \rightarrow 1$ emission integrated over velocity ranges which highlight the CO clumps discussed in Appendix C of Schneider et al. (2006). Good correlations between BLAST emission and CO are revealed. The coordinate system chosen for these enlarged views is equatorial to facilitate comparison with the cutout regions in the annotated figures in Schneider et al. (2006). Star clusters, local sources of power, ionization, and pressure, are also noted (Section 3.1). In the right panel is the MIPS 24 μm image with contours of the 21 cm radio emission from the CGPS map shown in Figure 2. Motte et al. (2007) show pairs consisting of their 1.2 mm MAMBO image and the corresponding *MSX* 8.3 μm image, but with no contours of CO or radio emission. The MIPS image here is more sensitive to point-like sources, many coinciding with BLAST sources.

The regions are presented in order of the number of the DR H II region in the field, whose nominal position is marked with an arrow or filled triangle in the right hand panel. To locate the regions in the large overview image in Galactic coordinates (Figure 2), see the DR numbers marked there. Details of the

nature of the BLAST compact sources and their evolution are deferred to Sections 4 and 5.

DR7. The first region highlighted is a field including DR7, as shown in Figure 6. Immediately outside the DR7 H II region itself is a rim of BLAST emission containing several compact sources. The typical rim shaped geometry of the DR7 region has been formed by the star cluster (LK09) now residing in the cavity. Interestingly, the DR7 H II region along with its cluster is not associated with the contours of CO shown. This H II region has a recombination line velocity of -40 km s^{-1} (Lockman 1989) and CO velocity -50 km s^{-1} beyond the velocity coverage in Schneider et al. (2006), placing it well behind the Cyg OB2 complex, at 3.6 to 7.5 kpc, possibly in the Perseus arm. Another indicator of the larger distance is the lack of signature in the extinction map, which is based on colors of detectable 2MASS stars.

There are, however, several CO clumps that do coincide with BLAST emission and compact sources. The strong BLAST emission (with compact sources with MIPS counterparts) to the south coincides with clump 5. Not all clumps (which have different W) are easily seen in the BLAST emission (e.g., clumps 7, 8, and 9). The bright BLAST source at the top, in clump 1, has a compact H II region and a cometary tail linking it to Cyg OB2 (Section 5.1.2).

The emission at the upper left, associated with clump 2, is perhaps the most interesting, having a chaotic morphology in both MIPS and BLAST images (see also Figure 1). In the ridge we find three BLAST sources. Although in projection the center of Cyg OB2 is close by about $15'$ to the east (left), there is no sign of interaction; furthermore, there is a parallel ridge of H II emission on the right, suggesting illumination from that side. It coincides with G79.957+0.866 for which the recombination line velocity is -14.8 km s^{-1} (Lockman 1989), close to the CO velocity of -11 km s^{-1} . In the entire map, this CO cloud is unique in this velocity range < -10 km s^{-1} and not obviously connected to the other Cyg X molecular complexes. This then seems to be an object somewhat more distant, beyond the influence of Cyg OB2 (Section 5.1.2).

DR15. Figure 7 shows the fascinating region containing DR15 and the above-mentioned PAH arc. Schneider et al. (2006) argue that the DR15 molecular cloud complex near 0 km s^{-1} is being influenced by Cyg OB2 off to the upper left (see also

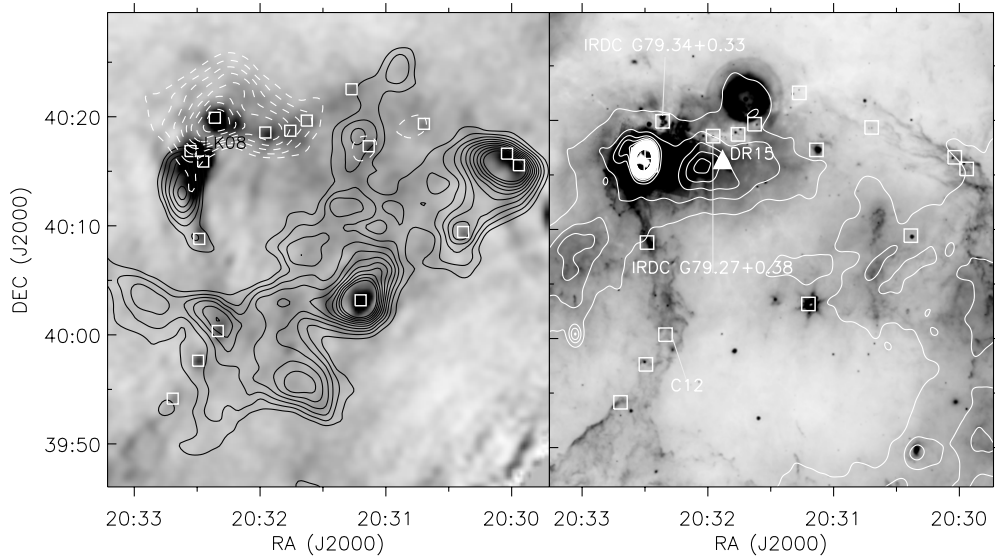


Figure 7. Same as Figure 6 but for the DR15 region. Dashed and solid CO contours for ranges -3 to 3 and 3 to 20 km s^{-1} , as used in Figure B.6 of Schneider et al. (2006).

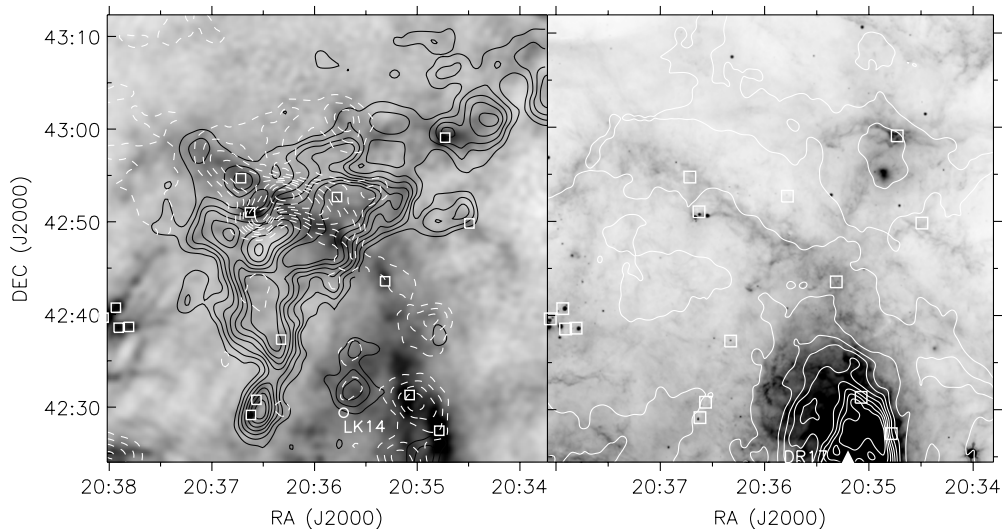


Figure 8. Same as Figure 6 but for DR17N. Solid and dashed CO contours are for ranges $1-6$ and $6-14$ km s^{-1} , as used in Figure B.1 of Schneider et al. (2006).

Section 5.1.2). This range also traces the IRDC ridge containing G79.34+0.33 and G79.27+0.38. As shown in Figure 3 and in more detail in Section 5.6.2, BLAST sees this cold ridge in emission and resolves several compact sources; in the MIPS image, some embedded protostars shine faintly through. Toward the center of this field is the protostar IRAS 20293+3952, part of a different CO system at positive velocity. The pair of BLAST sources to the upper right are associated with streamers in the MIPS image which appear to be “blown” from the right.

DR17N. The lower portion of Figure 8 shows the northern part of the extended DR17 region (see also Figure 2 and Section 5.4). A major arc-shaped extended structure crosses BLAST and MIPS images, and is seen in $8 \mu\text{m}$ PAH emission as well, confining the H II emission influenced by the OB clusters inside DR17. CO in the higher velocity range 6 to 14 km s^{-1} best traces the arc. The lower velocity system projects across this and has its own BLAST emission and compact sources.

DR17-Pillars. Schneider et al. (2006) identified “molecular pillars” (their Figure B.1) in the higher velocity range whose orientation points to the influence of the OB stars in DR17.

BLAST finds compact sources associated with these pillars as shown in Figure 9. Compared to other dust in DR17, the above-mentioned arc and these molecular pillars are cool (Figure 3). There is another H II region to the left in the image, with BLAST emission and compact sources along its interface as in DR7. This is the “Diamond Ring” (Marston et al. 2004) at an intermediate velocity (8 km s^{-1}), as described further in the DR21 discussion below.

DR20. Figure 10 shows DR20, which is at the end of a prominent ridge seen in the low-velocity CO (clump 1) and BLAST emission (see Figure 13 in Section 4.1 below). There are several BLAST compact sources here and in the complex to the west (clump 2, DR20W). The source in the middle of this image is associated with higher velocity gas (clump 3, DR20NW), as is more diffuse emission and other compact sources along the pillar toward the upper left (Section 5.1.1), possibly connected to the velocity system of the DR17 molecular pillars and arc.

DR21 and W75N. The DR21 and W75N regions shown in Figure 11 are obviously very active. The ridge of BLAST emission including DR21 and DR21(OH) points deceptively

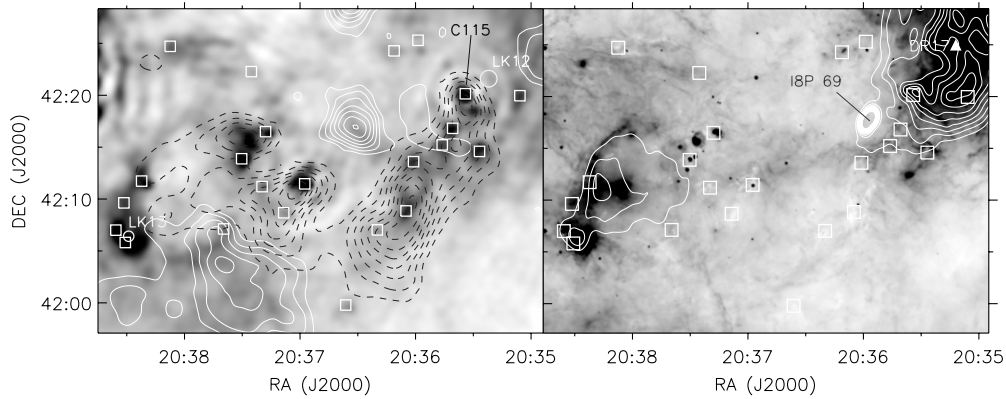


Figure 9. Same as Figure 8 but for the DR17-pillars region to its south (Schneider et al. 2006). Solid and dashed CO contours are for ranges 1–6 and 14–20 km s^{-1} , as used in Figure B.1 of Schneider et al. (2006). The long molecular pillar on the right is that labeled in Figure 3. A non-thermal extragalactic radio source 18P 69 (Wendker et al. 1991) also prominent in Figure 2 is marked.

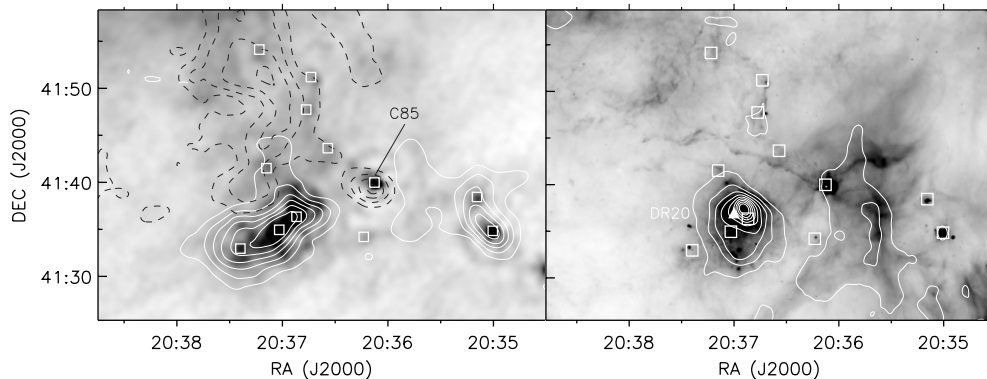


Figure 10. Same as Figure 6 but for DR20. Solid and dashed CO contours for ranges -10 to 1 and 6 – 14 km s^{-1} , as used in Figure B.2 of Schneider et al. (2006). They called the molecular clump on the right DR20W, in the same velocity system as DR20, and that containing C85, in a different velocity system of a prominent elephant trunk (Section 5.1.1) DR20NW.

to W75N. However, the peak CO emission on the ridge (clumps 3 and 4) and clump 8 containing the BLAST sources to the northwest of W75N are at -3 km s^{-1} (the low-velocity system), whereas clump 10 of W75N is in a quite different higher velocity component at $+10$ km s^{-1} . The low-velocity system is fairly widespread, including a complex to the southwest (overlapping the lower edge of the eastern-most DR17 molecular pillar) and extending down to DR23 and DR22 (Figure 12). The mass column density traced by BLAST correlates well with the CO emission. A fascinating feature is the extension of the DR21 ridge to the south, which shows up as a very narrow dark lane in the 24 μm image. This linear feature is at -4.5 km s^{-1} (see also Figure 28 in Section 5.6.2 below).

The higher velocity gas also contains prominent sources other than W75N, including the “Diamond” (clump 5) of the “Diamond Ring” (Marston et al. 2004). The more extended H II region along the “Ring” appears to be defined by both velocity systems.

DR22 and DR23. The CO cloud structures in the DR22 and DR23 regions shown in Figure 12 correlate well with the BLAST dust emission. Immediately to the southwest of DR23 is a dim bay in the MIPS image, where the main CO cloud (clump 1) of the low-velocity system confines the H II region. Along this interface are three BLAST compact sources, including C132, perhaps triggered by the earlier generation of stars in the DR23 cluster DB17. The two DR regions are interconnected by a CO filament (several clumps) in the lower velocity range. Along this filament there are BLAST compact sources and dark clouds, one (clump 3) with a protostellar nursery visible with MIPS

and IRAC (Section 5.6.2). For DR22, the complementary detail provided by IRAC emission (see Figure 23 in Section 5.2) confirms a classical PDR geometry, with the lower left being most edge on. The location of the BLAST sources, not just the compact H II region but all around the periphery, is suggestive of triggering.

4. PROPERTIES OF COMPACT SOURCES

4.1. Submillimeter-MIR SEDs

The SED for cold dust emission at temperature ~ 13 K and emissivity index $\beta = 1.5$ peaks at 250 μm , and so the combination of the three BLAST filters alone is well suited for determining the dust temperature. Nevertheless, there is a range of temperature among sources (Section 4.3) and it is always preferable to have a broad wavelength coverage spanning both sides of the peak. Fortunately, Cyg X is well covered by both blind and more-targeted surveys. An example of the multi-wavelength coverage is given in Figure 13. Clearly, resolution changes from map to map. Also, for the central source here, the centroid changes at shorter wavelengths (and in the radio). As described in Section 2.5, we have extracted flux densities consistently within the same size beam to characterize the same physical structure.

We fit an idealized single-temperature SED expressed by Equation (2) to data at all available wavelengths to determine temperature, mass, and total luminosity of each source (see Chapin et al. 2008 and Truch et al. 2008 for details). We adopt the same parameter values, namely $\kappa_0 = 10$ $\text{cm}^2 \text{g}^{-1}$, $r = 0.01$,

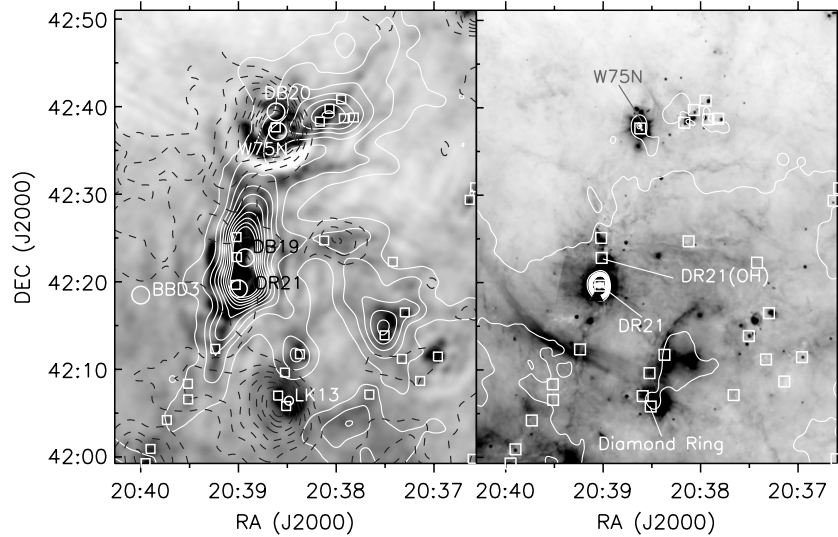


Figure 11. Same as Figure 6 but for DR21 and W75N regions. Solid and dashed CO contours are for ranges -10 to 1 and $6-14$ km s^{-1} as used in Figure B.3 of Schneider et al. (2006).

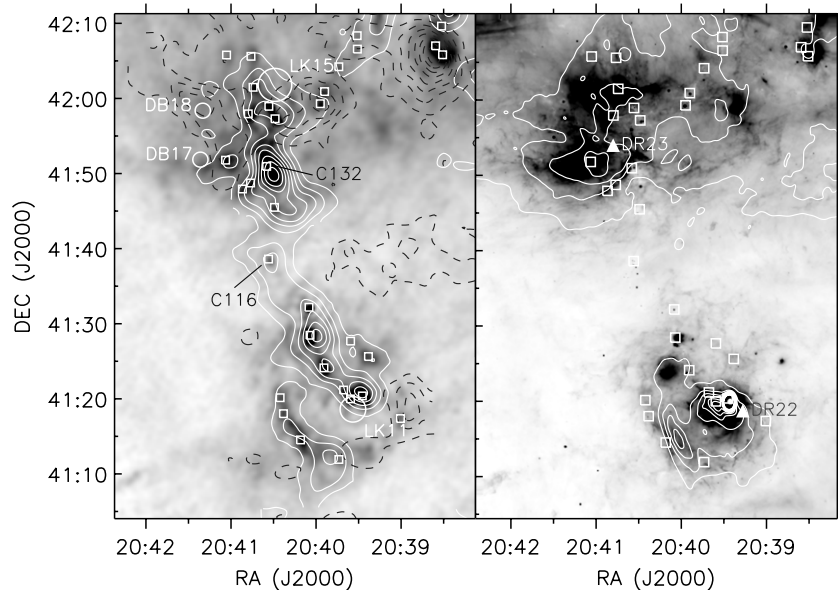


Figure 12. Same as Figure 11 but for DR22 and DR23 regions to its south.

and $\beta = 1.5$, and $D = 1.7$ kpc except for a few distant sources (Section 4.2). Single-temperature SEDs based on this value of β fit the data of typical sources well. One of the main systematic uncertainties is the value of $\kappa_0 r$, which is probably not known within a factor of two.

We treated ancillary photometric data for wavelengths less than $100 \mu\text{m}$ (see the Appendix) in the specific context of each individual SED, including them as upper limits where available/necessary. Upper limits come with an additional penalty function in the χ^2 minimization through a survival equation (Chapin et al. 2008; Truch et al. 2008).

BLAST filters have large spectral widths about the central wavelength. Color correction to monochromatic flux density is carried out as part of the SED fitting described by Truch et al. (2008). The factors are close to unity and fairly consistent from source to source for the range of temperatures encountered here: 1.04, 1.07, and 0.99 for 250, 350, and $500 \mu\text{m}$, respectively.

An example of a multi-wavelength SED fit is shown for C169 in Figure 14; this is one of the most luminous sources, W75N,

and one of the hottest, with a best-fit temperature for millimeter-FIR data of 36 K. In contrast to this, the SED of one of the colder sources is shown in Figure 15; this is C116 with a temperature of 17 K.

In Table 4, we record T , M , Σ , and L and their uncertainties for 170 individual sources, there being no entries for the 14 faint sources either near the map edge or with unreliable $500 \mu\text{m}$ flux densities. The uncertainties in T , M , and L , and the corresponding 68% confidence envelope of possible modified blackbodies, were obtained by the Monte Carlo technique described by Chapin et al. (2008).

4.2. Sources Behind Cyg OB2

There are eight sources at distances larger than the main Cyg OB2 complex, C27, C30, C33, and C35 in DR7 (Section 3.6), C59, C60, and C61 in G79.957+0.866 (Sections 3.6 and 5.1.2), and C71 in ECX6-27 (Sections 2.1 and 3.1). For calculating L and M , we assigned these rough distances of 6.8, 3.4, and 8.5 kpc, respectively, making L and M 16, 4, and 25 times

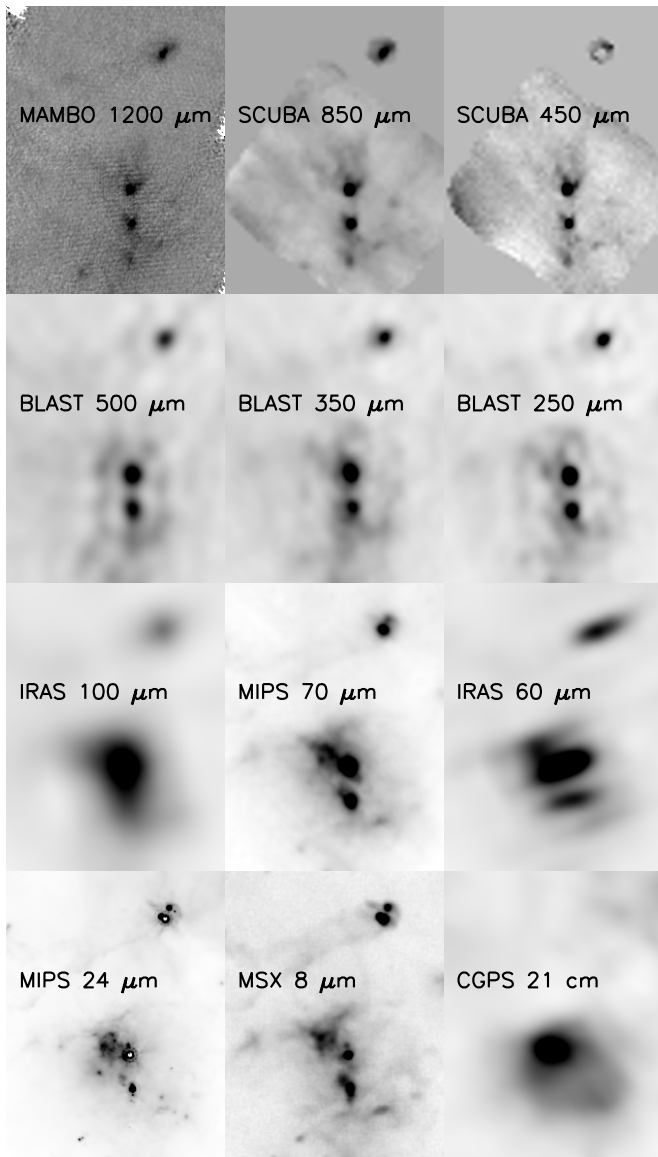


Figure 13. Thumbnails zooming in on a $14' \times 18'$ section of the BLAST survey area containing DR20 (Galactic coordinates; cf. Figure 10) at multiple wavelengths available for photometry. Relative appearance of structures changes because of different dust temperatures. The lowest in the vertical chain of three sources, seen only at wavelengths $500 \mu\text{m}$ and longer and so not cataloged as a BLAST source, must be quite cold. At *IRAS* $60 \mu\text{m}$ Infrared Galaxy Atlas (IGA, after HIRES processing) sources appear elliptical across the scan direction. At *IRAS* $100 \mu\text{m}$, the emission of crowded sources is often blended.

larger than if the Cyg OB2 distance of 1.7 kpc were adopted. This makes C30 the most luminous source and C71 the most massive. Both are of course integrated over much larger spatial scales than for the sources at 1.7 kpc. Note that L/M and T are preserved.

4.3. Temperature

Temperature is obtained directly as a free parameter of the SED fit. Figure 16 shows the temperature histogram of BLAST sources detected in the Cyg X field. The superimposed histogram is for the Vulpecula region (Chapin et al. 2008). The median of the distribution in Cyg X is about 22 K which is comparable to the median for Vulpecula at 21 K. Recall that these are for $\beta = 1.5$. A somewhat higher β combined with a temperature distribution might be a more realistic model

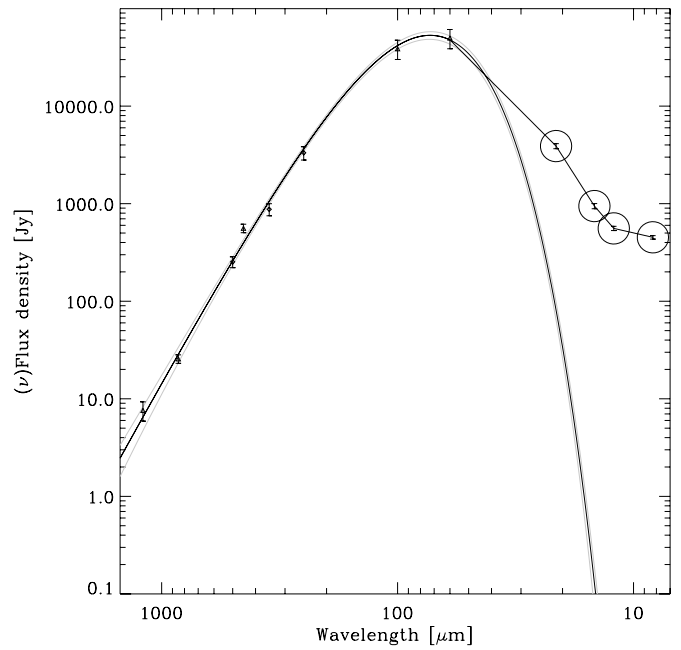


Figure 14. SED of C169 (W75N). To show intuitively where the most important contributions to the bolometric luminosity arise, this particular log-log plot uses νF_ν , obtained by multiplying flux densities by ν/ν_{250} with ν_{250} corresponding to $250 \mu\text{m}$. The central solid curve shows the best-fit modified blackbody using data at $\lambda \geq 60 \mu\text{m}$ with $\beta = 1.5$. The *MSX* data shown by the circles are not used in the fit but are important in constraining L_{bol} (Section 4.5). The bracketing curves represent the 68% confidence envelope of modified blackbody models obtained from Monte Carlo simulations. Best-fit parameters are $T = 36.2 \pm 3.6 \text{ K}$, $M = (7.6 \pm 1.2) \times 10^2 M_\odot$, and $L = (6.2 \pm 2.2) \times 10^4 L_\odot$.

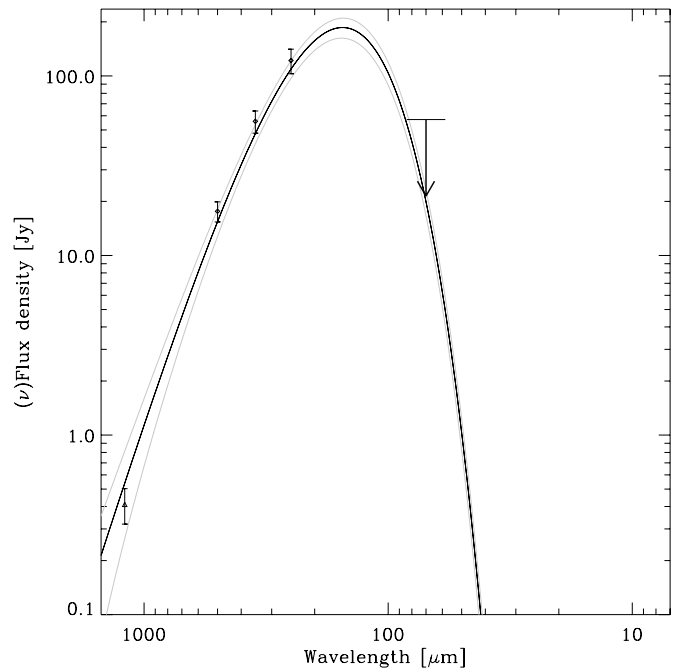


Figure 15. Like Figure 14 but for one of the colder sources in Cyg X, C116. At $70 \mu\text{m}$ we plot the 1σ (arrow) and 3σ upper limits (the Appendix); upper limits constrain the SED through a penalty function (Chapin et al. 2008). Best-fit parameters are $T = 17.1 \pm 0.9 \text{ K}$, $M = (1.7 \pm 0.2) \times 10^2 M_\odot$, and $L = (2.2 \pm 0.4) \times 10^2 L_\odot$. The $24 \mu\text{m}$ MIPS image in the upper panel of Figure 26 reveals a deeply embedded stellar nursery, but it is not yet very luminous.

(Netterfield et al. 2009), though in the simple model here there is a single T . For $\beta = 2$, the temperatures would be about 10% lower.

Table 4
Results from SED Fits

BLAST ID	T (K)	M ($100 M_{\odot}$)	Σ (g cm^{-2})	L ($100 L_{\odot}$)	L_{bol} ($100 L_{\odot}$)
C0	15.5 ± 0.7	1.8 ± 0.4	0.033	1.4 ± 0.2	...
C1	40.1 ± 4.0	1.9 ± 0.4	0.121	277.2 ± 100.7	489.4
C3	16.6 ± 1.1	1.4 ± 0.3	0.021	1.6 ± 0.4	...
C4	17.5 ± 0.7	1.7 ± 0.3	0.022	2.6 ± 0.4	...
C5	13.2 ± 1.3	0.5 ± 0.2	0.022	0.1 ± 0.0	...
C6	19.6 ± 0.6	0.7 ± 0.1	0.009	1.8 ± 0.2	2.0
C7	25.8 ± 0.8	2.6 ± 0.3	0.084	33.4 ± 3.3	50.2
C8	17.3 ± 1.6	2.2 ± 0.6	0.038	3.1 ± 1.0	...
C9	20.4 ± 2.0	0.4 ± 0.1	0.006	1.3 ± 0.4	...
C10	15.7 ± 1.3	4.1 ± 1.0	0.051	3.4 ± 1.0	...
C11	25.7 ± 0.8	0.4 ± 0.1	0.008	4.4 ± 0.4	...
C12	20.9 ± 0.6	0.4 ± 0.1	0.007	1.8 ± 0.2	...
C13	15.7 ± 0.8	0.8 ± 0.2	0.014	0.7 ± 0.1	...
C14	29.9 ± 1.7	0.1 ± 0.0	0.003	3.8 ± 0.6	4.5
C15	20.8 ± 0.9	2.7 ± 0.5	0.024	10.5 ± 1.1	15.3
C16	23.7 ± 0.6	2.1 ± 0.3	0.096	16.5 ± 1.4	...
C17	21.5 ± 1.8	0.2 ± 0.0	0.005	1.0 ± 0.3	...
C18	15.1 ± 2.0	0.8 ± 0.3	0.015	0.5 ± 0.2	...
C19	32.5 ± 1.1	0.2 ± 0.0	0.003	9.8 ± 1.2	10.1
C20	23.6 ± 3.8	0.5 ± 0.2	0.006	4.1 ± 1.8	...
C21	15.2 ± 0.6	1.6 ± 0.3	0.009	1.1 ± 0.1	...
C22	14.7 ± 1.2	2.5 ± 0.7	0.021	1.5 ± 0.3	2.3
C23	15.0 ± 1.6	2.2 ± 0.8	0.015	1.5 ± 0.5	...
C25	15.1 ± 1.2	2.4 ± 0.5	0.018	1.6 ± 0.5	...
C26	13.4 ± 0.9	3.7 ± 0.6	0.059	1.3 ± 0.3	...
C27 ^a	40.1 ± 4.2	0.4 ± 0.1	0.007	62.3 ± 24.9	55.4
C28	47.0 ± 9.7	0.4 ± 0.1	0.009	144.3 ± 211.5	113.5
C29	17.3 ± 2.7	0.4 ± 0.2	0.007	0.5 ± 0.2	...
C30 ^a	37.7 ± 4.6	1.1 ± 0.5	0.020	110.6 ± 37.2	102.5
C31	18.0 ± 2.3	1.8 ± 0.6	0.033	3.3 ± 1.2	...
C32	46.2 ± 2.8	1.1 ± 0.2	0.024	330.7 ± 72.1	...
C34	25.4 ± 1.3	0.4 ± 0.1	0.006	4.3 ± 0.7	...
C36	25.5 ± 1.1	2.6 ± 0.4	0.039	30.6 ± 4.3	...
C37	18.8 ± 2.5	0.4 ± 0.2	0.011	1.0 ± 0.4	...
C38	37.6 ± 1.9	0.4 ± 0.1	0.014	38.3 ± 6.0	48.7
C39	19.4 ± 2.8	0.8 ± 0.3	0.010	2.0 ± 1.3	...
C40	15.5 ± 1.2	1.7 ± 0.5	0.009	1.3 ± 0.3	...
C41	35.1 ± 1.9	0.1 ± 0.0	0.002	4.4 ± 0.9	5.4
C42	13.0 ± 1.6	2.0 ± 0.8	0.027	0.6 ± 0.2	...
C43	28.9 ± 1.1	0.4 ± 0.1	0.010	8.4 ± 0.9	...
C44	23.0 ± 0.5	0.4 ± 0.1	0.003	3.0 ± 0.2	...
C45	18.4 ± 0.3	1.1 ± 0.1	0.012	2.2 ± 0.2	...
C46	14.9 ± 0.7	1.2 ± 0.3	0.004	0.8 ± 0.1	...
C47	11.0 ± 0.9	2.6 ± 0.7	0.032	0.3 ± 0.1	0.9
C48	11.8 ± 1.2	3.8 ± 1.3	0.025	0.7 ± 0.2	...
C49	27.0 ± 0.9	0.1 ± 0.0	0.005	2.1 ± 0.2	2.8
C50	15.3 ± 1.7	1.0 ± 0.3	0.010	0.8 ± 0.2	...
C51	22.2 ± 1.0	0.7 ± 0.1	0.026	3.7 ± 0.5	5.0
C52	17.8 ± 3.0	0.3 ± 0.1	0.005	0.5 ± 0.1	1.2
C53	27.8 ± 1.1	0.2 ± 0.0	0.005	4.2 ± 0.5	4.9
C54	11.5 ± 1.1	1.2 ± 0.4	0.055	0.2 ± 0.0	...
C55	30.2 ± 1.3	1.6 ± 0.2	0.117	48.2 ± 6.2	52.9
C57	28.8 ± 1.4	0.1 ± 0.0	0.004	2.3 ± 0.4	3.6
C58	28.3 ± 1.0	0.2 ± 0.0	0.007	3.3 ± 0.4	4.1
C59 ^a	17.6 ± 1.9	1.7 ± 0.5	0.053	2.6 ± 0.9	6.8
C60 ^a	16.4 ± 1.3	3.8 ± 1.6	0.021	4.0 ± 2.4	...
C61 ^a	25.7 ± 0.9	1.8 ± 0.2	0.029	22.8 ± 2.9	24.8
C63	17.5 ± 0.7	1.1 ± 0.3	0.006	1.7 ± 0.2	...
C64	30.6 ± 1.7	0.1 ± 0.0	0.006	4.3 ± 0.6	6.0
C65	24.4 ± 0.9	1.1 ± 0.2	0.008	10.0 ± 0.9	...
C66	30.5 ± 1.7	0.1 ± 0.0	0.003	2.6 ± 0.4	8.0
C67	25.5 ± 0.8	0.4 ± 0.0	0.009	4.9 ± 0.5	5.6
C68	17.2 ± 1.5	0.6 ± 0.1	0.006	0.8 ± 0.3	...
C69	22.4 ± 0.6	0.1 ± 0.0	0.008	0.9 ± 0.1	...
C70	34.3 ± 2.3	0.0 ± 0.0	0.001	2.6 ± 0.4	...

Table 4
(Continued)

BLAST ID	T (K)	M ($100 M_{\odot}$)	Σ (g cm^{-2})	L ($100 L_{\odot}$)	L_{bol} ($100 L_{\odot}$)
C71 ^a	30.7 ± 1.3	0.9 ± 0.1	0.016	30.6 ± 4.5	31.3
C73	33.4 ± 1.5	1.6 ± 0.2	0.030	84.3 ± 17.1	87.6
C74	23.2 ± 2.6	0.3 ± 0.3	0.006	2.3 ± 0.7	3.1
C75	34.8 ± 2.6	0.1 ± 0.0	0.002	6.2 ± 1.3	6.3
C76	28.4 ± 1.0	0.8 ± 0.1	0.016	18.3 ± 2.1	21.8
C78	21.9 ± 2.9	0.2 ± 0.1	0.003	0.8 ± 0.3	...
C79	27.4 ± 1.4	0.2 ± 0.0	0.002	2.8 ± 0.4	...
C80	30.0 ± 1.0	1.5 ± 0.2	0.056	43.4 ± 5.1	48.9
C81	13.5 ± 1.2	0.9 ± 0.3	0.017	0.3 ± 0.1	...
C82	11.5 ± 1.3	1.5 ± 0.8	0.037	0.2 ± 0.1	...
C83	28.8 ± 1.1	0.5 ± 0.1	0.007	10.8 ± 1.3	11.6
C84	23.4 ± 0.8	0.5 ± 0.1	0.006	3.7 ± 0.4	...
C85	29.9 ± 1.0	1.2 ± 0.1	0.053	35.4 ± 5.0	51.8
C86	16.0 ± 1.9	2.3 ± 0.8	0.025	2.1 ± 0.6	...
C87	26.8 ± 1.0	1.8 ± 0.2	0.058	28.0 ± 4.9	33.6
C88	32.5 ± 1.1	1.9 ± 0.2	0.091	85.7 ± 11.3	106.0
C89	25.7 ± 1.2	0.1 ± 0.0	0.002	1.8 ± 0.3	...
C90	16.8 ± 2.3	3.3 ± 1.7	0.019	4.0 ± 1.3	...
C91	17.2 ± 1.2	1.5 ± 2.3	0.008	2.0 ± 0.4	...
C92	39.3 ± 5.5	1.9 ± 0.7	0.024	240.6 ± 91.8	323.2
C93	22.0 ± 2.1	1.8 ± 0.5	0.015	9.7 ± 2.1	...
C95	24.4 ± 1.7	0.3 ± 0.1	0.001	2.4 ± 0.6	...
C97	21.0 ± 1.2	2.6 ± 0.5	0.013	10.6 ± 2.0	...
C98	19.1 ± 0.5	2.1 ± 0.3	0.009	5.1 ± 0.4	...
C99	25.3 ± 0.9	1.2 ± 0.2	0.007	13.7 ± 2.0	...
C100	23.5 ± 0.6	0.3 ± 0.0	0.002	1.9 ± 0.2	...
C101	26.3 ± 0.8	1.6 ± 0.2	0.013	21.9 ± 2.4	23.0
C102	22.4 ± 0.7	0.6 ± 0.1	0.007	3.4 ± 0.3	...
C104	28.2 ± 0.9	1.8 ± 0.2	0.027	37.7 ± 3.8	44.7
C105	19.9 ± 1.7	0.7 ± 0.2	0.007	2.1 ± 0.6	...
C106	15.6 ± 1.3	2.0 ± 0.5	0.018	1.6 ± 0.4	...
C107	22.2 ± 0.6	1.3 ± 0.2	0.071	7.3 ± 0.7	...
C108	15.4 ± 0.6	6.4 ± 1.1	0.029	4.8 ± 0.7	...
C109	16.6 ± 2.8	0.7 ± 0.2	0.003	0.8 ± 0.4	...
C110	28.7 ± 0.9	0.7 ± 0.1	0.006	15.5 ± 1.5	...
C111	23.6 ± 1.4	0.6 ± 0.1	0.008	5.0 ± 0.9	...
C112	19.5 ± 0.5	1.4 ± 0.2	0.015	3.9 ± 0.4	...
C113	17.7 ± 0.5	1.1 ± 0.2	0.012	1.7 ± 0.2	...
C114	19.6 ± 0.8	1.0 ± 0.2	0.021	2.7 ± 0.4	...
C115	25.6 ± 0.8	2.2 ± 0.3	0.115	27.5 ± 3.1	31.4
C116	17.1 ± 0.9	1.7 ± 0.2	0.022	2.2 ± 0.4	...
C117	32.1 ± 0.9	0.8 ± 0.1	0.005	34.6 ± 3.6	...
C118	18.3 ± 2.4	0.2 ± 0.5	0.006	0.4 ± 0.2	...
C119	21.8 ± 0.5	3.0 ± 0.5	0.115	15.2 ± 1.5	...
C120	17.1 ± 0.7	1.3 ± 0.3	0.009	1.8 ± 0.3	...
C121	13.8 ± 2.2	1.3 ± 0.6	0.033	0.5 ± 0.3	...
C122	12.9 ± 1.2	5.4 ± 1.5	0.079	1.5 ± 0.4	...
C123	21.0 ± 0.9	1.4 ± 0.2	0.008	5.9 ± 0.8	...
C124	22.4 ± 1.2	0.2 ± 0.0	0.001	1.4 ± 0.3	...
C125	28.1 ± 0.8	0.2 ± 0.0	0.002	4.4 ± 0.6	5.0
C126	21.9 ± 1.1	2.7 ± 0.4	0.019	14.0 ± 3.4	15.1
C127	33.9 ± 3.7	1.7 ± 0.3	0.006	95.1 ± 71.1	91.3
C128	27.1 ± 1.6	0.3 ± 0.1	0.012	5.4 ± 0.9	6.9
C129	20.3 ± 2.3	2.7 ± 0.7	0.026	9.1 ± 3.8	25.7
C130	23.2 ± 1.2	0.5 ± 0.1	0.008	3.7 ± 0.7	...
C132	27.2 ± 1.5	2.7 ± 0.5	0.015	46.0 ± 9.3	...
C133	23.1 ± 1.3	0.6 ± 0.2	0.004	4.5 ± 0.9	...
C134	22.7 ± 0.6	1.0 ± 0.1	0.009	6.4 ± 0.6	...
C135	25.5 ± 1.3	0.4 ± 0.1	0.011	5.3 ± 0.8	7.5
C136	14.6 ± 1.1	5.1 ± 1.2	0.040	2.9 ± 0.6	...
C139	20.7 ± 0.7	0.4 ± 0.1	0.011	1.4 ± 0.2	...
C140	22.0 ± 0.6	1.7 ± 0.2	0.009	9.1 ± 1.0	...
C141	21.5 ± 0.6	1.7 ± 0.2	0.041	8.3 ± 0.7	8.9
C142	21.6 ± 1.1	0.5 ± 0.1	0.007	2.3 ± 0.4	...

Table 4
(Continued)

BLAST ID	T (K)	M ($100 M_{\odot}$)	Σ (g cm^{-2})	L ($100 L_{\odot}$)	L_{bol} ($100 L_{\odot}$)
C143	14.6 ± 1.5	1.6 ± 0.5	0.034	0.9 ± 0.3	...
C144	19.4 ± 0.7	0.5 ± 0.1	0.006	1.4 ± 0.2	...
C145	21.9 ± 1.2	1.1 ± 0.1	0.026	5.6 ± 1.2	...
C146	13.8 ± 1.9	5.8 ± 2.7	0.027	2.4 ± 0.8	...
C147	13.3 ± 2.5	1.7 ± 1.9	0.022	0.6 ± 0.3	...
C148	21.9 ± 0.6	0.4 ± 0.0	0.002	1.8 ± 0.2	...
C149	19.5 ± 0.8	1.1 ± 0.2	0.022	3.0 ± 0.6	...
C150	19.3 ± 0.9	0.3 ± 0.1	0.004	0.8 ± 0.1	...
C151	20.2 ± 0.9	0.8 ± 0.2	0.014	2.7 ± 0.4	...
C152	18.9 ± 0.8	0.6 ± 0.1	0.006	1.5 ± 0.2	...
C153	19.7 ± 2.5	0.7 ± 0.3	0.019	2.2 ± 0.7	...
C154	17.4 ± 0.8	1.8 ± 0.3	0.013	2.7 ± 0.4	...
C155	36.0 ± 4.4	8.8 ± 2.4	0.432	697.6 ± 250.4	776.6
C156	26.1 ± 0.7	0.4 ± 0.1	0.004	5.5 ± 0.6	...
C157	26.7 ± 2.0	18.8 ± 2.4	1.019	291.6 ± 108.6	319.3
C158	24.6 ± 0.8	0.2 ± 0.0	0.001	1.5 ± 0.2	...
C159	28.6 ± 0.8	0.8 ± 0.1	0.007	17.0 ± 1.7	...
C160	25.9 ± 2.3	11.2 ± 2.2	0.903	145.3 ± 47.4	152.0
C161	21.4 ± 2.9	0.4 ± 0.1	0.004	1.7 ± 0.7	...
C162	12.4 ± 1.9	2.4 ± 1.2	0.035	0.5 ± 0.2	...
C163	26.4 ± 2.7	0.3 ± 0.1	0.010	4.9 ± 2.3	5.8
C164	25.6 ± 3.2	0.3 ± 0.1	0.007	4.1 ± 1.8	...
C165	27.3 ± 1.5	0.8 ± 0.1	0.012	14.0 ± 2.5	17.3
C166	24.0 ± 0.6	1.2 ± 0.2	0.013	10.0 ± 1.0	...
C167	20.2 ± 2.1	3.2 ± 0.8	0.045	10.6 ± 2.8	...
C168	24.4 ± 1.3	0.4 ± 0.2	0.014	3.7 ± 0.5	4.9
C169	36.2 ± 3.6	7.6 ± 1.2	0.689	624.4 ± 229.4	664.9
C170	22.9 ± 0.7	0.4 ± 0.0	0.002	2.5 ± 0.3	...
C171	27.1 ± 0.9	0.5 ± 0.1	0.011	8.3 ± 1.0	11.5
C172	13.7 ± 1.6	2.0 ± 0.6	0.069	0.8 ± 0.3	...
C173	10.2 ± 1.1	3.5 ± 1.2	0.007	0.3 ± 0.1	...
C174	18.6 ± 2.0	0.7 ± 0.2	0.039	1.4 ± 0.7	...
C175	13.3 ± 1.1	5.5 ± 1.4	0.034	1.8 ± 0.5	...
C176	25.2 ± 1.7	0.4 ± 0.1	0.004	4.0 ± 0.9	...
C177	24.6 ± 0.8	1.3 ± 0.2	0.013	12.4 ± 1.5	...
C179	14.1 ± 2.1	4.3 ± 2.3	0.035	2.0 ± 0.7	...
C180	42.6 ± 2.4	0.2 ± 0.0	0.006	34.4 ± 6.5	49.4
C181	9.3 ± 1.3	6.2 ± 3.5	0.084	0.3 ± 0.1	...
C182	29.4 ± 1.0	0.6 ± 0.1	0.007	15.3 ± 1.8	...
C183	25.0 ± 2.2	0.7 ± 0.7	0.023	7.1 ± 1.0	10.2

Note. ^a M and L not corrected for different distance than Cyg OB2 (see Section 4.2).

4.4. Mass

Source mass M is obtained from the best-fit amplitude and temperature of the SED and Equation (2), which shows how any uncertainties in κ , r , and D are propagated as systematic errors. Recall that our sources typically have an apparent FWHM of $1'$, which corresponds to about 0.5 pc. This is more characteristic of a “clump” mass, as distinguished from the high-resolution measurements of “cores” by Motte et al. (2007). Note that the values adopted for κ_0 and β do provide consistency with the 1.2 mm opacity of $1 \text{ cm}^2 \text{ g}^{-1}$ adopted by Motte et al. (2007), following Ossenkopf & Henning (1994). However, without the multi-wavelength coverage, they were forced to adopt a temperature. From these derived masses, ranging from 10 to $2000 M_{\odot}$, the BLAST sources have the potential to form (many) massive stars under favorable physical conditions. For example, in the context of the turbulent core model, Krumholz & McKee (2008) predicted a critical surface density for the formation of

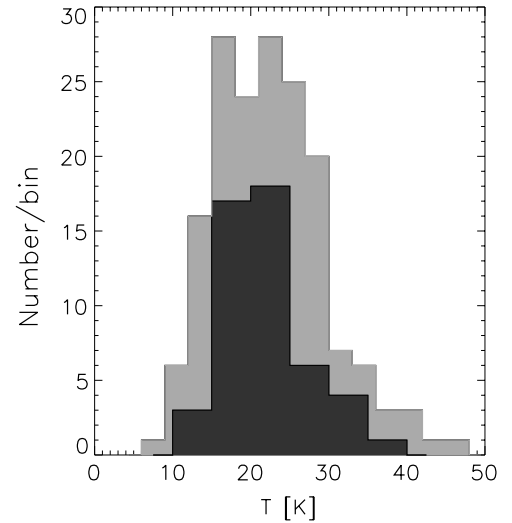


Figure 16. Light gray histogram shows the distribution of source temperatures for the Cyg X field. Dark overplotted histogram is for the BLAST05 Vulpecula field (Chapin et al. 2008).

massive stars, as opposed to fragmentation into much lower masses (see Section 6.3 for further discussion).

The surface column density for fragments of radius R is given by

$$\Sigma = 2.7 \times 10^{-2} \left(\frac{M}{100 M_{\odot}} \right) \left(\frac{R}{0.5 \text{ pc}} \right)^{-2} \text{ g cm}^{-2}. \quad (3)$$

We adopt the deconvolved FWHM of the brightness profile as the radius. Surface densities of the cores (and clumps) of Motte et al. (2007) are listed in Table 3. (Note that the assumption of a temperature of 20 K for the cores means that the surface density reported might be an upper limit.) As discussed below, the surface density of BLAST clumps is somewhat lower, in part because of the low angular resolution which limits the ability to discern sub-structure at small R .

Following Equation (2) of Motte et al. (2007), the volume-averaged molecular hydrogen density is

$$\langle n_{\text{H}_2} \rangle = 3.3 \times 10^3 M / (100 M_{\odot}) \text{ cm}^{-3}. \quad (4)$$

Because of the BLAST beam size, these clump densities are more than an order of magnitude lower than for the embedded cores found by Motte et al. (2007). The corresponding free-fall timescale (Stahler & Palla 2005) is also longer,

$$t_{\text{ff}} = 5.6 \times 10^5 [M / (100 M_{\odot})]^{-1/2} \text{ yr}. \quad (5)$$

4.5. Luminosity

The best-fit single-temperature SED is a good and integrable interpolating function from which the far-infrared luminosity L is derived analytically. The frequencies at which the most important contributions arise can be visualized most readily when the SED is plotted in the νF_{ν} form like in Figure 14.

Often the short-wavelength mid-infrared data lie in excess of this simple SED and to allow for that we simply integrate the piecewise curve connecting that short-wavelength data where available. This is normally a small contribution to the total bolometric luminosity L_{bol} (Table 4). For example, for W75N (C169, Figure 14), L rises from 6.2 to $6.6 \times 10^4 L_{\odot}$. In the context of position in the logarithmic L - M plot below, this is not a big correction.

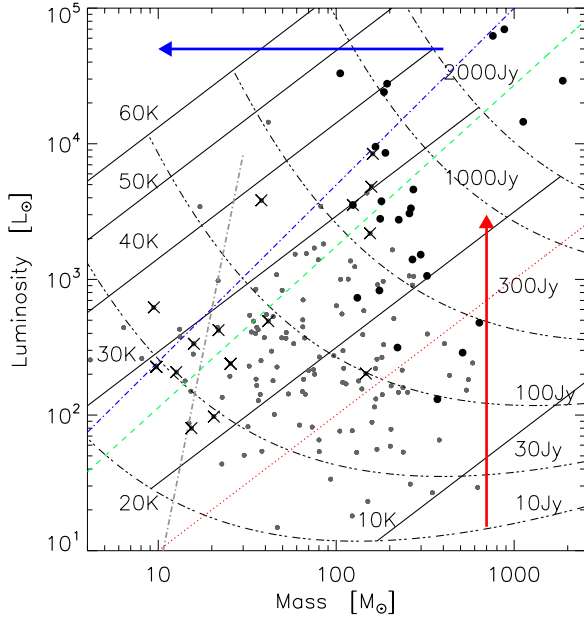


Figure 17. Distribution of BLAST sources in the Cyg OB2 complex in the L - M plane. Those on the right of the steep dash-dot (gray) curve are above the Bonner–Ebert mass. Solid diagonal lines are loci of constant T or L/M . The dotted line (red) is $L = M$. Dot-dash curves “orthogonal” to these are for constant $250\ \mu\text{m}$ flux density. Dash (green) and dot-dash (blue) lines denote the location of sources powered by accretion and nuclear burning, respectively, as derived empirically in Figure 9 of Molinari et al. (2008). Cool sources discovered by BLAST with low L/M still are externally heated (stage E). These appear to be gravitationally bound, but have no significant internal power from star formation yet. The vertical arrow indicates the direction of evolution in this diagram as protostar formation takes hold within a clump. The horizontal arrow indicates the direction of evolution as the embedding material is dispersed by the formed stars/cluster, assuming the surrounding dust still reprocesses most of the internally generated L . Otherwise (as appears to be the case), the re-radiated L , measured here, is less. Black filled circles are BLAST sources corresponding to clumps of Motte et al. (2007, Table 3). Crosses are sources with morphological evidence of mass stripping from radiative interaction with Cyg OB2; some at lower luminosity exhibit the effects of external ionization.

(A color version of this figure is available in the online journal.)

The luminosity range in Cyg X is large, extending over three orders of magnitude from $7 \times 10^4 L_\odot$ down to $40 L_\odot$, beyond which we lose many sources in the (cirrus) noise (note that the approximate $250\ \mu\text{m}$ completeness line is about 30 Jy; see Chapin et al. 2008).

4.6. The L - M Diagram

The L - M diagram can be exploited to assess evolutionary stages (Molinari et al. 2008). Figure 17 shows our results in the L - M plane for those sources at the distance of Cyg OB2; the results for the few distant sources (Section 4.2) are in Figure 18 (note the scales to larger masses and luminosities).

Lines of constant T are diagonal lines (constant L/M) in this L - M diagram: a mass M radiates a predictable L , depending on κ_{0r} and β . To be consistent with the analytical loci, we plot L from the SED fit rather than the only slightly larger L_{bol} . “Orthogonal” to these diagonal lines are loci of constant $250\ \mu\text{m}$ flux density. Note that there are relatively fewer sources between the 30 and 10 Jy loci because of the growing effect of cirrus noise.

In this diagram, the “error ellipse” determined by the Monte Carlo technique is elongated along the locus for the source flux density and the extent is well described by $\Delta T/T$. We examined the histogram of $\Delta T/T$ and rejected outliers >0.19 ; these were

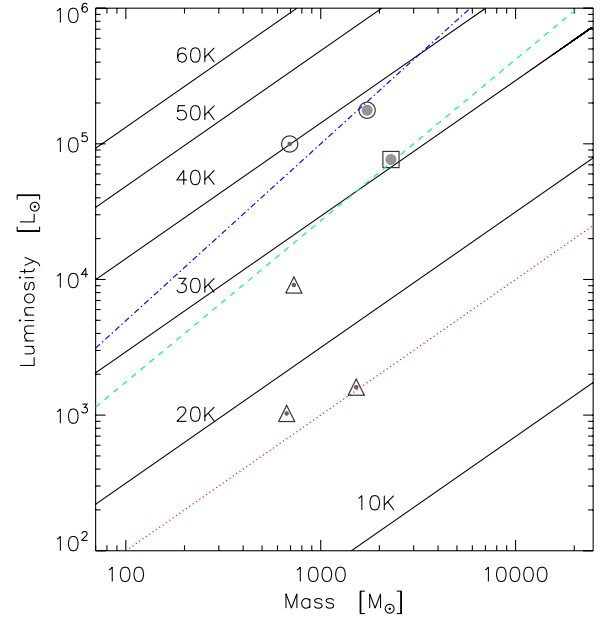


Figure 18. Same as Figure 17, but for sources more distant than Cyg OB2 (Section 4.2). Triangles, circles, and square represent sources about 3.4, 6.8, and 8.5 kpc away, respectively. These include the most luminous and most massive sources in the survey.

(A color version of this figure is available in the online journal.)

18 sources with poorly constrained SEDs, usually lacking in definitive data near $100\ \mu\text{m}$ combined with their poor image quality at $500\ \mu\text{m}$.

The dashed and dot-dash thick lines, roughly lines of constant T , are the loci obtained empirically by Molinari et al. (2008) for sources thought to be in the accretion stage and the later nuclear burning stage (when envelope dispersal begins), respectively. For single low-mass stars, these would correspond to the spectroscopically defined “Class 0” and “Class 1,” respectively. With BLAST, we detect sources of the size of “clumps” and furthermore even smaller angular-size high-mass “cores” are capable of forming multiple stars. This warns against a simple interpretation of this diagram based on single-star evolutionary tracks, although it is possible that once high-mass stars form, the most massive will dominate the luminosity and ionization (this will depend on the IMF, star formation efficiency, and also small-number statistics).

We think that the most illuminating way to think of pre-stellar evolution in this diagram is in terms of the energy source for the clump, which determines the appropriate equilibrium temperature T for the approximate SED. In the very earliest stages being sought in submillimeter surveys, the energy source for the clumps is predominantly external, namely the impinging interstellar radiation field. In Cyg X, the radiation field is in principle higher than in the local ISM because of all the massive stars that have already formed, but this radiation is attenuated by the dusty molecular material in which the pre-stellar clumps are embedded. A useful point of reference is the equilibrium temperature corresponding to $L = M$, which for the adopted κ_{0r} and β (Section 4.1) is 16.2 K.

Massive sources located below this $L = M$ locus (see Section 5.6) still can have substantial L by virtue of a lot of mass, but cannot have any predominant internal source of energy (either accretion or nuclear), and so could be called “starless.” This term is probably best avoided for these clumps, within which there might actually be a few low-mass stars

already forming and detectable by sensitive telescopes like *Spitzer* (Section 6.2). The key consideration is what is the dominant source of energy determining T . As mentioned in the introduction, these clumps could be said to be in stage E (“E” for “external” or “earliest”), which seems to us a better terminology than “starless,” or “Class -1 ” for single-star pre-stellar cores. Figure 17 shows that there are many clumps in this stage. We can calculate the Bonner–Ebert mass, above which (within the assumptions) a clump is gravitationally unstable (e.g., Stahler & Palla 2005):

$$M_{\text{BE}} = 1 [T_{\text{g}}/(10 \text{ K})]^{3/2} [n_{\text{H}_2}/(10^4 \text{ cm}^{-3})]^{-1/2} M_{\odot}. \quad (6)$$

Thus, assuming that $T_{\text{g}} \leq T$, the low-luminosity, low-temperature BLAST clumps are unstable. As discussed below, in the simplest theory they would evolve into the higher luminosity, higher temperature clumps seen higher in the diagram at the same M .

As gravitational collapse progresses, more and more mass accretes into protostellar cores. The actual luminosity in this accretion-powered stage depends on the accretion rate and the potential well. In recognition of the underlying energetics, these clumps could be said to be in stage A (“A” for accretion-powered). Consistent with this interpretation, sources observed to be in this part of the L – M diagram have a characteristic signature of active accretion (Section 5.5).

Ultimately, nuclear fusion becomes the dominant source of power. Unlike for low-mass stars, massive pre-main-sequence stars probably continue accreting after first beginning nuclear burning, increasing their mass further (Zinnecker & Yorke 2007). When this accretion ends, an individual star is at its final position on the zero-age main sequence (ZAMS). It will still be embedded, and so optically obscured, but its vast power reprocessed will produce a relatively warm far-infrared source. For sufficiently massive stars, significant ionization of the surroundings will ensue, producing a hypercompact H II region. There could be many within a single clump, for example (Rivera-Ingraham et al. 2010). These clumps would appear in the L – M diagram near the empirical nuclear burning locus (see Section 5.4).

As the massive stars clear their local environment through the expansion of the H II region and via radiation pressure on dust (successively ultracompact then compact H II regions), the individual objects will become more extended far-infrared sources. The strong short-wavelength stellar radiation field will enhance both thermal emission and non-equilibrium emission from PAHs in nearby PDR material, making the SED of the integrated re-emission of the clump broader and more complex. Evolution in the L – M diagram will initially be at constant L with decreasing M ; ultimately, the optical depth and/or covering factor would decrease so that the reprocessed L will fall.

A stellar cluster with an extended H II region would emerge. Even though such clusters are found in Cyg X, they are not detected as compact BLAST sources and so do not appear in the L – M diagram; only objects like their precursors would.

4.7. Census

It is interesting to ask how many objects are in each evolutionary stage. To address this, we have concentrated on the mass range between 50 and 500 M_{\odot} where there is an abundance of sources (100 omitting the sources more distant than Cyg OB2) and the lower luminosity end is minimally affected by completeness, at least down to $L = M$. Figure 19 presents a histogram

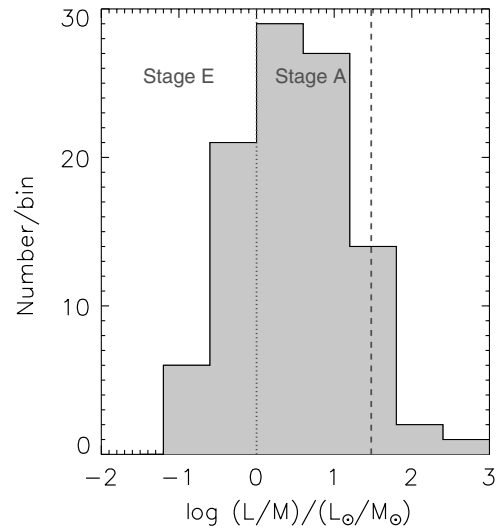


Figure 19. Histogram of L/M ratio of the Cyg X compact sources in the mass range 50–500 M_{\odot} . The dotted vertical line separates stage E sources below the locus $L = M$ in Figure 17. Most sources are in the accretion-powered stage A, up to the dashed line ($L/M \approx 30 L_{\odot}/M_{\odot}$), beyond which nuclear burning becomes predominant.

showing the relative populations in terms of L/M , which we have argued is at least qualitatively related to the successive stages. Note that this figure looks quite similar to Figure 16, there being a nonlinear mapping of L/M into T .

Figure 19 shows that there are many sources in stage E ($L/M < 1 L_{\odot}/M_{\odot}$), even though it is clear that there are selection effects (basically the combination of low flux density and cirrus noise) beginning to limit their detectability. Most of the sources are in the accretion-dominated stage A (L/M up to about 30 or $T = 30$ K). The relatively fewer hotter sources, where nuclear burning is taking over, presumably reflects the shorter lifetime of this stage, which could be characterized by more rapid final collapse and then envelope dispersal.

5. EVOLUTIONARY STAGES

Although our BLAST survey is “blind and unbiased,” in surveying the entire region rather than selecting sub-regions with, say, high extinction (Schneider et al. 2006; Motte et al. 2007), it is not unbiased in another sense. This region is obviously well known for its GMC and having formed the Cyg OB2 association, which has dramatically influenced the surrounding molecular material (Section 5.1). In such a region, one expects there to be both triggered and/or sequential star formation, supplementing spontaneous star formation. The conditions could be quite different now than what preceded the formation of Cyg OB2. We find no evidence for the precursor of another such massive compact association. Nevertheless, within this reservoir several smaller, but still notable, embedded clusters have been identified (Section 3.1). The OB stars in the more evolved ones have produced extended H II regions like DR17 and DR22 (Downes & Rinehart 1966).

As discussed in Section 3.5, in their $^{13}\text{CO } J = 2 \rightarrow 1$ data cubes, Schneider et al. (2006) have identified many clumps (detailed in their Appendix C). Where the coverage overlaps, each of the BLAST compact sources can be linked through the morphology to one of these clumps (see examples in Section 3.6). In Figure 20, we compare the sum of the masses of the BLAST sources (Section 4.4) within each clump to the tabulated CO-estimated clump mass. These are fairly well

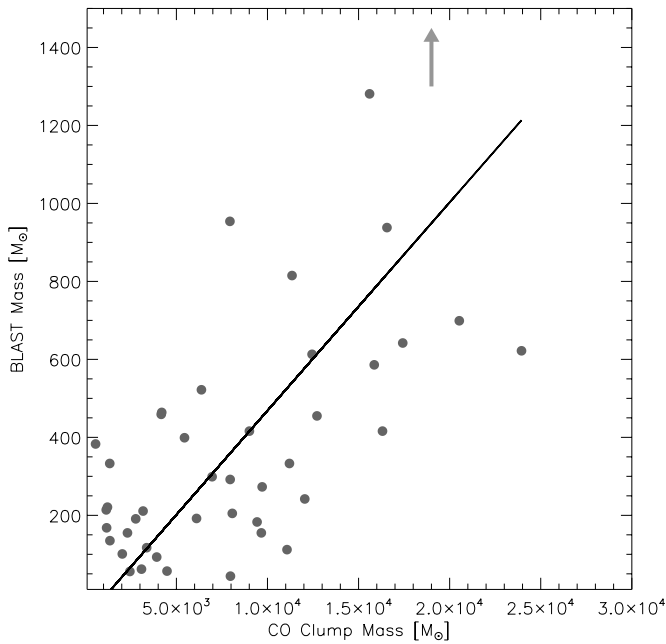


Figure 20. Sum of the masses of the BLAST sources within CO clumps of Schneider et al. (2006) vs. the CO-estimated clump mass. Linear correlation has a slope of 0.05. An outlier at $3000 M_{\odot}$ along the x direction, pointed to by the arrow, is not included in the fit.

correlated, and we typically find that only a few percent of the material over these extended regions are in the form of compact sources, in some way related to the (potential) star formation efficiency. This plus the timescales for clump evolution indicate that there is still an interesting future for star formation in this GMC.

From this perspective on the complex range of star formation going on in Cyg X, our goal is to work toward submillimeter evidence for the earliest stages of massive star formation. The somewhat later stages have been detected by a variety of earlier observations, and BLAST sees these too. The many clusters in Cyg X are agents producing complex morphologies in the medium, through expanding H II regions and strong UV radiation fields, and they might play a pivotal role in inducing further star formation in the molecular clouds. We work in reverse chronological order, finding what the outcome of a particular stage looks like in multi-wavelength data, and then asking what this tells us to look for in the stages that came before.

5.1. The Influence of the Massive Cluster Cyg OB2

Comparing the estimated mass of Cyg OB2 (Section 3.1), $(4\text{--}10) \times 10^4 M_{\odot}$ (Knödlseder 2000) to the remaining molecular reserve in Cyg X, $4 \times 10^6 M_{\odot}$ (Section 3.5; Schneider et al. 2006), indicates that formation of this OB2 association was the major event for this GMC, perhaps not to be repeated. Both of the central clusters, BBD1 and BBD2, are more massive than the Trapezium. Again, will there be more elsewhere in Cyg X? There is no BLAST clump that could be a precursor to such a prominent cluster and even adding the mass of an embedding CO clump (the most massive of which is $2 \times 10^4 M_{\odot}$) would fall short. Nevertheless, in unevolved GMCs, massive and compact precursors to such clusters might be detectable in the Planck Cold Core survey (Section 2.2; Juvela et al. 2010). It will of course depend on how long lived the precursor stage is.

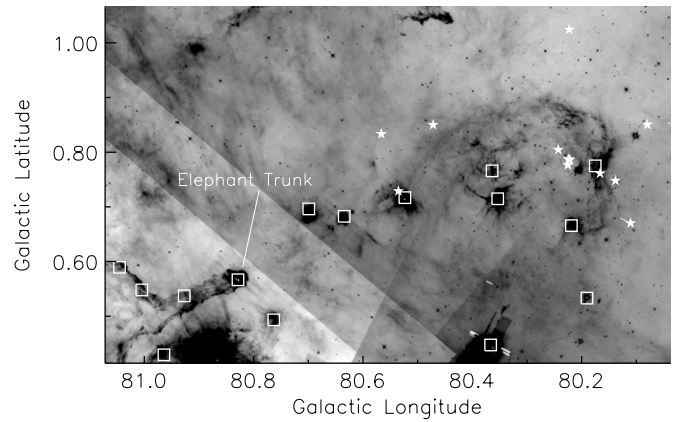


Figure 21. IRAC band 4 image showing a prominent pillar or “elephant trunk” structure pointing to Cyg OB2. Squares are BLAST sources and stars show the position of the OB stars.

Massive young stars, through ionization and radiation pressure, dramatically influence their environment. Cyg OB2 has an age of about 2.5×10^6 yr (Negueruela et al. 2008), and in that time has created in the ISM a lower density region of radius 1° (30 pc), ionized in the interior (see Figure 2) and surrounded by distinctive molecular cloud complexes. The connectivity of these clouds in the CO data cube and the signs of interaction through UV radiation (*MSX* Band A data) led Schneider et al. (2006) to conclude that they were all located at the same distance. While obviously not yet disrupted, the clouds have been reorganized and so Cyg OB2 might have induced some of the further star formation that is ongoing.

Above Cyg OB2 in Figure 2 is a relative void (nevertheless, it is projected on an emission and extinction plateau), with no high-contrast structures of significant column density in any tracer (molecules, dust, and ionized gas). The right-hand edge is defined by CXR9, whereas the left, though well-defined and containing some BLAST emission too, is unnamed. This void could be a “chimney” blown out by Cyg OB2, channeling high pressure gas out of the Galactic disk.

5.1.1. Pillars

Radiative forces sculpt pillars, where there are pre-existing dense molecular structures. The range of radiative influence of Cyg OB2 extends to a radius of at least 2° (60 pc), as illustrated by the prominent pillars near G79.4–1.1 and G81.4+2.2 in the *Spitzer* IRAC and $24 \mu\text{m}$ MIPS images. Figure 21 shows an example of a long pillar or elephant trunk pointing toward the Cyg OB2 core. At the end of the trunk is a luminous BLAST clump C85. In CO emission, it is called DR20NW by Schneider et al. (2006), with CO velocity $+12 \text{ km s}^{-1}$ (see also Figure 10). The clump is the obstruction defining the trunk structure. Star formation is occurring in this clump, suggestive of triggering by Cyg OB2. This geometry is seen elsewhere; for example, C75 on the left edge of the chimney is also at the head of a pillar facing Cyg OB2 (see also the cometary tails below).

Such a peninsular structure is continually eroded, which would produce eventually an isolated clump with a cometary tail, but this particular trunk appears to be attached to the molecular cloud, curving round and broadening out to include C91, C98, and C100 along the interface. These structures also evolve due to instabilities at the interface of the H II region and the neutral molecular cloud, and evidently ongoing star formation is commonly induced.

Note that DR20 (C88, C87, and C90) is at a projected distance of $6'$ from this trunk, and yet does not display the same hallmark interactions. However, this complex is at a very different velocity -3 km s^{-1} , more closely associated with DR21. Schneider et al. (2006) note that clump DR20W, at the same velocity, does have an elongated shape pointing to Cyg OB2 (see Figure 10). BLAST C80 is at the brighter head of its CO emission and C83 in the dimmer tail. Inspection of the *Spitzer* images shows signs of interaction with nearby stars in Cyg OB2, but at a different position angle than the CO clump which is oriented more toward the core.

Schneider et al. (2006) also identify other molecular pillars in the CO channel maps, the most prominent of which is the long “DR17 pillar” at a velocity about -13 km s^{-1} (Figure 9). From its direction of elongation, it appears to be influenced by the cluster LK12 in DR17, but there is not perfect alignment (possibly there is some influence of LK14 to the north). This cluster does produce a bright mid-infrared interface at BLAST C115, near the end of the pillar. The molecular pillar stretches from C115 through C114, C112, C113, and C108 to C109 and possibly C106 (Figure 9). The CO channel maps hint at a connection between this DR17 pillar and the above-mentioned elephant trunk, but this pillar does not appear to be influenced by Cyg OB2.

5.1.2. Cometary Tails

Further striking evidence for interaction is provided by cometary tails in more detached structures, pointing away from the core of Cyg OB2. These too are seen most clearly in *Spitzer* IRAC and $24 \mu\text{m}$ MIPS images.

DR18 is a large-scale prototype, with a ionized edge facing the Cyg OB2 core, the BLAST clump C73 in the neutral region next to this, and an extended tail seen in both CO and dust emission (mid-infrared to submillimeter). It is actually more complicated than this in detail, because a loose aggregate of early B stars has formed (triggered?) near the leading edge adding additional ionizing power and sculpting of the immediate PDR environment (Comerón & Torra 1999).

Another interesting example in the opposite direction is the cluster ECX6-21 (DB12) containing BLAST C55 in the head. C55 corresponds to OB2 globule 2 of Schneider et al. (2006) with CO velocity -4.5 km s^{-1} . About $5'$ “downstream” is a miniature version containing C53. These are located on the inner edge of the ionized ridge CXR9.

Further afield from Cyg OB2 is DR15, with a cluster and two BLAST clumps, C32 and C28. Here the putative tail (see Figure 7) appears to be part of an extended structure prominent in presumed PAH emission, which bends significantly toward lower latitude at a distance of $17'$, near C12. There are several other BLAST clumps along this structure, C21 before the bend, and C11, C9, C4, and C3 beyond.

Figure 22 shows a field quite close by, spanning the ionized ridge CXR11. There are two BLAST clumps C38 (on the left) and C17 with material ablated from the clump clearly being blown away. However, in the BLAST image these cometary tails are not detected because of low column density. C38 is massive enough to have a detectable ionized edge. The C17 tail extends to an angular distance of $6'$ or about 3 pc in spatial scale. If, for illustration, the clump lifetime were 10^5 yr the required material speed would be 30 km s^{-1} to reach such an extent.

There are many other sources like this with obvious interactions. Their positions in the $L-M$ diagram are highlighted in Figure 17. For these exposed sources, it is clear that a sizable

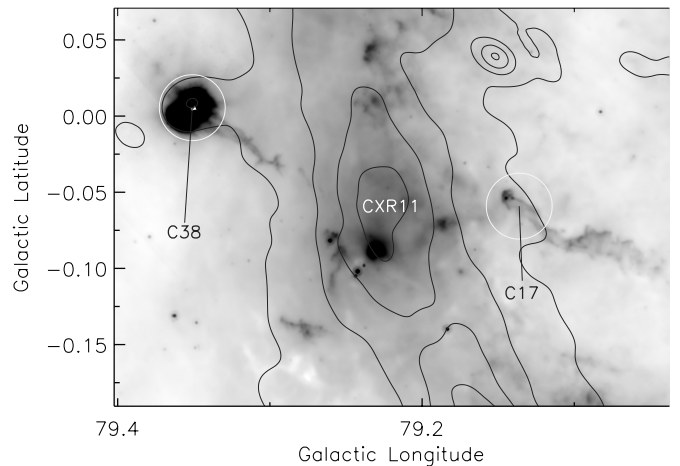


Figure 22. $24 \mu\text{m}$ MIPS image showing two BLAST sources, C38 and C17, with cometary tails. The spatial extents of the tails are roughly 1.5 and 3 pc, respectively. Contours of 21 cm radio emission from CGPS show ridge CXR11.

amount of mass is lost due to this erosion, and so the more evolved sources occupy a region toward the lower end of the mass axis in the $L-M$ plot.

The ridge of submillimeter emission containing sources C59, C61, and C60 provides an interesting counter-example. The superimposed CO ridge is called “OB2 globule 1” by Schneider et al. (2006), who suggest an interaction due to its compactness and proximity to the core of Cyg OB2, in projection about $15'$ away. However, inspection of the detailed *Spitzer* images that are now available reveals no signs of interaction. Furthermore, the displaced ionized ridge parallel to the dust emission is on the side away from Cyg OB2 (see Figure 6). Together with the peculiar velocity, the evidence is that this object is more distant, beyond the influence of Cyg OB2.

5.2. Clusters and Extended H II Regions

Interactions of clusters with the ISM produce large-scale complex structures and directly affect the next generation star formation efficiency in the region. The Cyg X region hosts numerous young open clusters (Section 3.1). In the BLAST region, there are five which have well-resolved H II regions with a fairly classical geometry. Expansion of the ionized gas, stellar winds, and radiation pressure have evacuated the core of the parent molecular cloud and produced a dense shell which appears in an arc-shaped geometry surrounding the cavity and cluster. Partial shells are suggestive of a blowout or blister geometry. The 21 cm radio emission traces the I-front, and slightly outside of this is the FIR and submillimeter continuum, where dust in the shell absorbs the FUV radiation emitted by the star cluster.

To illustrate this, Figure 23 shows an IRAC band 4 image highlighting the most massive of these clusters, LK11, with about 80 OB stars powering the DR22 region. Note that the PAH emission in this image is from the PDR, outside the I-front, whereas the $24 \mu\text{m}$ emission in Figure 12 shows greater correlation with the ionized gas. The BLAST sources occur along CO ridges to the north and southeast, the latter clearly arc-shaped (making this the “smiley nebula”). The most luminous source C92, coincident with a compact H II region, must be internally powered (see below). LK11 is shaping this clump and both the geometry and proximity suggest that star formation has been triggered there.

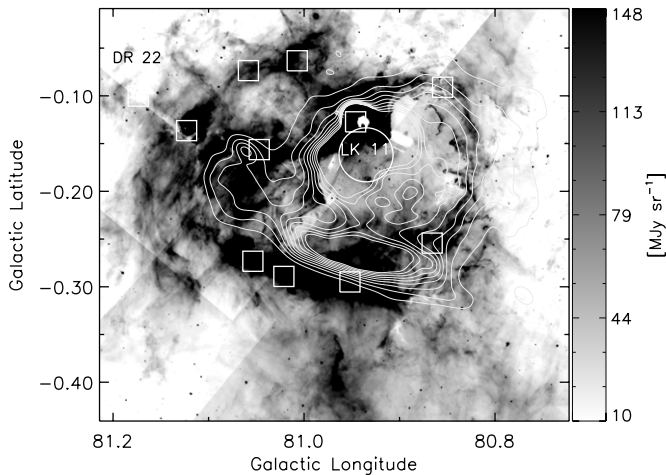


Figure 23. IRAC band 4 ($8.6 \mu\text{m}$) image of DR22. The circle marks the position and size (R_{50}) of the LK11 OB star cluster (Le Duigou & Knödseder 2002). Overlaid contours are 21 cm radio continuum emission from the CGPS. Squares indicate the BLAST sources, embedded in arcs of submillimeter emission outside the I-front (Figure 12).

Similar geometrical statements can be made about LK09 and C30 (and C27, C33) in DR7 (Figure 6), LK12 and C115 in DR17 (Figure 9), LK13 and C127 in G81.445+0.485 (the Diamond; Figure 11), and DB22 and C182 (and C177, C178) in ECX6-33.

Although these H II regions have evolved, the exciting clusters are still quite young; their stellar density is typically five times higher than for evolved open clusters (Le Duigou & Knödseder 2002). Thus, their radii R_{50} (half population radius), about $1'$ (0.5 pc), are perhaps indicative of the size of the precursor molecular clump. The stellar masses are estimated by Le Duigou & Knödseder (2002) to be $300\text{--}2000 M_{\odot}$ (a few times more for DR22) and so the precursor clump would be more massive still. BLAST clumps are of this angular size, but not nearly as massive, not even up to these stellar masses let alone allowing for inefficiency of star formation. We conclude that there are presently no BLAST clumps capable of forming such massive clusters. The embedding CO clumps are perhaps massive enough, but would have to condense considerably to form a concentrated cluster. The lifetime of these condensations could be quite short, lowering the likelihood of detecting this stage in a single GMC.

5.3. Triggered Star Formation

Spatially, a massive star cluster can promote further star formation in nearby molecular material by driving winds and shocks, which both sweep up material and overrun and compress pre-existing condensations. Subsequent gravitational instability and/or radiatively driven implosion of the overrun condensations collectively lead to what is known as “triggered” star formation (Elmegreen 1998; Zinnecker & Yorke 2007; Koenig et al. 2008). Thus, a sequence of generations of star formation can occur with spatial ordering (recognized as “sequential” star formation). For example, Koenig et al. (2008) studied these phenomena in W5 with *Spitzer*.

As discussed, in the vicinity of the OB star clusters in Cyg X there is evidence of further star formation. The most persuasive, if circumstantial, evidence for triggering is in the DR22, DR8, DR17, and DR15 molecular clouds.

5.4. Compact H II Regions

Earlier in their development, when massive protostars first become hot enough to emit ionizing UV photons, they initially ionize only a dense core, producing a hypercompact H II region, potentially optically thick at lower radio frequencies. Subsequent expansion of the ionized gas leads successively to ultracompact, compact, and then evolved H II regions (Churchwell 2002). The initial stage, which occurs when accretion is still strong, is accompanied by energetic bipolar outflows.

Circumstellar dust reprocesses the absorbed radiation from the protostar, re-radiating the energy at infrared wavelengths. Thus, in the Galactic plane, embedded H II regions are the most luminous objects observed in the mid- and far-infrared, first by *IRAS* and then *MSX*.

Hot cores, dense molecular clouds with temperature ≥ 100 K as classified by Kurtz et al. (2000), are often thought to be precursors of UC H II regions. In our survey, we do not detect any source warmer than ~ 40 K. Nevertheless, some of the brightest sources detected by BLAST in Cyg X are found among well-known H II regions, with previous studies revealing them to be compact or ultracompact; they are all detectable in 21 cm radio continuum emission in the CGPS. Five of these studied by Motte et al. (2007) are tabulated in Table 5 and discussed in the following subsection. Motte et al. (2007) obtained masses of these sources assuming a dust temperature of 40 K. We are actually able to measure the temperature, finding 30–40 K. Still, it should be remembered that BLAST measures dust emission including the outer envelope of these sources, which is cooler than dust near the core; with higher angular resolution MAMBO should sample slightly warmer dust on average.

These five sources are marked in Figure 24 with special symbols. They are clearly internally powered, beyond the transition to predominant nuclear burning. For reference, a $20 M_{\odot}$ ZAMS of spectral type O9V has $L_{\text{bol}} = 10^5 L_{\odot}$ (Schaerer & de Koter 1997). Even the most luminous of these embedded stars at the distance of Cyg OB2 is not that luminous. Given the mass of these clumps, $> 100 M_{\odot}$, they also seem likely to host more than a single star.

The precursors to these sources should be cooler, at similar mass. In the range of a few $100 M_{\odot}$, there are many such BLAST sources in Figure 24, the earlier stages to be discussed below. However, there do not seem to be the cooler equivalents of most massive sources (W75N, DR21, and DR21 OH), suggesting that the precursor stage to the most massive (dense) clumps is relatively short-lived or that when the cooler clump is too extended to have been classified as a BLAST source (Section 6.4).

Also, recorded in Table 5 are another 11 instances (including two distant ones) of BLAST sources with apparently associated compact 21 cm radio emission, not targeted by Motte et al. (2007). These are slightly cooler, with median temperature 27 K. These are marked in Figures 18 and 24 with gray filled circles.

A histogram of the bolometric luminosities of all of these sources, including the luminosity corrections for the two distant ones, is given in Figure 25. The luminosities of the five marked sources are at the high end, whereas most of the others have much lower luminosities. The luminosities can be used to calculate the corresponding photoionizing flux Q_0 and check for consistent radio emission (assuming no optical depth; see Section 3.2). The lowest luminosity sources in Figure 25 would not account for the associated H II emission. Inspection of the IRAC image reveals all but C76 to have cometary structure (those of higher mass and luminosity were already mentioned

Table 5
Compact H II Regions and Protostars

BLAST ID	T (K)	M ($100 M_{\odot}$)	L ($100 L_{\odot}$)	Source Name	MAMBO 1.2 mm	Figure ^a No
C1	40	1.9	489.0	S26, AFGL2591	UCH II	7
C7	26	2.6	50.2	S30, IRAS 20293+3952	MIRQP	7
C14	30	3.8	4.5	IRAS 20255+4032	...	6
C30 ^b	38	17.6	1640.0	IRAS 20264+4042
C32	46	1.1	330.7	S41, IRAS 20306+4005	HLIRPC	7
C36	26	2.6	30.6	S37, IRAS 20305+4010	MIRQP	7
C38	38	0.4	48.7	IRAS 20319+3958
C49	27	0.1	2.8
C55	30	1.6	52.9	IRAS 20286+4105
C58	28	0.2	4.1	IRAS 20315+4046
C64	31	0.1	6.0	IRAS 20328+4042
C71 ^b	31	22.5	782.5	IRAS 20320+4115
C73	33	1.6	87.6	IRAS 20333+4102
C76	28	0.8	21.8	IRAS 20327+4120
C80	30	1.5	48.9	IRAS 20332+4124
C85	30	1.2	51.8	N6, IRAS 20343+4129	HLIRPC	10
C87	27	1.8	33.6	N14, IRAS 20352+4124	HLIRPC	10
C88	33	1.9	106.3	N10, IRAS 20350+4126	UCH II	10
C92	39	1.9	323.2	N58, IRAS 20375+4109	CH II	12
C104	28	1.8	44.7	N62	IRQP	12
C107	22	1.3	7.3	N63	MIRP	12
C115	26	2.2	31.4	N3	MIRQP	9
C119	22	3.0	15.2	N12	MIRQP	9
C141	22	1.7	8.9	N65	MIRQP	12
C145	22	1.1	10.7	N68	MIRQP	12
C155	36	8.8	776.6	N46, DR21	UCH II	11
C157	27	18.8	319.3	N44, DR21(OH)	MIRQP	11
C167	20	3.2	10.6	N24	IRQP	11
C169	36	7.6	664.1	N30, W75N	HCH II	11

Notes.^a Figure number of the images containing individual sources.^b M and L corrected for distance (see Section 4.2).

above: C55, C73, C80; all but C14 appear to be influenced by Cyg OB2) and our interpretation is that the radio emission comes from external ionization. C76 lies in close projection to the O7 V star MT771.

5.4.1. Specific Embedded H II Regions in Cyg X

Here we make brief comments on the five marked sources from Motte et al. (2007) in Table 5, plus three others that appear to be in the same advanced stage of evolution.

C1, AFGL 2591. C1 coincides with AFGL 2591, an UC H II region that is among the most luminous sources in Cyg X. Motte et al. (2007) identify a core S26 within a clump S5. We find dust temperature 40 K, bolometric luminosity $2.7 \times 10^4 L_{\odot}$, and mass $190 M_{\odot}$. Campbell (1984) discovered that AFGL 2591 is comprised of a young stellar group and deduced that the H II region is being generated by B0 stars. This region also has powerful outflows (Bally & Lada 1983; Poetzels et al. 1992). Schneider et al. (2006) argue that the cometary shape is due to the influence of Cyg OB2.

C88, DR20. Compared to C1, C88 is slightly cooler (32 K), less luminous ($8.6 \times 10^3 L_{\odot}$), but equally massive ($190 M_{\odot}$). It corresponds to clump N4 (core N10) of Motte et al. (2007). The embedding region (see Figure 10) is bright in 21 cm radio continuum, mid-infrared, and PAH emission. C88 and C87 are two bright sources along a ridge containing C90. C88 is closest to the CGPS radio peak, but offset to lower longitude, whereas the UC H II region G80.86+0.4 observed by Kurtz et al. (1994)

is centered on C88. C88 also coincides with IRAS 20350+4126. Odenwald et al. (1990) suggest excitation by an O5-6 ZAMS star, but this seems too early.

The source C87 (clump N6, core N14) is relatively cold, 27 K, with no free-free emission. Its position on the L - M plot suggests most of the luminosity is generated from accretion (see below).

C92, DR22. C92, also known as IRAS 20375+4109, is a compact H II region in DR22 with a massive dense core, N58 (Motte et al. 2007). We find dust temperature 39 K, bolometric luminosity $2.4 \times 10^4 L_{\odot}$, and mass $220 M_{\odot}$. Odenwald et al. (1986) studied this region at both radio and far-infrared wavelengths and, assuming it to be 45 K and 3 kpc distant, they deduced that a single O6 ZAMS star was accounting for a luminosity of $3 \times 10^5 L_{\odot}$. This would be relaxed for the closer distance adopted here, and as mentioned above there is likely more than a single star in a BLAST clump (Section 5.4).

C155, DR21. C155 is the most luminous source in the BLAST survey region with dust temperature 36 K, luminosity $7.0 \times 10^4 L_{\odot}$, and mass $880 M_{\odot}$. DR21 has a dense core N46 with signatures of outflows (Motte et al. 2007), suggestive of an early stage OB cluster. Supportive of multiplicity, Motte et al. (2007) detected another two cores within a 1' radius in their clump N15; our mass agrees with the total mass of the three cores. This clump in the DR21 cloud complex (see Figure 11) harbors one of the most studied UC H II regions: microwave (Downes & Rinehart 1966), radio (Kurtz et al. 1994), near-infrared (Davis et al. 2007), and ^{13}CO (Schneider et al. 2006). Studying

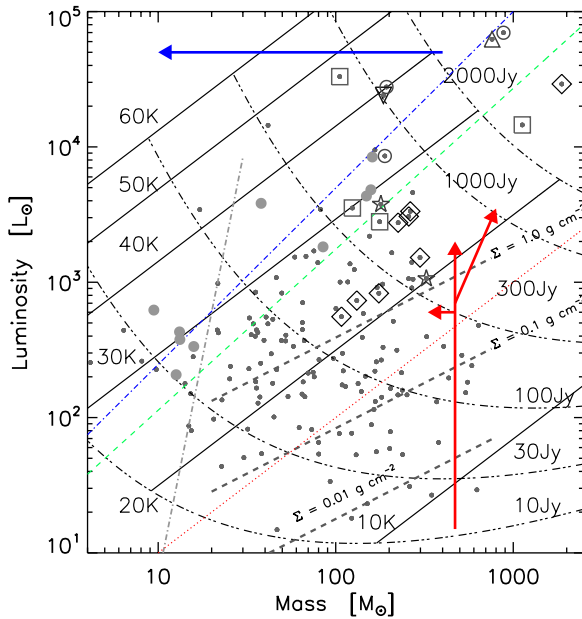


Figure 24. Same as Figure 17, but highlighting physical properties deduced from ancillary data. Many of the most luminous sources are ionizing and have associated radio continuum emission. Close to the nuclear burning locus, these contain deeply embedded massive stars (Motte et al. 2007): Δ HCH II; \circ UCH II; ∇ CH II. Gray filled circles are other BLAST sources with compact 21 cm continuum emission, outside the survey area of MAMBO. Protostars in stage A are at somewhat smaller L/M than the compact H II regions, near the accretion locus. These are classified by Motte et al. (2007) as \square HLRPC; \diamond MIRQP; and \star IRQP. At the lowest L/M , clumps are externally heated (stage E), while at intermediate values the clumps are probably powered by low-mass protostars; the thick dashed lines are the model predictions of Krumholz & McKee (2008; also see our Equation (7) in Section 6.3) for surface densities $\Sigma = 1.0, 0.1,$ and 0.01 g cm^{-2} . The vertical arrow signifies the result of evolution in L as star formation progresses in a clump. This might be interpreted as the result of the evolution of a single massive protostar (Molinari et al. 2008). However, the initial rise seems more likely to be the result of power from low-mass YSOs (Section 6.2). According to the model of Krumholz & McKee (2008), unless Σ exceeds a critical value near 1.0 g cm^{-2} , a massive star will not form and so the rise in L will be arrested (Section 6.4); this possibility is indicated schematically by the short horizontal arrow. Finally, the arrow segment pointing to the upper right represents qualitatively the evolution in the simulations by Smith et al. (2009) and Wang et al. (2010), where mass is fed into gravitational potential minima from the larger scale structure.

(A color version of this figure is available in the online journal.)

hydrogen recombination and the ammonium line, Cyganowski et al. (2003) found cometary morphology associated with the H II region. It is also identified as MSX6C G81.6802+0.5405, an *MSX* source, specifically bright at $8 \mu\text{m}$, and has saturated *Spitzer* sources. There is an embedded near-infrared cluster, W75S (Bica et al. 2003). The position of C155 in the $L-M$ diagram confirms that star formation is well established.

C169, W75N. The W75N cloud complex shown in Figure 11 is a well-known massive star-forming region. After first being detected at low resolution in the radio by Westerhout (1958) and Downes & Rinehart (1966), this complex was studied to decipher numerous “protostellar physical conditions.” A wide variety of sources were found embedded in this cloud, e.g., a group of infrared sources (Moore et al. 1991; Persi et al. 2006; Davis et al. 2007), UC H II regions, and H₂O and OH masers (Hunter et al. 1994). Haschick et al. (1981) identified three ionized regions within W75N, namely W75N (A), W75N (B), and W75N (C). Subsequent higher resolution surveys by Hunter et al. (1994) resolved W75N (B) into another three subregions. Motte et al. (2007) found three sources associated with the

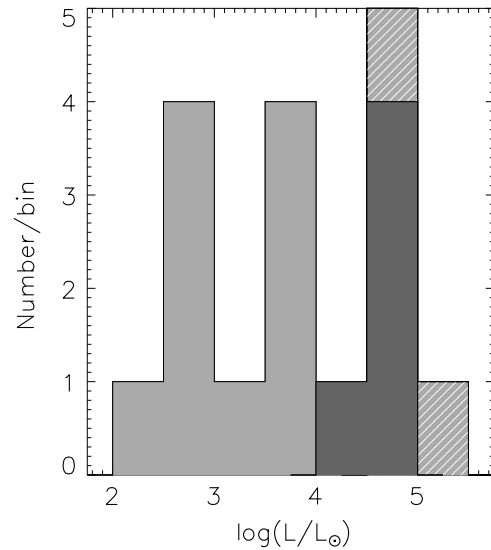


Figure 25. Histogram of L_{bol} for BLAST sources with compact H II emission. Two of the most luminous (stripes) are at a larger distance than Cyg OB2. The five noted by Motte et al. (2007) are shaded black. Other lower luminosity sources appear to have external ionization (Section 5.4).

W75N cloud (clump N13), of which W75N (B) is the most massive object, with a dense core N30. They classified this source as an HC H II region. BLAST with $1'$ resolution observes only one source. The derived properties are dust temperature 36 K , luminosity $6.2 \times 10^4 L_{\odot}$, and mass $760 M_{\odot}$, very close to C155. The radio emission at 21 cm is however much less, probably because of self-absorption (there is appreciable self-absorption in the spectrum of DR21 too, Wendker et al. 1991), but possibly because of a different IMF in the embedded clusters.

There is another embedded cluster DB20 a few arc minutes to the north, coincident with clump N14 of Motte et al. (2007) and its core N28.

C32, DR15 cloud. The DR15 complex was previously observed at radio wavelengths by Colley (1980) and Odenwald et al. (1990), who predicted that it hosts OB stars. Both free-free emission and PAH emission observed by *MSX* suggest ongoing star formation. The morphology of this cloud is complex, with extended emission on a range of scales. We could resolve two sources, C32 and C28. The cluster LK08 and radio peak are located between these (Figure 7). Motte et al. (2007) detected three embedded sources, of which two, MSX 79.2963+0.2835 and MSX 79.3070+0.2768, are within C32. The *Spitzer* sources are saturated. We find dust temperature 46 K , luminosity $3.3 \times 10^4 L_{\odot}$, and mass $110 M_{\odot}$. Motte et al. (2007) designated core S41 in clump S11 (corresponding to C32) as a high-luminosity infrared protostellar core (HLRPC). Our analysis based on the location of C32 in the $L-M$ plot suggests a slightly later stage like the other embedded H II regions being discussed. However, it is a complex region that will benefit from better resolution as provided by *Herschel*. It is possible that the temperature of the dust is influenced by the nearby cluster LK08, and fitting a single-temperature SED for this source would probably underestimate the clump mass.

C73, DR18. DR18 was studied extensively in the near-infrared by Comerón & Torra (1999) who found a stellar group. Most of the illumination is due to a single B0.5 V star which can be observed in the visible as well as the infrared. The CGPS radio peak is at the head of the larger cometary structure (see above) and probably is affected by external ionization. Consistent with

the cometary structure, C73 lies between the ionized gas and the CO clump. C73 has properties very similar to C88 in DR20. This interesting region is outside the coverage of Motte et al. (2007).

C30, DR7. Figure 6 shows LK09 located at the center of the DR7 H II region arc. The CGPS H II emission peak and ECX6-18 lie between BLAST sources C30 and C27; the former is much more massive. This region is not covered by Motte et al. (2007). The derived parameters for C30 are very close to those for C32, assuming the same distance. However, as remarked in Section 3.6, its velocity places it well behind the Cyg OB2 complex, at 3.6–7.5 kpc (we adopted 6.8 kpc in Section 4.2). Thus, this source should be about 16 times more massive and luminous, as listed in Table 5, ranking it with the most powerful sources in this survey.

5.5. Stage A: Accretion Power, Protostars, and MYSOs

As mentioned, BLAST cannot hope to see single stars, though the clump might be dominated by the most massive member of the group. During the next earlier stage, precursor to the embedded H II regions, matter collapses under gravity at multiple sites inside the clump, which are newly born stellar cores (Mac Low & Klessen 2004). The luminosity of the clump originates from the cumulative energy of accretion onto cores. During this accretion stage, protostars build up luminosity with little loss of envelope mass. In our L – M diagram (Figure 24), the evolution should be vertical, crossing the region between the dotted red line ($L/M = 1 L_{\odot}/M_{\odot}$) and the dashed green line. The former is coincidentally close to diffuse cirrus emission in equilibrium with interstellar radiation field at 17.5 K (Boulanger et al. 1996). The latter, taken from Figure 9 of Molinari et al. (2008), is a best fit to Class 0 sources. Sources plotting in this region would have cooler dust temperatures in the range 18–25 K, and $L/M \geq 1 L_{\odot}/M_{\odot}$ would clearly indicate internally powered sources.

Motte et al. (2007) have identified several massive infrared quiet protostellar cores (MIRQP), sources with mass greater than $40 M_{\odot}$ with at least some evidence of stellar activity and yet weak emission in the mid-infrared. All of the massive infrared-quiet cores are associated with high-velocity SiO emission, providing convincing evidence of powerful outflows and ongoing accretion. The SiO emission of MIRQPs is typically stronger than from HLRPCs, indicating that the former are in a more vigorous accretion phase.

Of the 17 MIRQP, eight are within our BLAST survey area and are readily detected and characterized (Table 5). In the L – M evolutionary diagram, they occupy the predicted region (see diamonds in Figure 24). Judging from Figure 24, there are many other BLAST sources with similar properties. The sensitive *Spitzer* images reveal the sub-structure, with many accreting cores over a range of fluxes (see also Section 6.2).

C157, DR 21(OH). The most luminous MIRQP is in DR21(OH), which is lacking in 21 cm radio free–free emission. However, high-sensitivity subarcsecond observations with the Very Large Array at centimeter wavelengths by Araya et al. (2009) reveal a cluster of radio sources; the strongest emission is toward the molecular core MM1, but is perhaps from shock-ionized gas in a jet rather than from a nascent compact H II region. C157 is also cooler than the strongly ionizing sources discussed above, as one might expect. It has a dense core N14 along with five neighboring fragments (Motte et al. 2007) in clump N14. Harvey-Smith et al. (2008) have observed 6.7 GHz methanol emission in all five spots, but only two of

them (DR21(OH) and DR21(OH)N) exhibited strong peaks. Our limited resolution integrates the dust emission from all nearby fragments. Though Motte et al. (2007) have classified the core as MIRQP, we note that the significant bolometric luminosity of C157, $2.9 \times 10^4 L_{\odot}$, is probably indicative of the entire cluster, detected in the near-infrared as DB19.

The next most luminous MIRQPs are in C7 and C115. C7 is an isolated source, whereas C115 is at the tip of the DR17 molecular pillar. Similarly, C119 is at the tip of an adjacent pillar (Figure 9). C36, among the coolest, is just north of DR15, at the most evolved end of the IRDC G79.34+0.33 discussed below (Section 5.6.2). There is a variety of indications of star formation (Redman et al. 2003), and *Spitzer* images indicate a rich stellar group.

There are two sources classified as infrared quiet protostar (IRQP; not so massive as MIRQP) by Motte et al. (2007) which appear to BLAST to be as luminous as the MIRQP-containing sources. The more luminous is C104 (N62 in clump N20 to the northeast of DR22) in the molecular filament (velocity -5 km s^{-1}) extending from DR22 through MIRQP C107 to MIRQPs C141, C145 and cluster LK15 in DR23 (see Figure 12). The most prominent molecular clump along this filament contains C138 (N69, in clump N23); it defines the boundary of brightest ionized part of DR23, powered by cluster DB17 to the east (Figure 12). The other is C167 (N24 in clump N10 to the northwest of W75N). At CO velocity -3 km s^{-1} , this is in the DR21 cloud complex (Figure 11). The *Spitzer* images indicate widespread embedded star formation in the C167 cloud and adjacent BLAST sources.

The two HLRPCs (other than C32 discussed above) plot toward the high-luminosity (high temperature) side of this region in the L – M plane. These correspond to the BLAST sources C85 and C87. C85 contains source N6 in clump N3 of Motte et al. (2007). It coincides with DR20NW (Schneider et al. 2006) at the head of the above-mentioned elephant trunk. There is an ionized rim on the face toward Cyg OB2, but apparently little internal ionization. Its position on the L – M plot suggests that most of the luminosity is generated from accretion. Compared to C88 also in the DR20 molecular cloud, C87 (clump N6 and core N14) is relatively cold, 27 K, with no free–free emission.

5.6. Stage E: Externally heated Cold Early Stage

Prior to the stage of active accretion, there must pre-exist a cold molecular clump with only external heating. A low temperature and corresponding low luminosity-to-mass ratio ($L/M \leq 1 L_{\odot}/M_{\odot}$) would be diagnostic of this stage. As a forerunner of SPIRE on *Herschel*, BLAST was designed to search for the submillimeter emission from such objects in the earliest stages of pre-stellar evolution, and according to Figure 17 has been quite successful, with 28 sources down to the approximate $250 \mu\text{m}$ completeness line of about 30 Jy. These compact sources are sufficiently cold and massive to be above the nominal Bonnor-Ebert critical mass. The higher mass objects can be considered as potential precursors of the MIRQP accretion-powered stage.

5.6.1. Cold Clouds with Nascent Star Formation

It is a general consensus that massive stars should begin to form within stellar nurseries deeply embedded in a dense envelope of dust and molecular gas. Because *Spitzer* is so sensitive and probes at wavelengths where the dust can be penetrated, evidence for such nascent star formation (not a lot

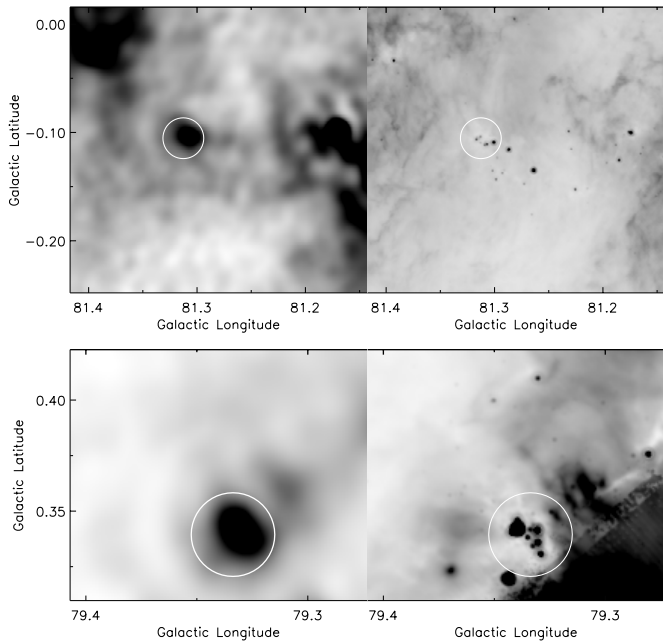


Figure 26. Left: cool BLAST sources at $250\ \mu\text{m}$. Right: corresponding $24\ \mu\text{m}$ MIPS images, showing evidence for nascent star formation. Top: C116. Bottom: C36 at the transition to MIRQP in IRDC G79.34+0.33. The radius of circles 1.3 .

of total power) is readily found. Figure 26 shows two examples. One is a cold BLAST source C116 (along the DR22–DR23 filament) corresponding to the Motte et al. (2007) core N70. We find dust temperature $17.1 \pm 0.8\ \text{K}$, bolometric luminosity $(2.2 \pm 0.4) \times 10^2 L_{\odot}$, and mass $(1.6 \pm 0.4) \times 10^2 M_{\odot}$. The other is C36, already containing a low-temperature MIRQP (Section 5.5), embedded in an IRDC (Section 5.6.2).

5.6.2. IRDCs

Given the appropriate geometry, highly dense, massive molecular clouds with significantly large extinction can be seen in silhouette as IRDCs. With the spatial resolution and sensitivity of *MSX*, many IRDCs have been found at Band A ($8.6\ \mu\text{m}$; Simon et al. 2006). The signature of an IRDC without a developed protostar is the lack of dust emission at mid-infrared *IRAS* wavelengths (Egan et al. 1998). However, this does not mean that there is no low-power nascent star formation, as illustrated below.

Because of the high column density, BLAST sees prominent IRDCs in emission. An example is the ridge (filament) shown in Figure 27 which contains the IRDCs G79.34+0.33 and G79.27+0.38 (Egan et al. 1998) with corresponding BLAST clumps C36 and C26, respectively. Although it was initially suspected that G79.34+0.33 was associated with the DR15 cloud, later Redman et al. (2003) found no such evidence. This filamentary ridge is associated with distinct ^{13}CO emission at velocities near $1\ \text{km s}^{-1}$ (Figure 7). G79.27+0.38 in the central part of the ridge was studied by Wu & Yang (2005).

Finer details can be found with the *Spitzer* images, both in extinction and in the presence of point sources. Both of these BLAST sources show evidence of nascent star formation (Figures 26 and 27). In fact, there are embedded mid-infrared objects right along the filament, even the upper part of the ridge where the less massive condensations are C25, C24, and C23.

Note that this ridge is seen in extinction against the shell of the LBV star G79.29+0.46 (Wendker et al. 1991), providing relative

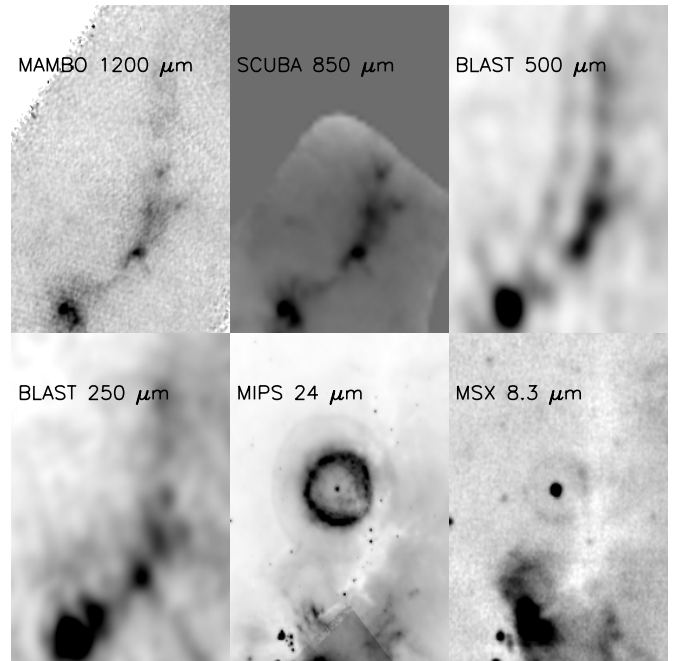


Figure 27. Multi-wavelength views of the IRDC ridge in Cyg X near $l = 79:23$ and $b = 0:45$. Each thumbnail has dimension $12' \times 16'$.

distance information which locates the star behind the Cyg X region. The shell, even the faint outer halo seen at $24\ \mu\text{m}$, shows no signs of interaction with Cyg OB2, indicating considerable separation. Kraemer et al. (2010b) have quantified this using the stellar parameters, obtaining a distance of 3 kpc.

Figure 28 shows an interesting long filament that shows up well in the $24\ \mu\text{m}$ image, in emission but changing to absorption in front of a bright band of cirrus. At *IRAC* $8\ \mu\text{m}$ it is only in emission, the bright cirrus band being absent. This structure is detected in BLAST emission as well as *CO*, extending the DR21 ridge to the south (Figure 11). The characteristic *CO* velocity, $-3\ \text{km s}^{-1}$, confirms that this is related to the DR21 molecular cloud. The extended mid-infrared source in the upper part is apparently warm and has no BLAST counterpart.

5.6.3. Starless Cold Clouds

Focusing on the earliest stage, are there any sources that are so far starless? The best candidates to search should be those in the region with $L/M < 1 L_{\odot}/M_{\odot}$. In terms of internally generated power, they all can be considered “starless.” But when examined in the *MIPS* $24\ \mu\text{m}$ image, most of these candidates do in fact have point sources, indicating nascent star formation though probably only low-mass young stellar objects (YSOs; Section 6.2).

However, we found one instance that is apparently starless at $24\ \mu\text{m}$, C81, an isolated feeble source with a weak *CO* signature at $+6\ \text{km s}^{-1}$. While there are some point sources at *IRAC* $8\ \mu\text{m}$, these do not have spectra rising to $24\ \mu\text{m}$ as might be expected of YSOs; also there is no special concentration to the BLAST source and so they are probably field star contamination. The *IRAC* image also shows several small IRDCs.

Two other possibilities are C103 and C121. (Curiously, C103 exhibits diffuse emission at $24\ \mu\text{m}$ including being crossed by a partial thin shell of radius 2.8 centered at G81.0425-0.1155.) C108, clump N2 of Motte et al. (2007) with no core, is crossed by IRDCs at 24 and $8\ \mu\text{m}$, and might be another good example of a starless clump.

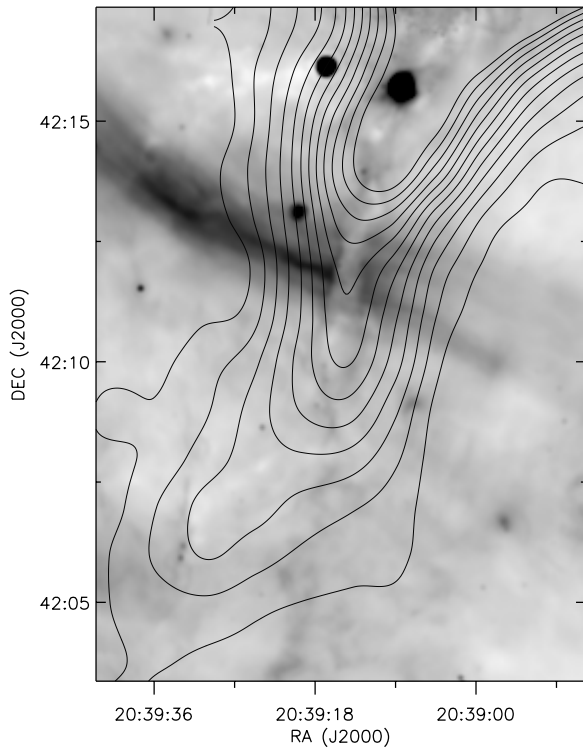


Figure 28. MIPS $24\ \mu\text{m}$ image showing dark lane extending from DR21 ridge. BLAST sees this lane in emission (Figure 11). The contours are ^{13}CO emission (Schneider et al. 2006) integrated over -7 to $1\ \text{km s}^{-1}$.

6. DISCUSSION

The L – M diagram (Figures 17 and 24) can be adopted as a diagnostic tool for describing the early evolutionary stages of massive star formation (Molinari et al. 2008). With our sample of compact sources now covering a broad range of luminosity and mass, particularly extending to low L/M , we are in a position to further assess its utility. We first review how independent empirical evidence for evolutionary stages relates to the characteristic position in the L – M diagram and then, to the extent possible, use theoretical models to provide insight into the evolution.

6.1. High L/M

In the Cyg X region, 16 BLAST sources have detectable compact 21 cm continuum emission. All have strong $100\ \mu\text{m}$ emission and so are not background radio galaxies. Our detections of these sources are represented by filled light-gray circles in Figure 24. Five of these were also noted and classified for H II region compactness by Motte et al. (2007) and are marked as triangles, circles, and inverted triangles. All of these clumps appear in the higher T ($>30\ \text{K}$) and L/M region, near the nuclear burning locus, above the stage A sources and the empirically obtained accretion line. An extensive discussion of individual embedded H II regions in Cyg X has been presented in Section 5.4. High-mass protostars inside these massive clumps account for the high ionization rate and luminosity. We do not have the angular resolution to distinguish multiplicity, but the clumps contain multiple sources when examined in the near- and mid-infrared (Section 6.2).

SiO ($2 \rightarrow 1$) emission is often used as a tracer of shocked gas, associated with outflows which are an intrinsic consequence of accretion process. After the onset of nuclear burning stage,

massive stars build up an intense radiation pressure which halts further accretion. In accordance with this expectation, the luminous sources DR21 and W75N have only low intensity SiO ($2 \rightarrow 1$) emission (Motte et al. 2007). In fact, all of their HLIRPCs correspond to BLAST sources with high L/M and also do not have a striking molecular emission accretion signature.

Slightly earlier in the evolution, clumps are already quite luminous, near the empirical accretion locus for massive stars; single-star cores within them would be classified as Class 0, at least for lower mass stars. On the basis of their position in this region in the L – M plot, we would expect these BLAST sources to show independent and direct evidence of (bipolar) outflow and indeed this is the case (Section 5.5). Motte et al. (2007) identified a class of massive IR-quiet protostellar cores (MIRQP) with strong SiO ($2 \rightarrow 1$) emission, indicative of ongoing active accretion. The eight BLAST sources corresponding to their MIRQP are marked by diamonds in Figure 24 and all of them lie in the stage A accretion-dominated region of the diagram.

6.2. Low L/M

In the Cyg X region, we have discovered a significant fraction of the clumps with low L/M devoid of massive protostellar cores. This low L/M regime is for us the most intriguing part of the L – M diagram, potentially containing the story of the earliest stages of massive star formation. Molinari et al. (2008) show vertical tracks corresponding to the evolution of a *single and massive* protostar, and this is suggested by the vertical arrow in our L – M diagram. However, this is probably a misleading interpretation for low L/M . Even though these clumps appear above the “ $L = M$ ” line, and are arguably self-luminous, there is no obvious signature of a high-mass star being formed. Given that massive protostars probably evolve rapidly through this region, it is statistically improbable to observe this stage.

The more likely alternative energy source is the collective power of many lower mass YSOs. In Section 5.6.1, we have already previewed some evidence for multiple YSOs in cold massive clumps. Since the BLAST observations were carried out, a census of YSOs has been obtained by Beerer et al. (2010) based on SEDs from *Spitzer* imaging of the northern part of the Cyg X region. Using their map of *Spitzer* YSO positions (their Figure 8), we find YSOs, often multiple YSOs, associated with most of our clumps. For the brighter sources, we probably underestimate the number of (crowded) YSOs when using their Figure 8 rather than a catalog. Figure 29 demonstrates that the observed L/M is correlated with the total number of YSOs per unit clump mass, as expected energetically. This also suggests considerable fragmentation into low-mass stars, an inevitable result of the initially low Jeans’ masses in the cold gas (Krumholz 2006).

There are (at least) two hypotheses for massive star formation, namely the competitive accretion model (Bonnell et al. 1998) where massive stars are formed due to dynamical coalescence of low-mass stars in a dense clustered medium, and the turbulent core model (McKee & Tan 2003) in which massive cores with non-thermal support provided by the turbulence evolve in a quasi-static way. Both of these theories predict that high-mass star formation is preceded by an epoch of the low-mass star formation, converting a larger proportion of the total mass in the competitive accretion model. Owing to low resolution, BLAST observations cannot differentiate between these two hypotheses on this basis, nor do we have masses for the *Spitzer* YSOs.

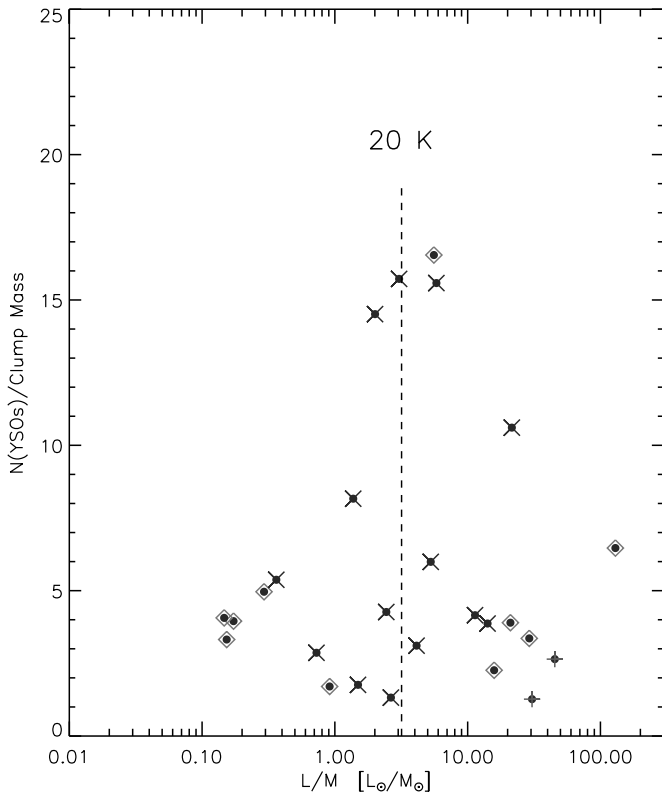


Figure 29. Number of YSOs (Classes 0, I, and II) per 100 M_{\odot} vs. L/M . The cross, diamond, and plus symbols represent surface densities Σ in the ranges 0.005–0.02, 0.02–0.08, and 0.08–0.4 g cm^{-2} , respectively. The vertical (dashed) line corresponds to 20 K, a typical value where Σ in the model of Krumholz & McKee (2008) is about 1 g cm^{-2} for the masses of BLAST sources (see Section 6.3 and Figure 24).

However, the intermediate resolution MAMBO data resolves sub-structures (cores) of size ~ 0.1 pc within our clumps. In Figure 30, we compare the total mass of the cores within each clump to the clump mass (assuming the cores are at the same temperature as BLAST observes for the clump). We find that (only) 20% of the clump mass is in cores; however, four bright sources (W75N, DR21, DR21(OH), and C160) were excluded in the fit.

6.3. Relationship to Surface Density

According to the model of Krumholz & McKee (2008), for the low L/M regime the steady-state accretion luminosity generated by the low-mass YSOs is

$$L = 390 \left(\frac{\Sigma}{1 \text{ g cm}^{-2}} \frac{M}{100 M_{\odot}} \right)^{0.67} L_{\odot}. \quad (7)$$

In order to show the relative position of BLAST sources with respect to this model prediction, we plot loci in the L – M diagram of Figure 24 for $\Sigma = 1.0, 0.1, \text{ and } 0.01 \text{ g cm}^{-2}$.

If this theory is adopted, then we can directly determine surface density from Equation (7) for any source in the L – M diagram. This is the surface density that would be required for a clump of mass M to produce a luminosity of L . However, we can also measure the surface density directly. In Figure 31, we plot surface densities of BLAST sources versus the model surface density, for sources below $L/M < 6 L_{\odot}/M_{\odot}$ where most of the luminosity arguably comes from low-mass stars. The measured surface density of the most of the sources is below the one-to-one line. This might be because we have underestimated Σ

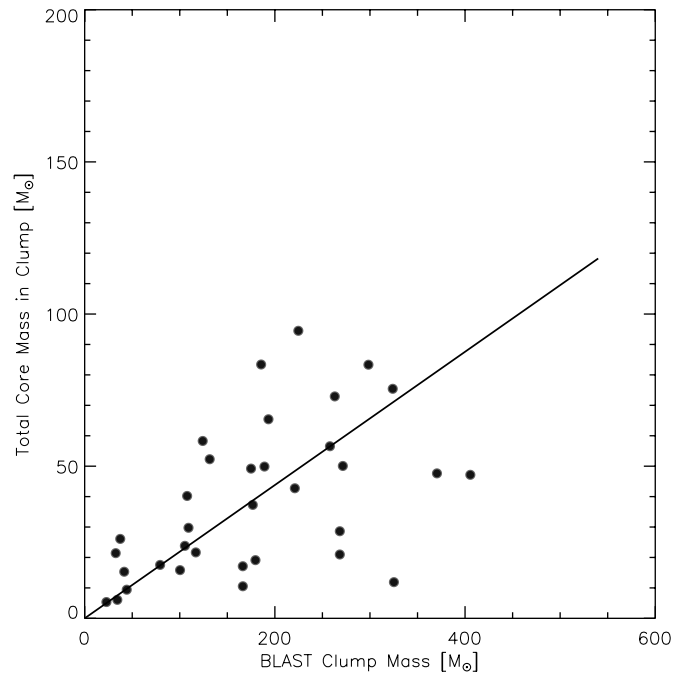


Figure 30. Sum of the masses of cores within the BLAST clumps vs. the clump mass. The linear correlation shown has a slope 0.20.

owing to poor angular resolution; qualitative support for this is the evidence of sub-structure (Section 6.2). However, there are about eight sources with surface density above the one-to-one line. These are very interesting, possibly a very early stage where the presumed steady state of low-mass YSO formation has not been achieved. We have confirmed that there is a lower number of YSOs associated with these sources, except for the source shown by a cross in Figure 31 which was difficult to measure near the edge of the image at 500 μm .

Krumholz & McKee (2008) note that because cores with higher Σ are warmer due to the power of the low-mass YSOs, there is a critical Σ such that by the time the steady-state heating is achieved fragmentation into further low-mass YSOs halts. The threshold surface density is about 1 g cm^{-2} and this is plotted in Figure 24. This characteristic surface density should be a marker of (potential) massive star-forming regions, and there is some evidence consistent with this, at least for evolved objects. In the BLAST survey, we find that the few most luminous sources containing compact H II regions have such a high surface density. The MAMBO cores containing compact H II regions and MIRQPs with strong SiO emission also have a high measured surface density (Table 3). Similarly, Garay et al. (2006) found an average surface density of 0.8 g cm^{-2} for dense cores of ultracompact H II regions. We find that the typical surface density of massive embedded star clusters observed by Le Duigou & Knödseder (2002) in the Cyg X region is about 1 g cm^{-2} (allowing for the presence of some additional gas—now dispersed—in the precursor).

An observed, high Σ associated with MYSOs might not be a unique signature to the turbulent core model, or even a prerequisite. In the simulations by Smith et al. (2009) of a competitive accretion model, “massive stars were not formed from a single massive thermally supported fragment, but instead from a smaller core which accreted additional material channeled toward it by the potential of the forming stellar cluster.” Likewise, in the simulations by Wang et al. (2010) of a model of “clump-fed massive star formation” regulated by outflow

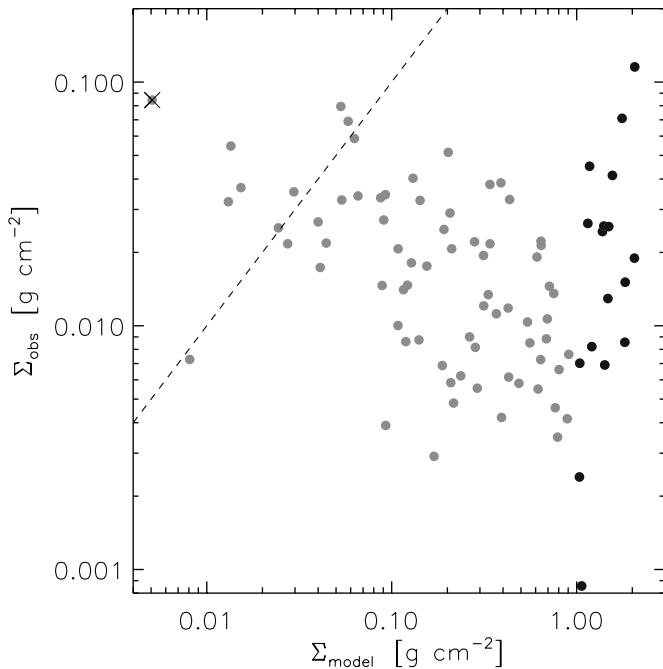


Figure 31. Observed surface density of BLAST clumps with $L/M < 6 L_{\odot}/M_{\odot}$ vs. the surface density required in the low-mass YSOs model of Krumholz & McKee (2008) to produce the observed L given the observed M . Sources above the one-to-one line (dashed) are underluminous compared to the prediction from the model, and so possibly very young. The source shown by a cross is near the map edge at $500 \mu\text{m}$. Sources with model surface density more than 1 g cm^{-2} are highlighted.

feedback (ORCF), “the most massive object is not formed out of a pre-existing dense core” but rather “is controlled by the global clump dynamics.” Recently, Csengeri et al. (2010) observed a few of the massive young dense cores (C107, C115, C119, DR21(OH), and DR21) in Cyg X to study the kinematic properties of the underlying environment. They found that non-thermal support due to turbulence at the scale of the dense core is not enough for a quasi-static evolution of the massive protostars as predicted by the turbulent core model of McKee & Tan (2003), and they favor competitive accretion.

Therefore, a key question in investigating the mode of evolution is whether there is evidence for cold high- Σ clumps or cores before high-mass protostar(s), and even the preceding low-mass YSOs, are established. Even if the evolution timescale were favorably long, this would be difficult with BLAST, as can be seen directly from Equation (3): at the spatial resolution of 0.5 pc about $4000 M_{\odot}$ is needed to produce a surface density of 1 g cm^{-2} . We have noted that we do not see such massive cold objects; if such dense cold objects do exist at lower mass, we cannot identify them by directly measuring their true Σ . Higher resolution is required for such detections; for example, MAMBO observations at the resolution of 0.1 pc in Cyg X need a mass of only $150 M_{\odot}$ to produce equivalent contrast. The predominantly low surface densities obtained by Elia et al. (2010) suggest that even the *Herschel* resolution is not sufficient for finding such dense sub-structures in most cold sources.

6.4. Vertical Evolution in the L - M Diagram?

Given the different theories, it is still unclear to us which of the low L/M BLAST clumps will give rise to mas-

sive star formation. If there is a universal IMF, then statistically a massive clump will be required to give birth to massive protostars. Therefore, the massive clumps identified by BLAST are certainly of interest in this regard. Naively, the evolution in the L - M diagram would be vertical (constant M) as the luminosity increases from accretion onto the massive protostar and then nuclear burning. Even this is complicated because the power produced by low-mass YSOs in most theories can mask the earliest low L stage of the massive protostar.

However, it does not follow that massive clumps/cores always form massive stars. In fact, the model by Krumholz & McKee (2008) explicitly predicts that this will not happen unless Σ is above a critical value of about 1 g cm^{-2} . Otherwise, their prediction is that the clump is destined to continue to produce only low-mass stars, at some presumed steady-state rate. Thus, the vertical rise in L is arrested at a ceiling for a given Σ . We have marked such a possibility in Figure 24 with a horizontal red arrow at a level which would correspond to the sub-critical Σ of the clump. The end result is a cluster or association of only low-mass stars, i.e., one with a truncated IMF. Because the precursor is of low Σ , the resulting assemblage of stars must be as well, making them more difficult to detect, and there is no high-mass star to draw attention to the region by its high luminosity and ionization.

The empirical context, a snapshot of the stages of evolution, is that there is a hierarchy of structures. BLAST identifies compact sources of size about 0.5 pc within the CO clumps of spatial extent about 10 pc (Schneider et al. 2006). Within most of the BLAST clumps, MAMBO is able to find smaller and denser sub-structures of scale 0.1 pc . Presumably, these structures have been created and evolve by accumulating mass in the dynamical environment of the larger reservoir and possibly also simultaneously transfer mass to the immediately lower scale sub-structures. At any given time, these structures will each have a characteristic Σ . At some point does this become frozen in time so that we can discuss the fate of the objects of fixed Σ ? Or tracking a clump, could Σ and M evolve, allowing evolution toward the upper right in the L - M diagram? We have indicated this latter possibility as well in Figure 24—of course, only schematically. Recent numerical simulations of the competitive accretion model (Smith et al. 2009), and the ORCF model (Wang et al. 2010) which has features of both competitive accretion and the turbulent core model, show a channeling of mass to bound potential energy minima of the parsec-scale dense clumps studied, emphasizing the importance of clump-level dynamics. In these models, when the material is cold it is more distributed and so would not be identified as a high-mass, high Σ , cold clump. By the time that mass builds up in massive cores, accreting on massive protostars, the compact source would have low-mass YSOs as well and have been warmed up. Thus, the cold precursors of dense clusters might be more extended objects than clumps, a massive reservoir yet to be channeled by gravity into a higher surface density state. Some cold IRDCs (Section 5.6.2, Figure 3), within which BLAST identifies sub-structure as sources, might fit into this scenario, but dynamical diagnostics would be needed to pursue the relevance of this possibility.

7. CONCLUSION AND FUTURE WORK

An unbiased survey conducted by BLAST has enabled us to detect both compact sources and the embedding diffuse emission as a basis for studying the earliest stages of star formation.

We have quantified contrasting dust temperatures of diffuse extended structures by correlating the fluctuating emission in *IRAS* and BLAST bands. To reveal the global morphology, we have studied the relationship between dust continuum emission and radio, mid-infrared, and ^{13}CO line emission. Comparing the total mass present in the BLAST compact sources with the parent ^{13}CO clump mass (Schneider et al. 2006), we have obtained a linear correlation with slope of 0.05, which might not only be indicative of the star formation efficiency, but also relates to the relative lifetime of the compact clump phase. With multi-wavelength photometry we have tightly constrained the dust emission SEDs of the compact sources to measure temperature, luminosity, and mass. We have diagnosed the earliest stages of star formation in Cyg X, and the evolution, in the context of the luminosity–mass diagram of the compact sources. We have studied eight DR regions that are known as massive star formation sites in Cyg X. We have identified 16 sources that have compact H II emission and found an average dust temperature of 33 K. Not all of these identified sources have sufficient luminosity to be ionizing sources, pointing to the influence of Cyg OB2 creating external ionization. The complex morphology along with the direction of cometary shapes of some compact sources provides direct evidence of interaction with the massive Cyg OB2 association. Along the periphery of the evacuated H II region created by some of the more evolved stellar clusters, there is a signature of triggered star formation. We have observed a complex of infrared quiet dark clouds where star formation has already started to take place. To BLAST, and also SCUBA and MAMBO, this appears as an impressive ridge of cold dust emission. However, in sensitive high resolution $24\ \mu\text{m}$ MIPS and $8\ \mu\text{m}$ IRAC images, there is evidence of a stellar nursery, indicating a potential site of massive star formation. In our search for the precursors of clusters, however, we have not found any cold compact clump that is massive enough to become a star cluster like the Cyg OB2 association or even the other lesser embedded clusters. In the future, the unbiased Planck Cold Core survey might find such objects in unevolved GMCs, possibly in a more extended lower surface density state than in the final cluster. Resolving multi-scale structures is a new challenge underlying investigations of the earliest stages of star formation. BLAST with its limited resolution could only resolve spatial structures of 0.5 pc at 1.7 kpc away. On the other hand, MAMBO with its $11''$ resolution was successful in separating sub-structures on a scale of 0.1 pc; further progress should be possible with *Herschel*. To determine the role of surface density and more generally which cold high-mass clumps will evolve to produce high-mass protostars, even higher resolution observations will be required, and so there appears to be a rich future in uncovering the unseen story using SCUBA2 ($8''$ resolution at $450\ \mu\text{m}$, Holland et al. 2006), CCAT ($3.5''$ at $350\ \mu\text{m}$, Sebring 2010), and ALMA¹⁸ (down to subarcsecond resolution at submillimeter wavelengths).

The BLAST collaboration acknowledges the support of NASA through grant numbers NAG5-12785, NAG5-13301, and NNGO-6G111G, the Canadian Space Agency (CSA), the UK Particle Physics & Astronomy Research Council (PPARC), and Canada's Natural Sciences and Engineering Research Council (NSERC). We would also thank the Columbia Scientific Balloon Facility (CSBF) staff for their outstanding work.

18

<http://www.almaobservatory.org/en/component/content/article/16-essentials/13-numbers>

APPENDIX

MULTI-WAVELENGTH PHOTOMETRY

Flux densities at many supplementary wavelengths are presented in Tables 1 and 6. They were obtained as follows.

MAMBO 1200 μm . The MAMBO camera mounted on the IRAM 30 m telescope imaged all regions having column density greater than ($A_V \geq 15$) at wavelength of 1.2 mm (Motte et al. 2007). With its $11''$ beam, MAMBO has the ability to resolve multiple cores (if present) within BLAST clumps. Combining our data with MAMBO helps in multi-wavelength photometry, especially when any cold source is undetected in the mid- to far-infrared spectrum. To obtain consistent photometry, we first convolved the MAMBO map to $1'$, about the resolution of the BLAST maps. This has two effects: blending together any MAMBO cores and bringing in flux from the more extended emission (halo or plateau) usually associated with these multi-scale structures. Gaussian photometry was performed on the convolved map.

SCUBA 850 and 450 μm . Using the archival data from SCUBA on the 15 m James Clerk Maxwell Telescope (JCMT), Di Francesco et al. (2008) sample many high extinction regions of the Galactic Plane, including Cyg X, with diffraction-limited beams of $14.5''$ and $7.5''$, at 850 and 450 μm , respectively. Due to the higher spatial resolution, SCUBA can also identify numerous small-scale cores. The archival images consist of discontinuous smaller maps and so could not be convolved to BLAST resolution prior to photometry. Instead, we used flux densities using the SCUBA legacy catalogs of Di Francesco et al. (2008). We obtained flux densities from the Extended Map Object Catalog (EMOC) and added up all flux densities for sources within $1'$ of the BLAST source. Because of the small SCUBA maps, some BLAST sources are not completely scanned near the map edges and the resulting flux density is low.

IRAS 100 and 60 μm . Bright dust emission is observed at 100 and 60 μm throughout Cyg X, and for most of the more luminous, hotter BLAST sources these *IRAS* bands cover the peak of the SED. The *IRAS* point-source catalog does not have any entries for about half of our Cyg X region. This arose because of severe thresholds in confusion processing due to very bright source like DR21 (C. Beichman 2007, private communication). Nevertheless, the *IRAS* images that have been made subsequently are not seriously affected. We extract flux densities at 100 and 60 μm from the IGA images (Cao et al. 1997), made using HIRES (Aumann et al. 1990), a resolution enhancing algorithm. There is some elongation of sources across the dominant scan direction. The resolution at 100 and 60 μm is about $2'$ and $1'$, respectively, substantially better resolution than in the original ISSA product. Most of the isolated BLAST sources are warm enough to have a counterpart in the IGA map. BLAST counterparts at 100 μm were measured with a circular aperture of 2.4 . Similarly, at 60 μm elliptical apertures of dimension 1.8×1.2 were placed with the major axis aligned across the scan direction. In the crowded regions, multiple Gaussian photometry (elliptical in the case of 60 μm) was carried out by fixing centroids of nearby sources.

The counterparts to BLAST sources in the 60 μm images are often affected by extended cirrus-like structure and sometimes by deconvolution artifacts. Such sources show inconsistent structure between the 100 and 60 μm images. We preferred not to use such photometric data as detections to constrain the Wien part of the SED, rather using them as upper limits through

Table 6
MSX Counterparts

BLAST ID	$\Delta\alpha^a$ ($''$)	$\Delta\delta^a$ ($''$)	S_8 (Jy)	S_{12} (Jy)	S_{14} (Jy)	S_{25} (Jy)
C1	5.9	3.0	313.8	568.0	798.5	1023.4
C6	-1.5	6.0	0.2	0.8	0.6	1.6
C7	-7.8	13.7	17.1	23.5	23.4	100.0
C14	11.6	-5.1	0.4	1.0	1.2	2.4
C15	17.2	-6.2	4.6	5.8	3.7	13.6
C19	4.4	2.3	1.8	1.7	0.9	1.3
C22	-27.6	15.4	0.7	1.3	2.0	2.5
C27	15.4	-6.3	2.1	4.7	3.0	8.7
C28	34.4	-12.6	4.8	9.1	6.6	37.7
C30	-35.0	-12.5	0.5	4.0	7.6	13.8
C38	8.7	3.6	12.5	13.4	11.1	64.3
C41	8.0	-5.8	1.0	1.0	0.7	2.0
C47	-4.4	-10.7	0.2	0.6	1.3	1.5
C49	3.9	-0.7	0.7	1.4	1.3	2.7
C51	6.9	-1.5	0.2	0.6	0.7	2.3
C52	11.6	4.7	0.4	1.0	0.4	1.5
C53	4.1	-4.8	0.8	1.6	1.0	1.4
C55	-18.3	-6.0	6.3	8.1	4.0	13.2
C57	10.2	6.4	0.5	0.8	0.4	1.8
C58	-3.7	-6.3	0.7	1.2	1.1	2.5
C59	-5.3	18.7	0.7	1.2	2.3	2.7
C61	17.2	0.7	2.7	3.5	1.8	3.7
C64	2.1	0.6	2.6	4.7	4.2	5.7
C66	2.1	5.9	9.1	15.9	20.2	26.8
C67	-2.0	-1.4	1.0	1.6	0.4	1.3
C71	0.3	10.5	1.0	1.9	1.4	2.8
C73	-17.3	-2.2	3.2	5.8	7.0	19.5
C74	28.1	-12.9	0.4	0.8	0.5	1.3
C75	1.0	3.1	0.5	0.6	0.5	1.2
C76	0.1	-7.6	7.9	9.1	8.2	7.4
C80	6.9	-5.2	4.7	5.7	3.9	18.5
C83	-1.2	-6.4	1.3	1.6	0.7	1.5
C85	2.7	0.8	10.2	17.1	23.7	90.9
C87	0.8	9.6	3.4	6.3	9.6	19.7
C88	9.2	-0.0	5.4	14.6	26.2	99.3
C92	-21.6	0.2	27.1	66.1	98.5	634.1
C101	1.6	-13.0	1.5	1.7	1.6	1.4
C104	-6.0	12.4	4.9	5.7	4.4	26.6
C115	4.9	8.8	1.5	2.7	3.0	3.7
C125	-1.2	15.0	0.6	0.9	0.7	1.2
C126	-1.0	32.9	1.4	1.7	1.5	2.0
C127	-13.5	22.0	1.9	3.4	2.3	5.8
C128	-6.5	16.7	3.1	4.0	1.8	3.9
C129	11.6	18.3	0.8	1.0	0.7	1.3
C135	8.0	-7.8	0.8	2.7	5.2	11.6
C141	2.1	-13.7	0.3	0.6	0.7	1.4
C155	3.3	15.6	8.8	29.6	68.4	543.9
C157	-31.6	26.6	9.2	16.3	21.6	72.7
C160	62.8	13.0	2.8	3.3	3.4	10.8
C163	-14.0	16.5	0.3	0.8	1.2	2.1
C165	2.6	31.5	6.2	6.1	4.3	10.4
C168	-10.4	11.2	0.5	1.3	2.4	3.7
C169	19.9	8.7	15.0	27.1	55.4	331.8
C171	-0.4	-6.4	3.2	4.1	3.3	17.0
C180	0.9	2.5	11.5	17.0	23.8	124.5
C183	3.2	11.8	2.9	6.5	10.0	13.3

Note. ^a Offsets of *MSX* sources with respect to BLAST counterparts.

a penalty function (Chapin et al. 2008). In crowded regions, the flux density measurements of fainter sources are highly uncertain and for such cases we also used the photometric data as an upper limit. These upper limits are indicated by a superscript “u” in Table 1.

MIPS 70 μm . *Spitzer* *MIPS* observations at 70 μm have better resolution and sensitivity than *IRAS* IGA 60 μm data, and so are particularly useful for detecting or placing upper limits on colder and fainter BLAST sources. The *MIPS* images were destriped, which is advantageous for probing faint sources, and corrected at the pixel level for nonlinearity (Dale et al. 2007). Measurements using a Gaussian model of fixed FWHM 40 $''$ (typical extent of actual *MIPS* sources) at the positions of 39 faint BLAST sources where we have found no apparent counterparts in the *MIPS* image give an rms flux density of 5.7 Jy. This provides a very useful upper limit for these sources, constraining the SED on the Wien side of the peak. For flux densities of somewhat brighter sources, we first convolved the 70 μm map to 1 $'$, to be comparable to BLAST, and then made measurements using multi-Gaussian photometry with a linear background model. This provided useful detections for 56 sources and upper limits for the others. For six BLAST sources, pixels at the peaks of the bright *MIPS* counterparts are blanked; however, the *IRAS* data for these are sufficient to constrain the SED. The resolution of our convolved maps is also closer to the IGA 60 μm resolution, facilitating a comparison with isolated sources with a good *IRAS* detection. We find that the *MIPS* flux densities are slightly higher than at 60 μm ($F_{60}/F_{70} = 0.78$), as expected for these SEDs. At the native resolution, without beam matching, the *MIPS* flux densities are systematically lower, as is discussed by Mottram et al. (2010).

MSX 8, 12, 14, and 21 μm . *MSX* (Price et al. 2001) observed in *A*, *C*, *D*, and *E* bands at 8.3, 12.1, 14.7, and 21.3 μm , respectively. Among the four bands, *A* is the most sensitive and is dominated by diffuse emission from PAH molecules. It has angular resolution 18 $'$.3.

MSX sources have relatively small positional uncertainties (within 4 $''$ –5 $''$). *MSX* sources were identified within a search radius of 30 $''$ about the BLAST coordinate. After visual inspection, we rejected some *MSX* “matches” that were either in a PDR and/or excited by some nearby OB stars, and so had nothing to do with the star formation history of the subject BLAST source.

We extracted flux densities from the map in its native resolution directly by fitting multiple Gaussians, assuming a constant (not tilted) background. We find that our flux densities in all the bands are systematically higher than reported in the *MSX* point-source catalog, and the deviation is more noticeable for less bright sources. This trend was also observed by Molinari et al. (2008).

Results of *MSX* photometry are given in Table 6. In our present analysis, *MSX* flux densities in no way constrain temperature and total mass. We use *MSX* flux densities in the SEDs only to calculate a small correction to the bolometric luminosity by connecting data points piecewise continuously (Chapin et al. 2008). See for example, the SED for W75N in Figure 14; note the “rising spectrum” from 4 to 21 μm , characteristic of an MYSO. We find that this correction does not change the results significantly as the Cyg X sources detected by BLAST are quite cool.

REFERENCES

- Araya, E. D., Kurtz, S., Hofner, P., & Linz, H. 2009, *ApJ*, 698, 1321
Aumann, H. H., Fowler, J. W., & Melnyk, M. 1990, *AJ*, 99, 1674
Bally, J., & Lada, C. J. 1983, *ApJ*, 265, 824
Beerer, I. M., et al. 2010, *ApJ*, 720, 679
Bergin, E. A., & Tafalla, M. 2007, *ARA&A*, 45, 339
Beuther, H., Leurini, S., Schilke, P., Wyrowski, F., Menten, K. M., & Zhang, Q. 2007a, *A&A*, 466, 1065

- Beuther, H., Zhang, Q., Bergin, E. A., Sridharan, T. K., Hunter, T. R., & Leurini, S. 2007b, *A&A*, **468**, 1045
- Bica, E., Bonatto, C., & Dutra, C. M. 2003, *A&A*, **405**, 991
- Bonnell, I. A., Bate, M. R., Clarke, C. J., & Pringle, J. E. 1997, *MNRAS*, **285**, 201
- Bonnell, I. A., Bate, M. R., Clarke, C. J., & Pringle, J. E. 2001, *MNRAS*, **323**, 785
- Bonnell, I. A., Bate, M. R., & Zinnecker, H. 1998, *MNRAS*, **298**, 93
- Bonnell, I. A., Larson, R. B., & Zinnecker, H. 2007, *Protostars and Planets V*, ed. B. Reipurth, D. Jewitt, & K. Keil (Tucson, AZ: Univ. of Arizona Press), 149
- Bontemps, S., Motte, F., Csengeri, T., & Schneider, N. 2010, *A&A*, **524**, A18
- Boulanger, F., Abergel, A., Bernard, J.-P., Burton, W. B., Desert, F.-X., Hartmann, D., Lagache, G., & Puget, J.-L. 1996, *A&A*, **312**, 256
- Campbell, B. 1984, *ApJ*, **287**, 334
- Cao, Y., Terebey, S., Prince, T. A., & Beichman, C. A. 1997, *ApJS*, **111**, 387
- Carey, S. J., et al. 2005, *BAAS*, **37**, 1252
- Chapin, E. L., et al. 2008, *ApJ*, **681**, 428
- Churchwell, E. 2002, *ARA&A*, **40**, 27
- Colley, D. 1980, *MNRAS*, **192**, 377
- Comerón, F., & Torra, J. 1999, *A&A*, **349**, 605
- Comerón, F., & Torra, J. 2001, *A&A*, **375**, 539
- Comerón, F., et al. 2002, *A&A*, **389**, 874
- Compiegne, M., et al. 2011, *A&A*, **525**, A103
- Cong, H. I. L. 1977, PhD thesis, National Aeronautics and Space Administration, Goddard Space Flight Center, Greenbelt, MD
- Csengeri, T., Bontemps, S., Schneider, N., Motte, F., & Dib, S. 2010, arXiv:1009.0598
- Cyganowski, C. J., Reid, M. J., Fish, V. L., & Ho, P. T. P. 2003, *ApJ*, **596**, 344
- Dale, D. A., et al. 2007, *ApJ*, **655**, 863
- Dame, T. M., et al. 1987, *ApJ*, **322**, 706
- Davis, C. J., Kumar, M. S. N., Sandell, G., Froebrich, D., Smith, M. D., & Currie, M. J. 2007, *MNRAS*, **374**, 29
- Desert, F., Boulanger, F., & Puget, J. L. 1990, *A&A*, **237**, 215
- Di Francesco, J., Johnstone, D., Kirk, H., MacKenzie, T., & Ledwosinska, E. 2008, *ApJS*, **175**, 277
- Downes, D., & Rinehart, R. 1966, *ApJ*, **144**, 937
- Dutra, C. M., & Bica, E. 2001, *A&A*, **376**, 434
- Egan, M. P., Shipman, R. F., Price, S. D., Carey, S. J., Clark, F. O., & Cohen, M. 1998, *ApJ*, **494**, L199
- Elia, D., et al. 2010, *A&A*, **518**, L97
- Elmegreen, B. G. 1998, in *ASP Conf. Ser. 148, Origins*, ed. C. E. Woodward, J. M. Shull, & H. A. Thronson, Jr. (San Francisco, CA: ASP), 150
- Garay, G., Brooks, K. J., Mardones, D., & Norris, R. P. 2006, *ApJ*, **651**, 914
- Harvey-Smith, L., Soria-Ruiz, R., Duarte-Cabral, A., & Cohen, R. J. 2008, *MNRAS*, **384**, 719
- Haschick, A. D., Reid, M. J., Burke, B. F., Moran, J. M., & Miller, G. 1981, *ApJ*, **244**, 76
- Holland, W., et al. 2006, *Proc. SPIE*, **6275**, 62751E
- Hora, J. L., et al. 2009, *BAAS*, **41**, 498
- Hunter, T. R., Taylor, G. B., Felli, M., & Tofani, G. 1994, *A&A*, **284**, 215
- Juvela, M., et al. 2010, *A&A*, **518**, L93
- Knödseder, J. 2000, *A&A*, **360**, 539
- Kobulnicky, H. A., Gilbert, I. J., & Kiminki, D. C. 2010, *ApJ*, **710**, 549
- Koenig, X. P., Allen, L. E., Gutermuth, R. A., Hora, J. L., Brunt, C. M., & Muzerolle, J. 2008, *ApJ*, **688**, 1142
- Kraemer, K. E., et al. 2010a, *BAAS*, **42**, 253
- Kraemer, K. E., et al. 2010b, *AJ*, **139**, 2319
- Kramer, C., Stutzki, J., Rohrig, R., & Corneliussen, U. 1998, *A&A*, **329**, 249
- Krumholz, M. R. 2006, *ApJ*, **641**, L45
- Krumholz, M. R., & McKee, C. F. 2008, *Nature*, **451**, 1082
- Kurtz, S., Cesaroni, R., Churchwell, E., Hofner, P., & Walmsley, C. M. 2000, in *Protostars and Planets IV*, ed. V. Mannings, A. P. Boss, & S. S. Russell (Tucson, AZ: Univ. of Arizona Press), 299
- Kurtz, S., Churchwell, E., & Wood, D. O. S. 1994, *ApJS*, **91**, 659
- Lada, C. J., & Lada, E. A. 2003, *ARA&A*, **41**, 57
- Le Duigou, J.-M., & Knödseder, J. 2002, *A&A*, **392**, 869
- Leung, H. O., & Thaddeus, P. 1992, *ApJS*, **81**, 267
- Li, A., & Draine, B. T. 2001, *ApJ*, **554**, 778
- Lockman, F. J. 1989, *ApJS*, **71**, 469
- Lucy, L. B. 1974, *AJ*, **79**, 745
- Mac Low, M.-M., & Klessen, R. S. 2004, *Rev. Mod. Phys.*, **76**, 125
- Marston, A. P., et al. 2004, *ApJS*, **154**, 333
- Martin, P. G., et al. 2010, *A&A*, **518**, L105
- Massey, P., & Thompson, A. B. 1991, *AJ*, **101**, 1408
- McKee, C. F., & Tan, J. C. 2003, *ApJ*, **585**, 850
- Miville-Deschênes, M.-A., Lagache, G., Boulanger, F., & Puget, J.-L. 2007, *A&A*, **469**, 595
- Molinari, S., Pezzuto, S., Cesaroni, R., Brand, J., Faustini, F., & Testi, L. 2008, *A&A*, **481**, 345
- Molinari, S., et al. 2010, *PASP*, **122**, 314
- Moore, T. J. T., Mountain, C. M., & Yamashita, T. 1991, *MNRAS*, **248**, 79
- Motte, F., Bontemps, S., Schilke, P., Schneider, N., Menten, K. M., & Brogière, D. 2007, *A&A*, **476**, 1243
- Mottram, J. C., Hoare, M. G., Lumsden, S. L., Oudmaijer, R. D., Urquhart, J. S., Meade, M. R., Moore, T. J. T., & Stead, J. J. 2010, *A&A*, **510**, A89
- Negueruela, I., Marco, A., Herrero, A., & Clark, J. S. 2008, *A&A*, **487**, 575
- Netterfield, C. B., et al. 2009, *ApJ*, **707**, 1824
- Odenwald, S., Shivanandan, K., Campbell, M., Fazio, G., Schwartz, P., & Moseley, H. 1986, *ApJ*, **306**, 122
- Odenwald, S. F., Campbell, M. F., Shivanandan, K., Schwartz, P., Fazio, G. G., & Moseley, H. 1990, *AJ*, **99**, 288
- Ossenkopf, V., & Henning, T. 1994, *A&A*, **291**, 943
- Pascale, E., et al. 2008, *ApJ*, **681**, 400
- Patanchon, G., et al. 2008, *ApJ*, **681**, 708
- Perault, M., et al. 1996, *A&A*, **315**, L165
- Persi, P., Tapia, M., & Smith, H. A. 2006, *A&A*, **445**, 971
- Piddington, J. H., & Minnett, H. C. 1952, *Aust. J. Sci. Res. A: Phys. Sci.*, **5**, 17
- Poetzel, R., Mundt, R., & Ray, T. P. 1992, *A&A*, **262**, 229
- Price, S. D., Egan, M. P., Carey, S. J., Mizuno, D. R., & Kuchar, T. A. 2001, *AJ*, **121**, 2819
- Redman, R. O., Feldman, P. A., Wyrowski, F., Côté, S., Carey, S. J., & Egan, M. P. 2003, *ApJ*, **586**, 1127
- Reipurth, B., & Schneider, N. 2008, in *Handbook of Star Forming Regions, Vol. 1, Star Formation and Young Clusters in Cygnus*, ed. B. Reipurth (San Francisco, CA: ASP), 36
- Richardson, W. H. 1972, *J. Opt. Soc. Am.*, **62**, 55
- Rivera-Ingraham, A., et al. 2010, *ApJ*, **723**, 915
- Roy, A., et al. 2010, *ApJ*, **708**, 1611
- Schaerer, D., & de Koter, A. 1997, *A&A*, **322**, 598
- Schneider, N., Bontemps, S., Simon, R., Jakob, H., Motte, F., Miller, M., Kramer, C., & Stutzki, J. 2006, *A&A*, **458**, 855
- Sebring, T. 2010, *SPIE Conf.*, **7733**, 77331X
- Sibthorpe, B., et al. 2010, *ApJ*, **719**, 1553
- Simon, R., Rathborne, J. M., Shah, R. Y., Jackson, J. M., & Chambers, E. T. 2006, *ApJ*, **653**, 1325
- Smith, R. J., Longmore, S., & Bonnell, I. 2009, *MNRAS*, **400**, 1775
- Stahler, S. W., & Palla, F. 2005, *The Formation of Stars* (New York: Wiley)
- Stutzki, J., & Guesten, R. 1990, *ApJ*, **356**, 513
- Taylor, A. R., et al. 2003, *AJ*, **125**, 3145
- Truch, M. D. P., et al. 2008, *ApJ*, **681**, 415
- Truch, M. D. P., et al. 2009, *ApJ*, **707**, 1723
- Uyaniker, B., Fürst, E., Reich, W., Aschenbach, B., & Wielebinski, R. 2001, *A&A*, **371**, 675
- Waller, W. H., & Boulanger, F. 1994, in *ASP Conf. Ser. 58, The First Symposium on the Infrared Cirrus and Diffuse Interstellar Clouds*, ed. R. M. Cutri & W. B. Latter (San Francisco, CA: ASP), 129
- Wang, P., Li, Z., Abel, T., & Nakamura, F. 2010, *ApJ*, **709**, 27
- Wendker, H. J., Higgs, L. A., & Landecker, T. L. 1991, *A&A*, **241**, 551
- Werner, M. W., et al. 2004, *ApJS*, **154**, 1
- Westerhout, G. 1958, *Bull. Astron. Inst. Netherlands*, **14**, 215
- Williams, J. P., de Geus, E. J., & Blitz, L. 1994, *ApJ*, **428**, 693
- Wu, L.-X., & Yang, J. 2005, *Chin. Astron. Astrophys.*, **29**, 370
- Zinnecker, H., & Yorke, H. W. 2007, *ARA&A*, **45**, 481